공학박사 학위논문

리튬 및 소듐 이차전지용 흑연계 전극소재에 대한 연구

Graphite Derivatives for Li and Na Rechargeable Batteries

2015년 2월

서울대학교 대학원

재료공학부

김 해 겸

Abstract

Graphite Derivatives for Li and Na Rechargeable Batteries

Kim Haegyeom

Department of Materials Science and Engineering

College of Engineering

Seoul National University

The development of a low-cost and high-performance energy storage device is considered as a key issue in moving toward a sustainable society. The electricity production from renewable energy resources such as solar, wind and geothermal energy does not always coincide with consumption time. Therefore, the energy storage devices is necessary to account for the discrepancy. Currently, various energy storage devices (*i.e.* Li rechargeable batteries, Na rechargeable batteries, and supercapacitors) are intensively studied for emerging large scale applications.

For satisfying the emerging large scale applications, it is of prime importance in developing low-cost and high energy/power energy storage devices. Graphite is earth-abundant, non-toxic, and it can be obtained by relatively low cost process. Furthermore, graphitic materials have high electric conductivity, which is beneficial to deliver high power density. Under this consideration, graphite derivatives are the most promising electrode materials for next

generation energy storage applications. This thesis proposes novel approaches for utilizing graphite derivatives as electrodes, including both anode and cathode, for Li and Na rechargeable batteries, while graphite electrode is currently used only for Li rechargeable battery anodes.

Chapter Ⅱ deals with sodium storage behaviors in natural graphite using ether-based electrolytes. This thesis demonstrates that ether-based electrolytes enable sodium intercalation into natural graphite using sodium-solvent co-intercalation behaviors. The natural graphite could provide superior cycle stability over 2000 cycles without noticeable capacity degradation and supply outstanding rate capability.

Chapter Ⅲ introduces functionalized graphene nano-platelets with porous structures for Li and Na rechargeable battery applications. The functional groups anchored with conductive graphene surface can store Li and Na ions with acceptably high voltage for cathode applications through surface Faradaic reactions. Because the functionalized graphene cathode uses surface Faradaic reactions differently from conventional inorganic electrode materials (*i.e.* $LiCoO_2$, $LiMn_2O_4$, and $LiFePO_4$) utilizing solid-state diffusion, much higher rate capability can be obtained. Furthermore, the surface Faradaic reaction does not accompany large volume change, and therefore, the functionalized graphene cathode can provide excellent cycle performance.

A new type energy storage device, all-graphene-battery, will be introduced in Chapter Ⅳ. All-graphene-battery is composed of functionalized graphene cathode and reduced graphene anode. In this device, the graphene with surface functional groups works as a cathode and that without functional groups functions as an anode. Because both electrodes use surface reactions,

high power density can be obtained while maintaining high energy density.

Keywords: Carbon; Graphene; Batteries; Energy storage; Energy conversion

Student Number: 2011-30186

Contents

Chapter 1 Introduction 1
1.1 General background 1
1.2 References 5
Chapter 2 Na storage in natural graphite.....7
2.1 Na storage behavior in natural graphite 7
2.1.1 Research background 7
2.1.1.1 References 10
2.1.2 Experiments 14
2.1.3 Results and disccusion 16
2.1.4 Conclusion 24
2.1.5 References 46
Chapter 3 Transition metal free cathodes.....48
3.1 Functionalized graphene for Li rechargeable batteries 48
3.1.1 Research background 48
3.1.1.1 References 51
3.1.2 Experiments 55
3.1.3 Results and disccusion 58
3.1.4 Conclusion 68
3.1.5 References 92
3.2 Functionalized graphene for Na rechargeable batteries 94
3.2.1 Research backgorund 94
3.2.1.1 References 96
3.2.2 Experiments 100

3.2.3 Results and disccusion 102
3.2.4 Conclusion 108
3.2.5 References 129
Chapter 4 All-graphene-battery 133
4.1 A new type all-graphene-battery 133
4.1.1 Research background 133
4.1.1.1 References 136
4.1.2 Experiments 140
4.1.3 Results and disccusion 142
4.1.4 Conclusion 149
4.1.5 References 172
Chapter 5 Summary 175
Chapter 6 Abstract in Korean 176
Curriculum Vitae 179

List of Tables

Table 4-1. BET surface area and pore volume of the functionalized graphene and the reduced graphene oxide.. 172

List of Figures

Figure 2-1. Na storage properties of natural graphite. 26
Figure 2-2 CV profiles of natural graphite in various electrolyte systems..... 27
Figure 2-3. Typical charge/discharge profiles of natural graphite in Na half cells with $NaPF_6$ in DEGDME. 28
Figure 2-4. (a) Galvanostatic charge/discharge profiles and (b) $dQ\ dV^{-1}$ of natural graphite in Na half cells with different electrolytes of $NaPF_6$ in DEGDME, TEGDME, and DME.(inset: schematic of solvent molecules) 29
Figure 2-5. Charge/discharge profiles of natural graphite in three different electrolyte systems. 30
Figure 2-6. FE-SEM images (a and c) and galvanostatic charge/discharge profiles (b and d) of natural graphite (above) and synthetic graphite (below). The natural graphite and synthetic graphite were purchased from Sigma-Aldrich. 31
Figure 2-7. Charge/discharge profiles of natural graphite using different Na salts in DEGDME. 32
Figure 2-8. Charge/discharge profiles of natural graphite operated at high temperature (60 ^oC). 33
Figure 2-9. Cycle stability of natural graphite at 100 mA g^{-1}. 34
Figure 2-10. Long-term cycle stability of natural graphite at 500 mA g^{-1}..... 35
Figure 2-11. Rate capability of natural graphite at various current rates from 0.1 A g^{-1} to 10 A g^{-1}..... 36
Figure 2-12. Electrochemical measurements to identify Na storage mechanism in $NaPF_6$ in DEGDME electrolyte. 37
Figure 2-13. CV curves of natural graphite operated at various scan rates from 0.2 mV s^{-1} to 3 mV s^{-1}..... 38
Figure 2-14. Na storage mechanism in natural graphite through *ex situ* analyses. 39
Figure 2-15. HR-TEM images of natural graphite 40
Figure 2-16. FE-SEM image of natural graphite after discharge. 41
Figure 2-17. Typical charge/discharge profiles (above) and thickness change of natural graphite electrode (below). 42
Figure 2-18. Charge/discharge profile of natural graphite/Li cells 43

Figure 2-19. Confirmation of co-intercalation using FTIR analysis. 44
Figure 2-20. (a) EIS analysis after discharge in $NaPF_6$ in EC/DEC (above) and $NaPF_6$ in DEGDME (below). (b) A proposed schematic on how Na storage is possible in natural graphite with selected electrolyte systems. 45
Figure 2-21. Electrochemical properties of full cells using $Na_{1.5}VPO_{4.8}F_{0.7}$ cathode and natural graphite anode. 46
Figure 3-1. Solvent-assisted pore formation of the functionalized graphene nano-platelets. 70
Figure 3-2. The cross-sectional images of the functionalized graphene cathode. 71
Figure 3-3. FE-SEM images of GO samples 72
Figure 3-4. Demonstration of scalability of the functionalized graphene nano-platelets 73
Figure 3-5. Pore formation and reduction mechanism. 74
Figure 3-6. FT-IR spectra of GO 75
Figure 3-7. *In-situ* MS analysis result of HCl-treated samples 76
Figure 3-8. XPS spectra of H_2O-washed, NH_3-washed GO and HCl-washed samples after heat treatment at 120°C. 77
Figure 3-9. Schematic drawing of the pore formation and reduction mechanism 78
Figure 3-10. FE-SEM images of HFG, MFG, LFG, and MFG-400 samples. .. 79
Figure 3-11. Functionality-dependant electrochemical behavior of the functionalized graphene nano-platelets. 80
Figure 3-12. O/C ratio analysis of the functionalized graphene nano-platelets and O/C ratio uniformity. 81
Figure 3-13. Charge/discharge profiles of the samples in which the profile shapes 82
Figure 3-14. *Ex-situ* XPS analyses 83
Figure 3-15. *Ex-situ* FTIR analysis identifies that the C=O functional group participates in the lithium storage. 84
Figure 3-16. Cycle stability data over a voltage range from 1.5 to 4.5 V with a current rate of 0.1 A g^{-1}. 85
Figure 3-17. Long-lasting cyclability test of the MFG sample at a high current rate of 1 Ag^{-1} up to 2,000 cycles. 86

Figure 3-18. Morphology and chemical composition stability during battery cycling. 87
Figure 3-19. Discharge profiles at various current rates 88
Figure 3-20. Electrical conductivities and BET surface areas..... 89
Figure 3-21. Electrical conductivities and BET surface areas of HFG, MFG, LFG, and MFG-400 samples. 90
Figure 3-22. Ragone plot for the functionalized graphene nano-platelet electrodes with different amounts of functional groups 91
Figure 3-23. HR-TEM images of the functionalized graphene nano-platelets. 92
Figure 3-24. Fabrication of functionalized graphite nanoplatelets with porous structures. 110
Figure 3-25. Raman analysis of functionalized graphite nanoplatelets with a graphite reference 111
Figure 3-26. Morphologies of functionalized graphite nanoplatelets..... 112
Figure 3-27. FE-SEM images of several cross-sectioned regions of functionalized graphite nanoplatelets showing that the pores are also present inside the sample. 113
Figure 3-28. N_2 adsorption/desorption isotherm plot of functionalized graphite nanoplatelets. The hysteresis between adsorption and desorption curves revealed mesopores 114
Figure 3-29. Macroscopic distribution of functional groups in the sample... 115
Figure 3-30. FE-SEM images with EDS mapping analysis. 116
Figure 3-31. Energy storage capability and reaction mechanism. 117
Figure 3-32. *Ex-situ* XPS analyses for Na storage mechanism. 118
Figure 3-33. Material characterization of reduced graphite nanoplatelets. ... 119
Figure 3-34. The electrochemical profile of graphite nanoplatelets with few functional groups in the voltage range from 1.0 V to 4.3 V at a current rate of 0.1 A g^{-1}. 120
Figure 3-35. Anion adsorption on functionalized graphite nanoplatelet cathode. 121
Figure 3-36. Schematic illustration of the energy storage mechanism of functionalized graphite nanoplatelet cathodes. 122
Figure 3-37. Cyclability of functionalized graphite

nanoplatelets upon 40 cycles. 123
Figure 3-38. Electrochemical performance of functionalized graphite nanoplatelet cathode. 124
Figure 3-39. Electrochemical impedance spectroscopy (EIS) spectra of functionalized graphite nanoplatelets 125
Figure 3-40. Chemical and morphological stability upon battery cycling. ... 126
Figure 3-41. Energy density of various cathode materials for NIB. The average operation voltage (*vs.* Na) was used to calculate the energy density for cathodes. 127
Figure 3-42. Ragone plot of functionalized graphite nanoplatelet cathodes compared to other cathode materials for NIB and Na-ion capacitors. 128
Figure 3-43. Charge/discharge profiles at various current rates from 0.1 A g^{-1} to 30 A g^{-1}. The cut-off voltages were 1.0 V and 4.3 V. 129
Figure 4-1. Structural and morphological characterization of the functionalized graphene cathode and the reduced graphene oxide anode..... 151
Figure 4-2. XPS analysis of graphite and graphite oxide.. 152
Figure 4-3. XPS analysis of functionalized graphene and reduced graphene oxide at full scan mode 153
Figure 4-4. Raman analysis of graphite, functionalized graphene, and reduced graphene oxide.. 154
Figure 4-5. Images a. and b. are FE-SEM and HR-TEM images of the functionalized graphene, respectively. 155
Figure 4-6. Images a. and b. are FE-SEM and HR-TEM images of the reduced graphene oxide, respectively. 156
Figure 4-7. The isotherm linear plot of functionalized graphene sample. 157
Figure 4-8. The isotherm linear plot of reduced graphene oxide sample. 158
Figure 4-9. Uniformity of functional groups and interconnected pores of the functionalized graphene cathode. 159
Figure 4-10. EDS line scanning of reduced graphene oxide sample..... 160
Figure 4-11. a. A TEM image of the functionalized graphene cathode. b. and c. represent the EDS mapping images of C and O atoms.. 161
Figure 4-12. FE-SEM image of the functionalized graphene cathode, merging

with O atoms acquired by EDS mapping analysis. 162
Figure 4-13. FE-SEM images of the functionalized graphene cathode..... 163
Figure 4-14. a. FE-SEM image of functionalized graphene after FIB cutting. b. EDS mapping of carbon. c. EDS mapping of oxygen. 164
Figure 4-15. Electrochemical properties of functionalized graphene cathode. 165
Figure 4-16. *Ex-situ* XPS analysis of functionalized graphene cathode at a. Li1s and b. O1s regions. 166
Figure 4-17. Electrochemical properties of reduced graphene oxide anode.. 167
Figure 4-18. Cyclic voltammetry analysis..... 168
Figure 4-19. Schematic illustration of an advanced hybrid supercapacitor and its electrochemical reaction. 169
Figure 4-20. Electrochemical performance of an advanced hybrid supercapacitor composed of a functionalized graphene cathode and a reduced graphene oxide anode in a full cell system. 170
Figure 4-21. Rate capability of all-graphene energy storage devices..... 171

Chapter 1. Introduction

1.1 General background

Now a days, energy and environmental issues are increasingly highlighted owing to the exhaustion of fossil fuels and global warming. The global energy paradigm is rapidly transforming from fossil fuels to renewable energy resources such as solar, wind, and geothermal energies. But, power production from those sustainable energy resources is not always coincident with energy demands. To resolve this discrepancy, it needs to develop large scale energy storage systems.

To date, various energy storage devices including lead-acid batteries, sodium-sulfur batteries (so-called NAS battery), lithium/sodium rechargeable batteries, and supercapacitors have been proposed and intensively studied.[1-15] The lead-acid battery that is the oldest type of rechargeable battery invented in 1859 was commercialized and widely used in 1990's.[16] However, several problems including low round-trip efficiency, low energy density, and high self-discharge rate are not suitable for emerging large scale energy storage systems such as electric vehicles and smart grids. Sodium-sulfur batteries constructed from liquid sodium and sulfur have been considered as promising candidates for large scale applications because of their high energy density, high round-trip efficiency, and long cycle stability.[4] Nevertheless, the high operating temperature (300-350 °C) and corrosive nature of the discharged products hinder their commercial applications.

As alternatives, lithium and sodium rechargeable batteries that can be operated at room-temperature have been proposed.[5, 17] Lithium and sodium rechargeable batteries typically use intercalation compounds that contain transition metals. The high redox potential of transition metals in the electrodes contribute to the high voltage of rechargeable batteries, which provides high energy density. However, the transition metals contribute to a major portion of the material costs and some transition metals are not environmentally benign. Thus, it needs to develop transition-metal-free electrode materials. This thesis focus on the development of electrode materials using graphite derivatives, which are earth abundant and non-toxic.

In chapter Ⅱ, sodium storage behaviors in natural graphite are demonstrated when ether-based electrolytes are used. While sodium intercalation into natural graphite is not available using conventional carbonate-based electrolyte systems,[10, 18-19] ether-based electrolytes enable sodium intercalation into natural graphite using sodium-solvent co-intercalation behaviors. The natural graphite could provide superior cycle stability over 2000 cycles without noticeable capacity degradation and outstanding rate capability.

Chapter Ⅲ proposes a novel strategy to use conductive graphene as cathodes for lithium and sodium rechargeable batteries. By simple and scalable synthetic route, functionalized graphene nano-platelets were prepared and used as cathodes for lithium and sodium rechargeable batteries. Graphene based electrode materials have been widely used as anode materials for lithium and sodium rechargeable batteries because of their low

lithium/sodium storage potentials.[20-23] When graphene is functionalized with oxygen-containing groups, its redox potentials storing lithium and sodium significantly increased, which are suitable for cathode applications. Differently from conventional inorganic intercalation reaction compounds, the functionalized graphene nano-platelets use surface reactions while maintaining high energy. Therefore, the functionalized graphene nano-platelets can deliver high power density without sacrificing energy density.

In chapter Ⅳ, a new type energy storage device, all-graphene-battery, will be introduced. All-graphene-battery is composed of functionalized graphene cathode and reduced graphene anode. In this device, the graphene with surface functional groups works as a cathode and that without functional groups functions as an anode. Because both electrodes use surface reactions, high power density can be obtained while maintaining high energy density.

1.2 References

1. Jung, J. Lead-Acid Battery. In *Electrochemical Technologies for Energy Storage and Conversion*, Wiley-VCH Verlag GmbH & Co. KGaA: 2011; pp 111-174.

2. Dietz, H.; Garche, J.; Wiesener, K. The effect of additives on the positive lead—acid battery electrode. *Journal of Power Sources* **1985,** *14*, 305-319.

3. Oshima, T.; Kajita, M.; Okuno, A. Development of Sodium-Sulfur Batteries. *International Journal of Applied Ceramic Technology* **2004,** *1*, 269-276.

4. Sudworth, J.; Tiley, A. *Sodium Sulphur Battery*. Springer: 1985.

5. Tarascon, J. M.; Armand, M. Issues and challenges facing rechargeable lithium batteries. *Nature* **2001,** *414*, 359-367.

6. Bruce, P. G.; Scrosati, B.; Tarascon, J.-M. Nanomaterials for Rechargeable Lithium Batteries. *Angewandte Chemie International Edition* **2008,** *47*, 2930-2946.

7. Poizot, P.; Laruelle, S.; Grugeon, S.; Dupont, L.; Tarascon, J. M. Nano-sized transition-metal oxides as negative-electrode materials for lithium-ion batteries. *Nature* **2000,** *407*, 496-499.

8. Amatucci, G. G.; Tarascon, J. M.; Klein, L. C. Cobalt dissolution in LiCoO2-based non-aqueous rechargeable batteries. *Solid State Ionics* **1996,** *83*, 167-173.

9. Ellis, B. L.; Makahnouk, W. R. M.; Makimura, Y.; Toghill, K.;

Nazar, L. F. A multifunctional 3.5[thinsp]V iron-based phosphate cathode for rechargeable batteries. *Nat Mater* **2007,** *6*, 749-753.

10. Stevens, D. A.; Dahn, J. R. High Capacity Anode Materials for Rechargeable Sodium-Ion Batteries. *Journal of The Electrochemical Society* **2000,** *147*, 1271-1273.

11. Kim, S.-W.; Seo, D.-H.; Ma, X.; Ceder, G.; Kang, K. Electrode Materials for Rechargeable Sodium-Ion Batteries: Potential Alternatives to Current Lithium-Ion Batteries. *Advanced Energy Materials* **2012,** *2*, 710-721.

12. Conway, B. E.; Birss, V.; Wojtowicz, J. The role and utilization of pseudocapacitance for energy storage by supercapacitors. *Journal of Power Sources* **1997,** *66*, 1-14.

13. Vivekchand, S. R. C.; Rout, C.; Subrahmanyam, K. S.; Govindaraj, A.; Rao, C. N. R. Graphene-based electrochemical supercapacitors. *J Chem Sci* **2008,** *120*, 9-13.

14. Hu, C.-C.; Chang, K.-H.; Lin, M.-C.; Wu, Y.-T. Design and Tailoring of the Nanotubular Arrayed Architecture of Hydrous RuO2 for Next Generation Supercapacitors. *Nano Letters* **2006,** *6*, 2690-2695.

15. Chen, S.; Zhu, J.; Wu, X.; Han, Q.; Wang, X. Graphene Oxide−MnO2 Nanocomposites for Supercapacitors. *ACS Nano* **2010,** *4*, 2822-2830.

16. Han, J.; Kim, D.; Sunwoo, M. State-of-charge estimation of lead-acid batteries using an adaptive extended Kalman filter. *Journal of Power Sources* **2009,** *188*, 606-612.

17. Pan, H.; Hu, Y.-S.; Chen, L. Room-temperature stationary sodium-

ion batteries for large-scale electric energy storage. *Energy & Environmental Science* **2013,** *6*, 2338-2360.

18. Stevens, D. A.; Dahn, J. R. The Mechanisms of Lithium and Sodium Insertion in Carbon Materials. *Journal of The Electrochemical Society* **2001,** *148*, A803-A811.

19. Doeff, M. M.; Ma, Y.; Visco, S. J.; De Jonghe, L. C. Electrochemical Insertion of Sodium into Carbon. *Journal of The Electrochemical Society* **1993,** *140*, L169-L170.

20. Wu, Z.-S.; Ren, W.; Xu, L.; Li, F.; Cheng, H.-M. Doped Graphene Sheets As Anode Materials with Superhigh Rate and Large Capacity for Lithium Ion Batteries. *ACS Nano* **2011,** *5*, 5463-5471.

21. Wang, G.; Shen, X.; Yao, J.; Park, J. Graphene nanosheets for enhanced lithium storage in lithium ion batteries. *Carbon* **2009,** *47*, 2049-2053.

22. Wang, Y.-X.; Chou, S.-L.; Liu, H.-K.; Dou, S.-X. Reduced graphene oxide with superior cycling stability and rate capability for sodium storage. *Carbon* **2013,** *57*, 202-208.

23. Lian, P.; Zhu, X.; Liang, S.; Li, Z.; Yang, W.; Wang, H. Large reversible capacity of high quality graphene sheets as an anode material for lithium-ion batteries. *Electrochimica Acta* **2010,** *55*, 3909-3914.

24. Kim, H.; Cho, M.-Y.; Kim, M.-H.; Park, K.-Y.; Gwon, H.; Lee, Y.; Roh, K. C.; Kang, K. A Novel High-Energy Hybrid Supercapacitor with an Anatase TiO2–Reduced Graphene Oxide Anode and an Activated Carbon Cathode. *Advanced Energy Materials* **2013,** *3*, 1500-1506.

Chapter 2. Na storage in natural graphite

(The content of this chapter has been published in *Adv. Funct. Mater.* DOI:10.1002/adfm.201402984. Reprinted from [H. Kim *et al.* Sodium Storage Behavior in Natural Graphite using Ether-based Electrolyte Systems. *Adv. Funct. Mater.* 25, 534-541 (2015)]. Wiley-VCH Verbg GmbH&Co. KGaA, Weinheim. Copyright 2014)

2.1 Na storage behavior in natural graphite

2.1.1 Research background

Low cost and high performance energy storage systems (ESSs) utilizing environmental-friend elements are bound to increase in demand for large-scale applications such as an electric vehicle and a stationary storage combined with renewable energy resources (*i. e.* solar, wind, and geothermal energy).[1-3] Na-ion batteries (NIBs) have been recently considered as an alternative battery system for large-scale energy storage owing to the low-cost and widespread reserves of Na salts.[4] Most research, to date, has focused on the development of cathode materials for NIBs, and therefore, considerable achievements have been obtained in the cathode materials,[5-8] but, on the contrary, much less research effort has been devoted to the anode materials.

Carbonaceous materials have been extensively investigated as the most promising anode for NIBs.[9-12] Carbon materials with low graphitization (*i. e.*

hard carbon and soft carbon) are mostly demonstrated to capable of storing Na ions through Na intercalation to large interlayer distance combined with Na filling into nanovoids.[13-15] On the other hand, graphite, which is commercially used for Li-ion batteries (LIBs) due to its advantages in terms of high capacity, low operation voltage, and excellent cycle stability, has been so far reported to be not suitable for Na storage because of its small lattice distance for Na intercalation.[16-18] Nevertheless, there have been continuous efforts to utilize graphite as an anode for NIBs because of its straightforward advantages such as low costs, earth abundance, environmental benignness, and non-toxicity. For example, Wen *et al.* and Weng *et al.* proposed chemically modified graphite as a high performance anode for NIBs.[19-20] They functionalized graphite to enlarge interlayer distance, which can facilitate Na ion diffusion and enhance Na intercalation. In spite of those intensive recent research interests, there has never been demonstrated for the Na storage in natural graphite without modification or post-treatment, which is of prime importance to a practical point of view.

It is generally known that electrolytes can affect the properties and performances of electrode materials. Solvated ion size, de-solvation energy, and solid-electrolyte interphase (SEI) formation vary depending on the electrolytes, which, in turn, affects electrochemical properties such as cycle stability and rate capability.[21-24] It was also found that the intercalation behavior of monovalent cations (*i. e.* Li, Na, and K ions) depend strongly on the nature of the electrolyte solvents.[25] The intercalation of monovalent cations is known to be efficient only when they are strongly solvated. Li ions

are intrinsically strongly solvating in nature, and thus, Li ions can easily form solvated species with most solvents, enabling efficient intercalation. On the other hand, Na ions are relatively poor in solvating capability. Therefore, solvating and intercalation behaviors of Na ions are significantly affected by the solvent species. These results motivated us to explore electrolytes to enable natural graphite to be utilized as an anode for NIBs.

In this work, we report unusual Na storage behavior in natural graphite without any modification or treatment. Natural graphite anode can deliver a reversible capacity of ~150 mAh g^{-1} when ether-based electrolytes are used. By using electrochemical and structural analyses, we demonstrate that Na storage in natural graphite occurs through Na^+-solvent co-intercalation combined with pseudocapacitive behaviors. The natural graphite anode exhibits exceptionally high cycle stability (2500 cycles) and rate capability (>75 mAh g^{-1} at 10 A g^{-1}). Furthermore, the practical validity of natural graphite in NIB full cells is examined by combination with $Na_{1.5}VPO_{4.8}F_{0.7}$ (NVPF) cathode, which delivers an energy of ~120 Wh kg^{-1} (calculated by weight of both anode and cathode active materials) with average discharge voltage of ~2.92 V.

2.1.1.1 References

1. Armand, M.; Tarascon, J. M. Building better batteries. *Nature* **2008,** *451*, 652-657.

2. Arico, A. S.; Bruce, P.; Scrosati, B.; Tarascon, J.-M.; van Schalkwijk, W. Nanostructured materials for advanced energy conversion and storage devices. *Nat. Mater.* **2005,** *4*, 366-377.

3. Kang, K.; Meng, Y. S.; Bréger, J.; Grey, C. P.; Ceder, G. Electrodes with High Power and High Capacity for Rechargeable Lithium Batteries. *Science* **2006,** *311*, 977-980.

4. Kim, S.-W.; Seo, D.-H.; Ma, X.; Ceder, G.; Kang, K. Electrode Materials for Rechargeable Sodium-Ion Batteries: Potential Alternatives to Current Lithium-Ion Batteries. *Adv. Energy Mater.* **2012,** *2*, 710-721.

5. Xu, J.; Lee, D. H.; Clément, R. J.; Yu, X.; Leskes, M.; Pell, A. J.; Pintacuda, G.; Yang, X.-Q.; Grey, C. P.; Meng, Y. S. Identifying the Critical Role of Li Substitution in P2–Nax[LiyNizMn1–y–z]O2 (0 < x, y, z < 1) Intercalation Cathode Materials for High-Energy Na-Ion Batteries. *Chem. Mater.* **2014,** *26*, 1260-1269.

6. Jian, Z.; Han, W.; Lu, X.; Yang, H.; Hu, Y.-S.; Zhou, J.; Zhou, Z.; Li, J.; Chen, W.; Chen, D., et al. Superior Electrochemical Performance and Storage Mechanism of Na3V2(PO4)3 Cathode for Room-Temperature Sodium-Ion Batteries. *Adv. Energy Mater.* **2013,** *3*, 156-160.

7. You, Y.; Wu, X.-L.; Yin, Y.-X.; Guo, Y.-G. High-quality Prussian blue crystals as superior cathode materials for room-temperature sodium-ion batteries. *Energy & Environ. Sci.* **2014,** *7*, 1643-1647.

8. Yoshida, H.; Yabuuchi, N.; Kubota, K.; Ikeuchi, I.; Garsuch, A.; Schulz-Dobrick, M.; Komaba, S. P2-type Na2/3Ni1/3Mn2/3-xTixO2 as a new positive electrode for higher energy Na-ion batteries. *Chem. Commun.* **2014,** *50*, 3677-3680.

9. Alcántara, R.; Jiménez-Mateos, J. M.; Lavela, P.; Tirado, J. L. Carbon black: a promising electrode material for sodium-ion batteries. *Electrochem. Commun.* **2001,** *3*, 639-642.

10. Komaba, S.; Murata, W.; Ishikawa, T.; Yabuuchi, N.; Ozeki, T.; Nakayama, T.; Ogata, A.; Gotoh, K.; Fujiwara, K. Electrochemical Na Insertion and Solid Electrolyte Interphase for Hard-Carbon Electrodes and Application to Na-Ion Batteries. *Adv. Funct. Mater.* **2011,** *21*, 3859-3867.

11. Zhou, X.; Guo, Y.-G. Highly Disordered Carbon as a Superior Anode Material for Room-Temperature Sodium-Ion Batteries. *ChemElectroChem* **2014,** *1*, 83-86.

12. Yan, Y.; Yin, Y.-X.; Guo, Y.-G.; Wan, L.-J. A Sandwich-Like Hierarchically Porous Carbon/Graphene Composite as a High-Performance Anode Material for Sodium-Ion Batteries. *Adv. Energy Mater.* **2014,** *4*, n/a-n/a.

13. Cao, Y.; Xiao, L.; Sushko, M. L.; Wang, W.; Schwenzer, B.; Xiao, J.; Nie, Z.; Saraf, L. V.; Yang, Z.; Liu, J. Sodium Ion Insertion in Hollow Carbon Nanowires for Battery Applications. *Nano Lett.* **2012,** *12*, 3783-3787.

14. Wenzel, S.; Hara, T.; Janek, J.; Adelhelm, P. Room-temperature sodium-ion batteries: Improving the rate capability of carbon anode materials by templating strategies. *Energy & Environ. Sci.* **2011,** *4*, 3342-

3345.

15. Stevens, D. A.; Dahn, J. R. The Mechanisms of Lithium and Sodium Insertion in Carbon Materials. *J. Electrochem. Soc.* **2001,** *148*, A803-A811.

16. Doeff, M. M.; Ma, Y.; Visco, S. J.; De Jonghe, L. C. Electrochemical Insertion of Sodium into Carbon. *J. Electrochem. Soc.* **1993,** *140*, L169-L170.

17. Nobuhara, K.; Nakayama, H.; Nose, M.; Nakanishi, S.; Iba, H. First-principles study of alkali metal-graphite intercalation compounds. *J. Power Sources* **2013,** *243*, 585-587.

18. Okamoto, Y. Density Functional Theory Calculations of Alkali Metal (Li, Na, and K) Graphite Intercalation Compounds. *J. Phys. Chem. C* **2013,** *118*, 16-19.

19. Wen, Y.; He, K.; Zhu, Y.; Han, F.; Xu, Y.; Matsuda, I.; Ishii, Y.; Cumings, J.; Wang, C. Expanded graphite as superior anode for sodium-ion batteries. *Nat. Commun.* **2014,** *5*, 4033.

20. Weng, Y.-T.; Chen, W.-C.; Ma, C.; Kuo, C.-Y.; Meng, S.; Hwang, B.-J.; Wu, N.-L. Novel Surface Modification of Graphite with Excellent Performance for Sodium Ion Battery. *Meeting Abstracts* **2014,** *MA2014-04*, 332.

21. Yamada, Y.; Furukawa, K.; Sodeyama, K.; Kikuchi, K.; Yaegashi, M.; Tateyama, Y.; Yamada, A. Unusual Stability of Acetonitrile-Based Superconcentrated Electrolytes for Fast-Charging Lithium-Ion Batteries. *J. Am. Chem. Soc.* **2014,** *136*, 5039-5046.

22. Ponrouch, A.; Dedryvere, R.; Monti, D.; Demet, A. E.; Ateba Mba, J. M.; Croguennec, L.; Masquelier, C.; Johansson, P.; Palacin, M. R. Towards high energy density sodium ion batteries through electrolyte optimization. *Energy & Environ. Sci.* **2013,** *6*, 2361-2369.

23. Cuisinier, M.; Cabelguen, P. E.; Adams, B. D.; Garsuch, A.; Balasubramanian, M.; Nazar, L. F. Unique behaviour of nonsolvents for polysulphides in lithium-sulphur batteries. *Energy & Environ. Sci.* **2014**.

24. Kim, H.; Park, Y.-U.; Park, K.-Y.; Lim, H.-D.; Hong, J.; Kang, K. Novel transition-metal-free cathode for high energy and power sodium rechargeable batteries. *Nano Energy* **2014,** *4*, 97-104.

25. Santhanam, R.; Noel, M. Effect of solvents on the intercalation/de-intercalation behaviour of monovalent ionic species from non-aqueous solvents on polypropylene-graphite composite electrode. *J. Power Sources* **1997,** *66*, 47-54.

2.1.2 Experiments

Natural graphite (Bay Carbon Inc.) was used without any modification or post-treatment. Electrolytes were carefully prepared to maintain low H_2O content (<20 ppm). Na salts including $NaPF_6$, $NaClO_4$, and $NaCF_3SO_3$ and molecular sieves were kept in a vacuum oven (180 °C) for 3 days before use. Then, the Na salts were added to electrolyte solvents including diethylene glycol dimethyl ether (DEGDME), tetraethylene glycol dimethyl ether (TEGDME), dimethoxyethane (DME), ethylene carbonate/diethyl carbonate (EC/DEC), dimethyl carbonate (DMC), and tetrahydrofuran (THF) maintaining 1 M of concentration. The solution was stirred at 80 °C for 2 days and then molecular sieves were added to remove residual H_2O in the electrolyte solution.

Graphite electrodes were prepared by mixing the active material (natural graphite, 70 wt%) with polyvinylidene fluoride binder (PVDF, 10 wt%) and conductive carbon black (20 wt%) in an *N*-methyl-2-pyrrolidone (NMP) solvent. The resulting slurry was uniformly pasted onto Al and Cu foil, dried at 120°C for 2 h, and roll-pressed. The average electrode thickness and loading density are ~45 μm and ~4.3 mg cm^{-2}, respectively. Test cells were assembled in a glove box into a two-electrode configuration with a Na metal counter electrode. A separator of grade GF/F (Whatman, USA) was sonicated in acetone and dried at 120°C before use. Electrochemical profiles were obtained over a voltage range from 2.5 to 0.001 V using a multichannel potentio-galvanostat (WonATech). The full cell were assembled using natural graphite anode and NVPF cathode with a 1:1.5 ratio for weight, in which 1

M $NaPF_6$ in DEGDME electrolyte was used. The full cell was cycled in the voltage window between 0.7 V and 4.2 V. Electrochemical impedance spectroscopy (EIS, VSP-300, Bio-Logic, France) measurements were performed from 3 MHz to 100 mHz.

The structure of the samples was analyzed with an X-ray diffactometer (XRD, D2PHASER, Bruker, USA) using Cu Kα radiation. The morphology of the samples was verified using field-emission scanning electron microscopy (FE-SEM, SUPRA 55VP, Carl Zeiss, Germany). Na storage mechanism was analyzed using X-ray photoelectron spectroscopy (XPS, PHI 5000 VeraProbe^{TM}), high-resolution transmission electron microscopy (HR-TEM, Tecnai F20, FEI), Raman spectroscopy (High resolution dispersive Raman microscope, Horiba Jobin Yvon, France), and fourier transform infrared (FTIR, Hyperion 3000, Bruker, USA).

2.1.3 Results and discussion

To observe effect of electrolyte types on the Na storage capability of natural graphite with dozens to hundreds of micron size (Figure 2-1), we examined cyclic voltammetry (CV) and galvanostatic measurements in various electrolyte systems including carbonates, ether, and furan based electrolytes (Figure 2-2 – 4-4 and Figure 2-5). Natural graphite shows negligible electrochemical activity in most electrolyte systems such as carbonate and furan based electrolytes. However, surprisingly graphite/Na cell exhibits very reversible oxidative and reductive reactions in ether based electrolytes such as diethylene glycol dimethyl ether (DEGDME) as shown in Figure 2-2, 4-3. To understand whether the reversible redox reaction in DEGDME is related to Na storage in natural graphite, CV analysis was conducted using DEGDME electrolyte without Na salts. In absence of Na ions, no electrochemical reaction occurs as shown in Figure 2-2, which implies that the reversible oxidative and reductive reactions in DEGDME electrolyte system is attributable to Na storage in natural graphite. The capacity-voltage profiles show a reversible capacity of ~150 mAh g^{-1} with average voltage of ~0.6 V (Figure 2-3). To gain reliability, we performed galvanostatic charge/discharge measurements using other natural graphite with smaller size and synthetic graphite, wherein similar charge/discharge profiles were confirmed, which indicates the electrochemical reactions in DEGDME electrolytes do not critically depend on the size or synthetic method of graphite (see Figure 2-6).

To identify the effects of Na salts and solvent species on Na storage

behaviors, galvanostatic measurements were performed to natural graphite with various ether based electrolyte systems. With various Na salts including $NaPF_6$, $NaClO_4$, and $NaCF_3SO_3$, very identical charge/discharge profiles were observed, demonstrating that anions in the electrolytes do not participate in the electrochemical reactions (see Figure 2-7). We further confirmed that Na storage in natural graphite is possible not only in DEGDME but also in other ether based electrolytes such as tetraethylene glycol dimethyl ether (TEGDME) and dimethoxyethane (DME) as shown in Figure 2-4. Independent on chain length of the electrolyte solvents, Na ions are reversibly stored in natural graphite without a significant alteration of capacity. However, unexpectedly, it was found that the plateau for Na storage is proportionally increased from 0.60 V to 0.78 V according to the chain length (Figure 2-4). This behavior indicates that the electrolyte solvents may take part in the electrochemical reactions and the solvents with longer chain length would form energetically more stable discharged products. We further conducted galvanostatic cycling at high temperature (60 °C) to identify the composition that can be thermodynamically approached. The graphite/Na cell cycled at a high temperature exhibits a very similar specific capacity to that operated at room temperature, while irreversible capacity is slightly increased due to enhanced electrolyte decomposition at high temperature. On the basis of the results, we can conclude that natural graphite can thermodynamically store Na ions up to the formation of ~NaC_{15} although further investigation is needed.

Figure 2-9 shows cycle stability of natural graphite at 100 mA g^{-1}, wherein

127 mAh g^{-1} was maintained after 300 cycles and high coulombic efficiency (>98 %) was retained while the coulombic efficiency was slightly low at the initial few cycles, which is attributable to the SEI formation. At increased current rate of 500 mA g^{-1}, natural graphite anode could deliver a reversible capacity of ~125 mAh g^{-1} (~83% of 100 mA g^{-1}) and 80% was maintained even after 2500 cycles (Figure 2-10). The excellent electrochemical properties are more highlighted in rate capability as illustrated in Figure 1i. Natural graphite could exhibit a specific capacity of ~100 mAh g^{-1} at 5000 mA g^{-1}. The most notable here is that natural graphite could show excellent electrochemical properties such as stable cycle life and high rate capability under one of the most severe conditions without any modification, functional binders, and electrolyte additives to facilitate Na storage properties.

To grasp insight into Na storage mechanism in natural graphite, electrochemical measurements were performed (Figure 2-12). Herein, we used a CV technique, which is widely used to distinguish the contributions of surface-limited capacitive and diffusion-controlled intercalation elements in the electrochemical reactions through the dependence of current on scan rates.[1-4] Figure 2a shows the typical CV curve of natural graphite/Na cells at a scan rate of 0.2 mV s^{-1}, where apparent several cathodic and anodic peaks are shown, demonstrating multiple electrochemical reactions. The capacitive and intercalation effects were analyzed by using CV data at various scan rates from 0.2 to 3 mV s^{-1} (Figure 2-13) through the following power-law relationship.[4] (Note: cathodic (intercalation) peak currents labelled to C1, C2, C3, and C4 in Figure 2-12 were used.)

$$i = av^b \quad (1)$$

where i is the current (A), v is the scan rate (mV s^{-1}), a and b are adjustable values. Figure 2-12 shows the plot of log ($|i|$) *vs.* log (v), in which the slope of the linear line is estimated to b-value. A b-value of 0.5 indicates that the reaction follows diffusion-controlled one, while a value of 1.0 indicates that the reaction is surface-limited. The b value of C3 was estimated to be 0.5, indicating diffusion-controlled reactions primarily occur, whereas the b values of C1, C2, and C4 were calculated to 0.8-0.9, indicating combined capacitive and intercalation reactions.

In order to quantitatively separate the contribution of the surface-limited capacitive and diffusion-controlled intercalation elements, the method proposed by Dunn *et al* was used.[3] Through the dependence between the peak currents and scan rates, we can estimate the contribution of capacitive and intercalation elements using the following equation:

$$i = k_1 v + k_2 v^{1/2} \quad (2)$$

where i is the current (A) at a given potential, v is the scan rate (mV s^{-1}), k_1 and k_2 are constants. Here, $k_1 v$ represents the capacitive elements and $k_2 v^{1/2}$ represents intercalation elements. If we divide both sides of the equation above with the square root of the scan rate and plot the $i/v^{1/2}$ *vs.* $v^{1/2}$, we can obtain a line with a slope of constant k_1 and the y-intercept of constant k_2, which provides a quantitative information of capacitive elements and intercalation elements (see Figure 2-12). The quantitative characterization was carried out dividing the electrochemical reactions into three different regions in Figure 2-12d. On the basis of the results, we can conclude that the

diffusion-controlled intercalation reaction primarily occurs in region II. On the other hand, the intercalation reaction in combination with capacitive reaction occurs in region I and III.

The Na storage mechanism in natural graphite was further characterized through *ex situ* analyses. *Ex situ* XPS analysis shows that the content of Na in natural graphite is noticeably changed depending on the state of discharge. In the Na1s spectra, the Na peak reversibly increased with the discharge and decreased with subsequent charge of the natural graphite electrode, demonstrating the reversible Na insertion and extraction into/from natural graphite (Figure 2-14a). It should be noted that the sample before cycling is obtained after soaking in the $NaPF_6$ in DEGDME electrolyte for 1 day. Therefore, Na1s peak from before cycling would be originated from residual Na salts in the sample. Figure 2-14b and c show the *ex situ* Raman measurements during battery cycling. After discharge process, the intensity of D band (~1340 cm^{-1}) and D' band (~1600 cm^{-1}) significantly increased, indicative of sp^3-defects formation which implies that well-ordered graphitic interlayers become disordered.[5-6] Upon charge process, the Raman spectrum reversibly returns to the original state. Na insertion reaction was further directly visualized by using high resolution transmission electron microscopy (HR-TEM) analysis as illustrated in Figure 2-15. HR-TEM image of pristine natural graphite shows well-ordered lattice fringe of ~0.33 nm. However, the graphene layers are wrinkled and disordered, and the interlayer distances are greatly increased to the range of 0.415-0.53 nm without exfoliation of graphene layers (Figure 2-15b and Figure 2-16). As a

result, the thickness of the graphite electrode was expanded as much as 34% of the pristine electrode (Figure 2-17). This behavior is attributable to the formation of sp^3-defect carbon observed in Raman spectrum after discharge. After charge, the disordered planes became well-ordered with reduced lattice fringe of ~0.34 nm without significant damages on graphite, indicating that the electrochemical Na de/intercalation reaction is reversible (Figure 2-15c).

Since Na storage in graphite is feasible with only selected electrolytes (*i. e.* ether based electrolytes) and the working voltage varies depending on the chain length of the electrolytes, we considered the possibility of the alkali ion-solvent co-intercalation into graphite, which was demonstrated in Li-system by Abe *et al.*.[7] Indeed, they reported that Li^+-solvent co-intercalation into graphite anode with DME and dimethylsulfoxide (DMSO) electrolytes differently from conventional carbonate based electrolytes. To clarify the Li^+-solvent co-intercalation behavior, we examined galvanostatic cycling of natural graphite/Li cells with an ether based electrolyte, TEGDME (Figure 2-18). The charge/discharge profiles are significantly different from those obtained with carbonate based electrolyte systems, and the specific capacity is rather similar with natural graphite/Na system using ether based electrolytes. This suggested that the reaction mechanism in Li and Na systems with ether based electrolytes is similar each other, which could be the co-intercalation of alkali ion-solvent, according to the previous work of Abe and coworkers.[7] The co-intercalation behavior of Na ions and solvents are further evident by fourier transform infrared (FTIR) analysis (Figure 2-19a). The discharge process involves appearance of FTIR vibration peaks,

which is related to solvated Na ions in the electrolytes. This phenomena suggests that Na^+-solvent are co-intercalated to natural graphite upon discharge. While it is still controversial and further study is needed, we expect that Na intercalation into the graphite interlayers is prohibited because Na-intercalated graphite is energetically unstable. On the contrary, Na^+-solvent co-intercalated graphite would be thermodynamically stable, which resulting in Na storage in natural graphite (Figure 2-19b). However, it still remains an issue why Na^+-solvent co-intercalation is possible only in selected electrolyte solvents (*i. e.* ether based electrolytes). Graphite has a hydrophobic character, and thus, the intercalated species need to a hydrophobic or non-polar environment for efficient intercalation.[8] The ether based electrolytes with a high donor number can form stable Na^+ solvated species with non-polar in character for co-intercalation into natural graphite. Also, ether based electrolyte could suppress the electrolyte decomposition, which will form a negligible SEI film on the graphite surface, enabling Na^+-solvent transport to graphite lattice. On contrary, carbonate based electrolytes would form relatively thick insulating SEI layers on the graphite surface, which blocks Na^+-solvent transport (Figure 2-20).

The practical validity of natural graphite in NIB full cells was examined by combining with NVPF cathode that we previously reported.[9] Before constructing full cells, NVPF was cycled with the $NaPF_6$ in DEGDME electrolyte, delivering ~120 mAh g^{-1} with two plateaus of ~3.6 V and ~3.9 V (*vs.* Na) as shown in Figure 2-21a. The full cell assembled with NVPF cathode and natural graphite anode (balanced with 1.5:1.0 ratio for weights)

was tested in the voltage window between 0.7 V and 4.2 V at various current rates from 0.1 A g^{-1} to 1.0 A g^{-1} (Figure 2-21b). The full cell could deliver a specific capacity of ~103 mAh g^{-1} based on anode active material, corresponding to ~41 mAh g^{-1} based on the total electroactive materials including anode and cathode with average discharge voltage of ~2.92 V. The energy density obtained in this system was ~120 Wh kg^{-1} based on the total electroactive materials. Figure 2-21c shows cycle stability of the full cells at a current rate of 0.5 A g^{-1}. It could retain more than 70 % of the initial discharge capacity after 250 cycles. While further improvement is needed for practical applications, it is worth noting that the natural graphite is feasible for NIB full cells.

2.1.4 Conclusion

This study reported unusual Na storage behavior in natural graphite through Na^+-solvent co-intercalation combined with pseudocapacitive behaviors when ether based electrolytes with a high donor number were used, which was confirmed by electrochemical and *ex situ* analyses. Natural graphite delivered a reversible capacity of ~150 mAh g^{-1} and the plateau could be tuned from 0.6 V to 0.78 V (*vs.* Na) by adjusting chain length of electrolyte solvents. Without any modification and treatment, natural graphite exhibited excellent cycle stability (~2500 cycles) and rate capability (~100 mAh g^{-1} at 5000 mA g^{-1}). The practical feasibility of natural graphite in NIB full cells was confirmed by combining with NVPF cathode, which could deliver an energy of ~120 Wh kg^{-1} with average discharge voltage of ~2.92 V. This work would stimulate extensive research interests in graphite as a promising anode for NIBs in conjunction with its straightforward advantages such as low costs, earth abundance, environmental benignness, and non-toxicity.

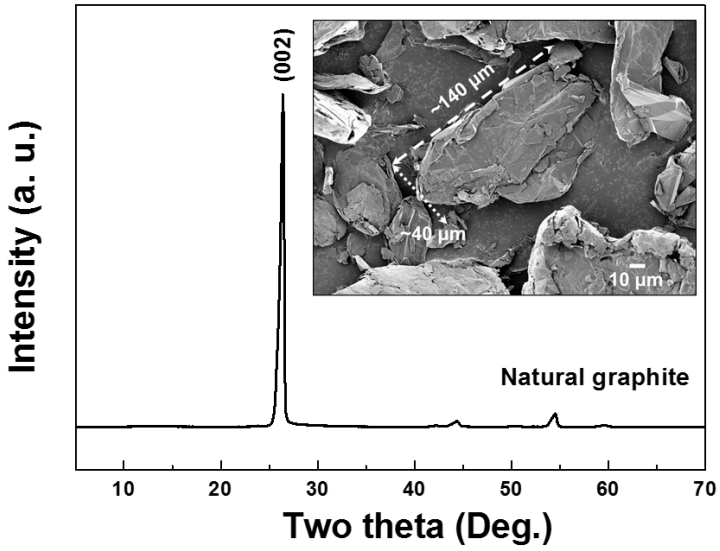

Figure 2-1. Na storage properties of natural graphite. XRD pattern of natural graphite (inset: FE-SEM image)

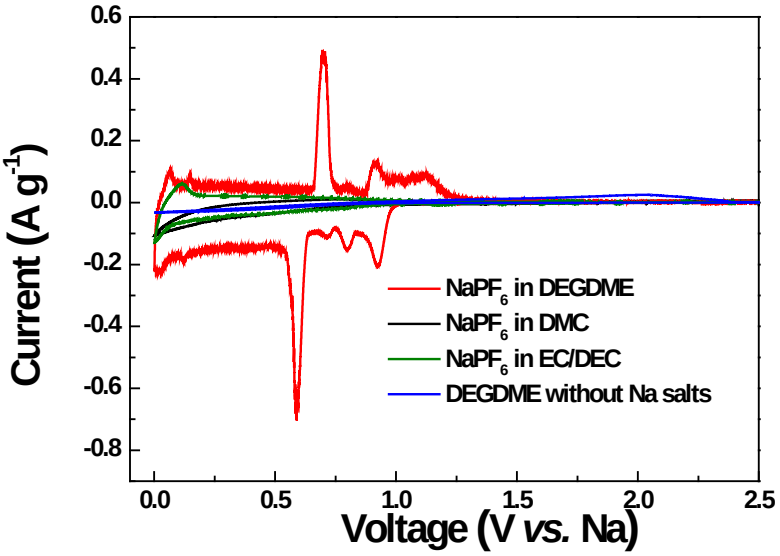

Figure 2-2 CV profiles of natural graphite in various electrolyte systems (red: $NaPF_6$ in DEGDME, black: $NaPF_6$ in DMC, green: $NaPF_6$ in EC/DEC, blue: DEGDME without Na salts)

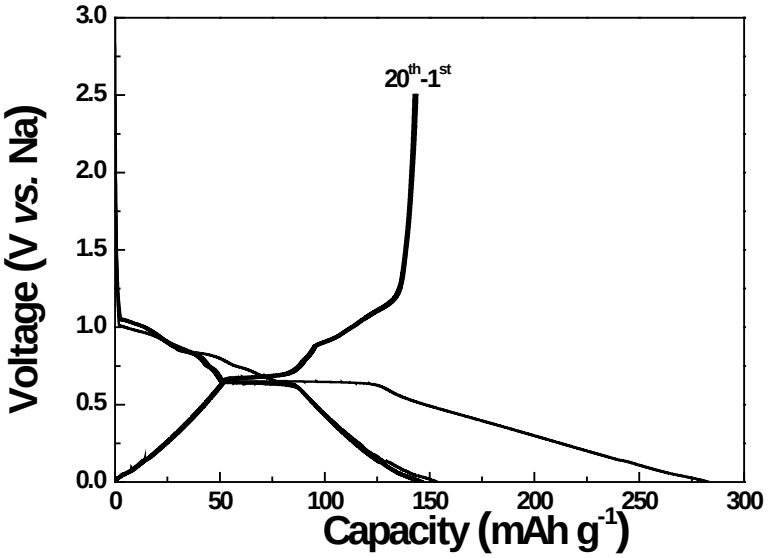

Figure 2-3. Typical charge/discharge profiles of natural graphite in Na half cells with $NaPF_6$ in DEGDME.

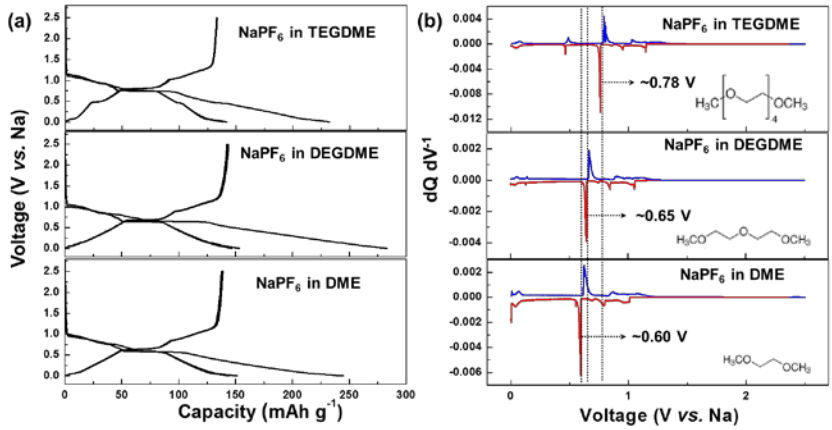

Figure 2-4. (a) Galvanostatic charge/discharge profiles and **(b)** dQ dV^{-1} of natural graphite in Na half cells with different electrolytes of $NaPF_6$ in DEGDME, TEGDME, and DME.(inset: schematic of solvent molecules)

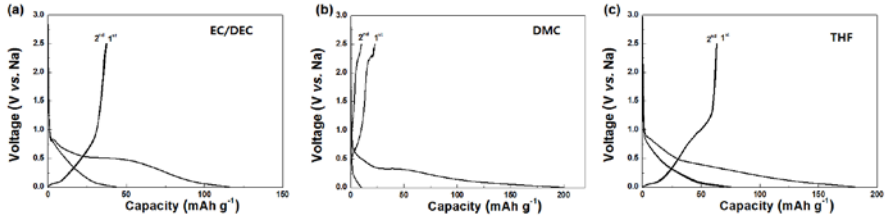

Figure 2-5. Charge/discharge profiles of natural graphite in three different electrolyte systems. $NaPF_6$ in **a.** ethylene carbonate/diethyl carbonate (EC/DEC), **b.** Dimethyl carbonate (DMC), and **c.** tetrahydrofuran (THF).

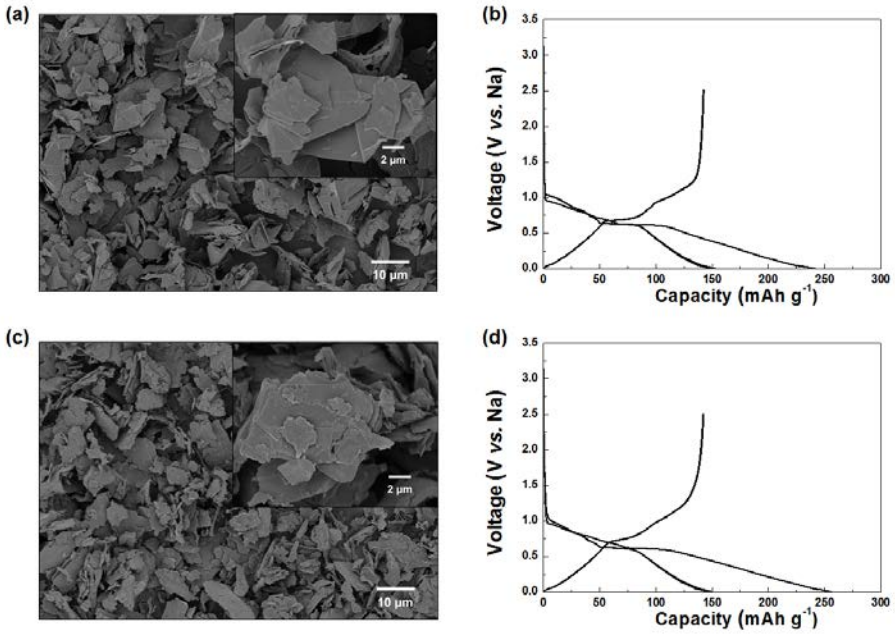

Figure 2-6. FE-SEM images (a and c) and galvanostatic charge/discharge profiles (b and d) of natural graphite (above) and synthetic graphite (below). The natural graphite and synthetic graphite were purchased from Sigma-Aldrich.

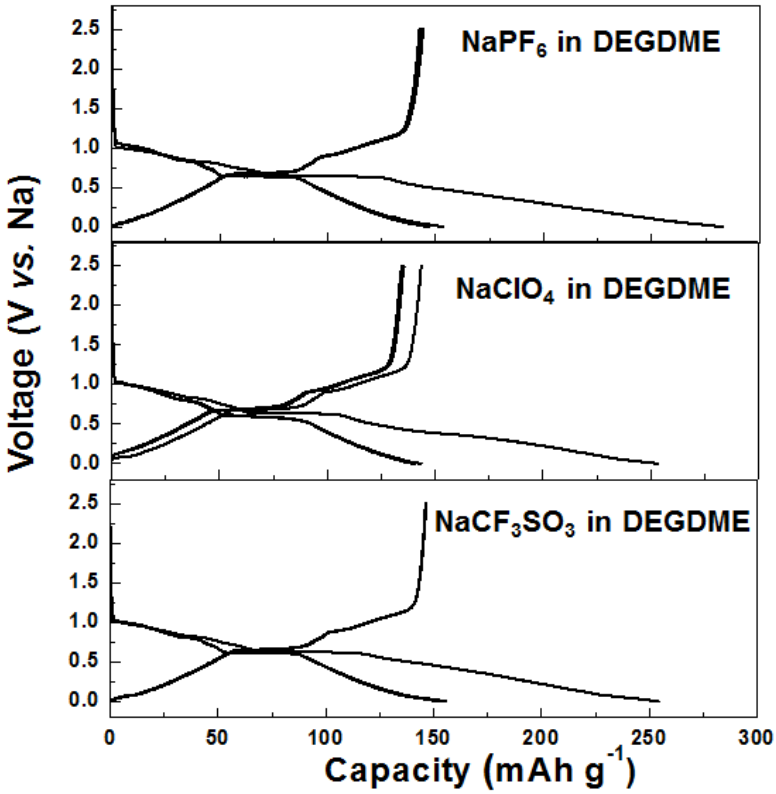

Figure 2-7. Charge/discharge profiles of natural graphite using different Na salts in DEGDME.

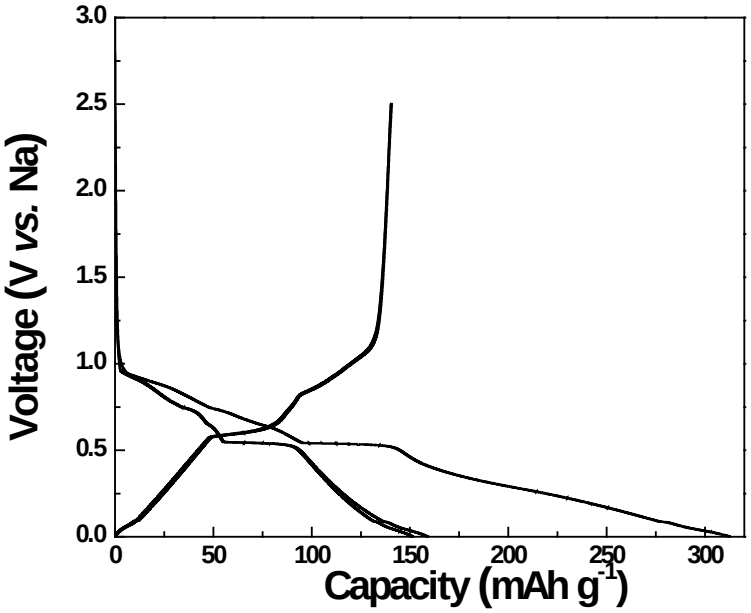

Figure 2-8. Charge/discharge profiles of natural graphite operated at high temperature (60 ºC).

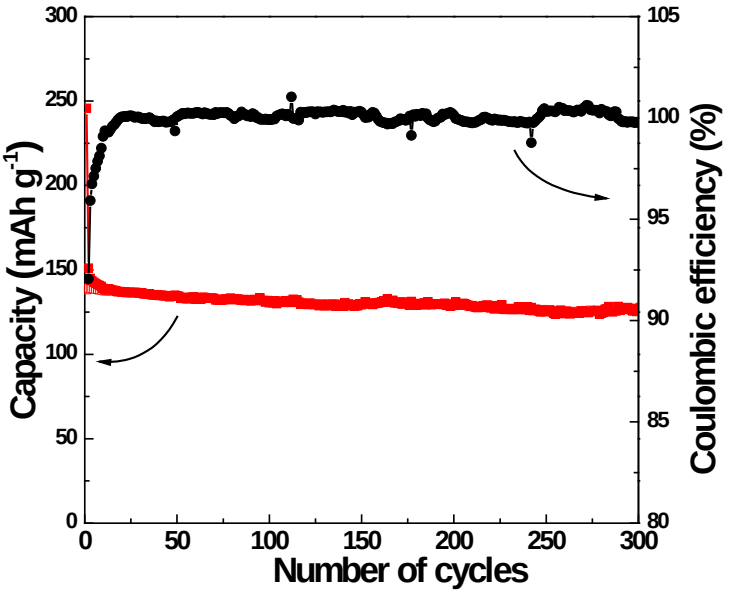

Figure 2-9. Cycle stability of natural graphite at 100 mA g^{-1}.

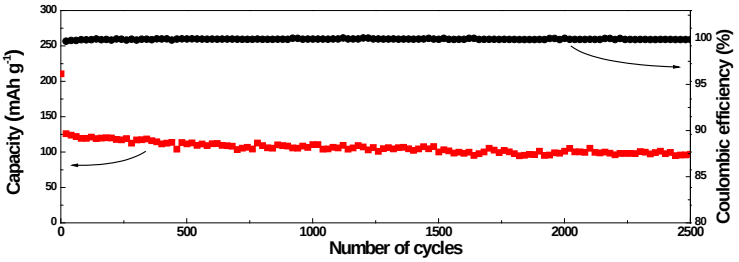

Figure 2-10. Long-term cycle stability of natural graphite at 500 mA g^{-1}.

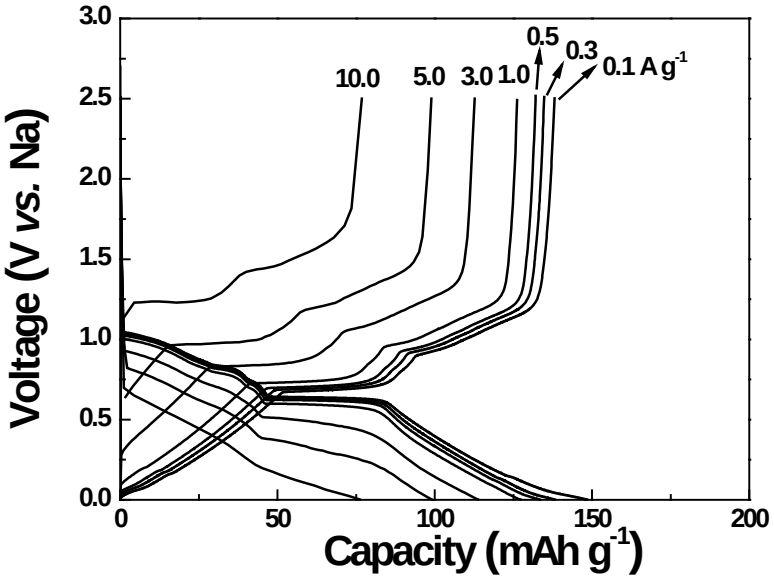

Figure 2-11. Rate capability of natural graphite at various current rates from 0.1 A g^{-1} to 10 A g^{-1}.

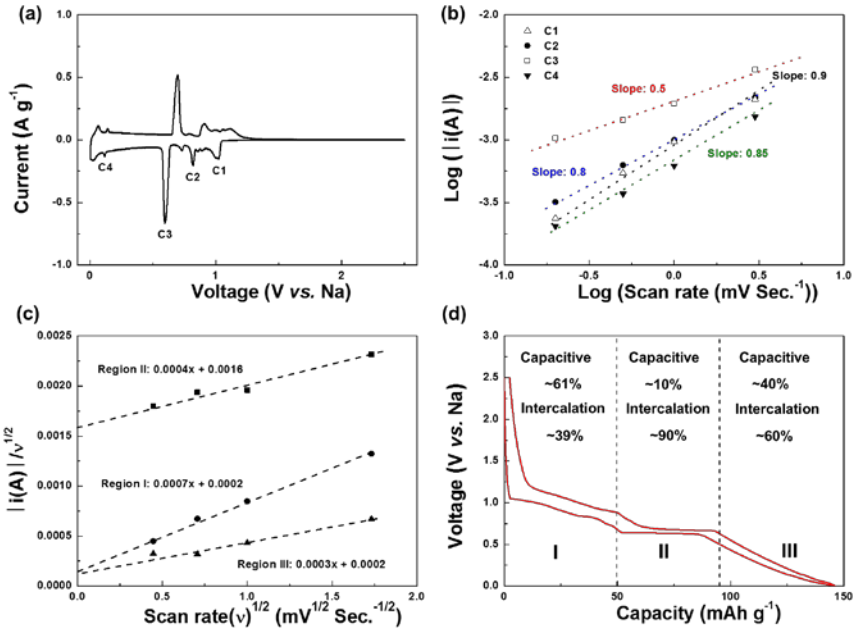

Figure 2-12. Electrochemical measurements to identify Na storage mechanism in $NaPF_6$ in DEGDME electrolyte. (a) CV profile of natural graphite. **(b)** b-value determination of the cathodic (intercalation) peak currents. **(c)** Cathodic peak current dependence on the scan rate determining capacitive and intercalation contribution for energy storage. **(d)** Typical charge/discharge profile. Quantitative contribution of capacitive and intercalation on Na storage was estimated from Figure (c).

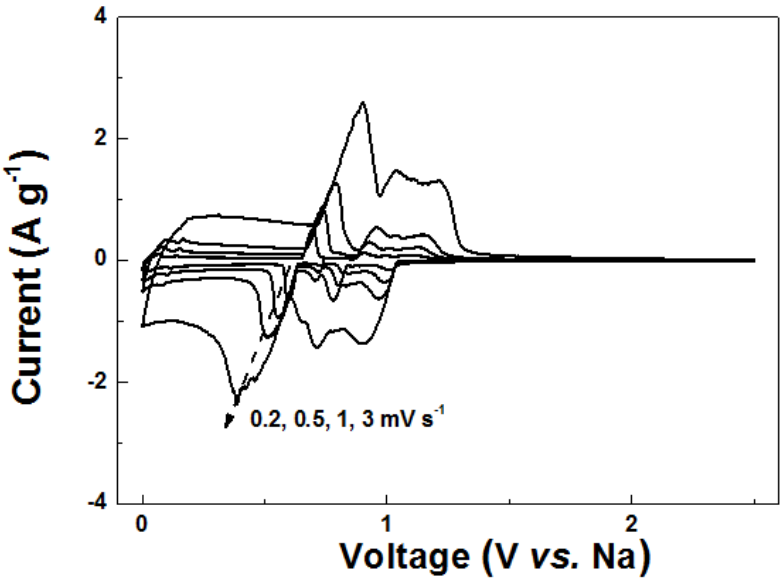

Figure 2-13. CV curves of natural graphite operated at various scan rates from 0.2 mV s^{-1} to 3 mV s^{-1}.

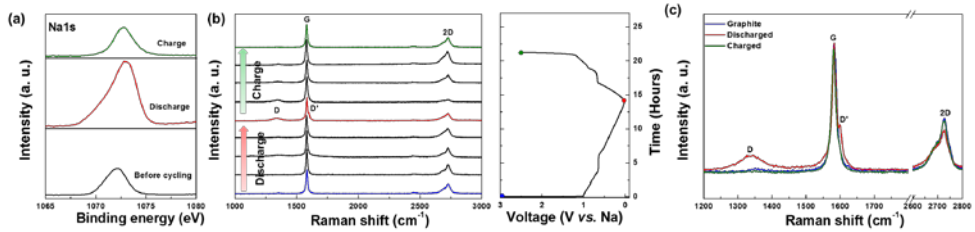

Figure 2-14. Na storage mechanism in natural graphite through *ex situ* analyses. (a) XPS analysis demonstrates Na storage in natural graphite. **(b)** Raman measurements confirms that sp^3-defect formation in natural graphite upon discharge. The sp^3-defect disappeared after subsequent charge. **(c)** Magnified Raman spectra of natural graphite with discharged and charged samples.

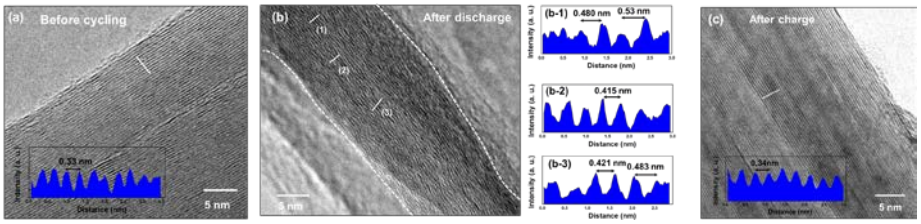

Figure 2-15. HR-TEM images of natural graphite at **(a)** before cycling, **(b)** after discharge, and **(c)** after charge with lattice distances in the samples. The HR-TEM analysis reveals that the Na storage generates disordered planes with expanded lattice distance.

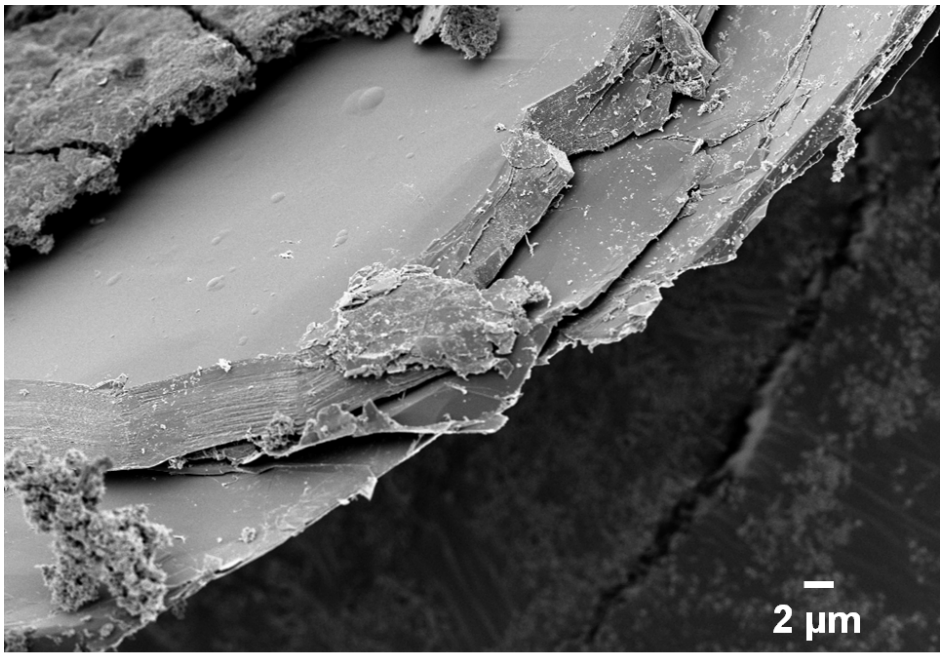

Figure 2-16. FE-SEM image of natural graphite after discharge. $NaPF_6$ in DEGDME was used as an electrolyte.

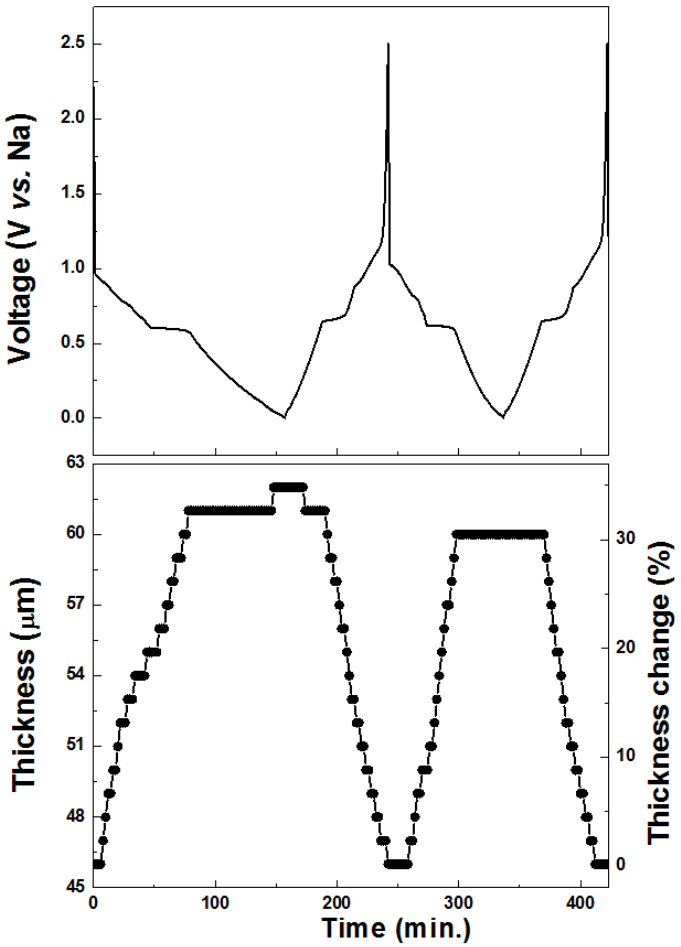

Figure 2-17. Typical charge/discharge profiles (above) and thickness change of natural graphite electrode (below).

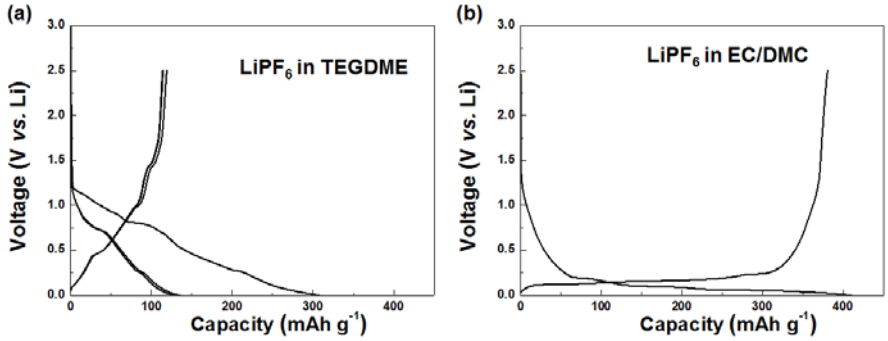

Figure 2-18. Charge/discharge profile of natural graphite/Li cells in **a.** $LiPF_6$ in TEGDME and **b.** $LiPF_6$ in EC/DMC

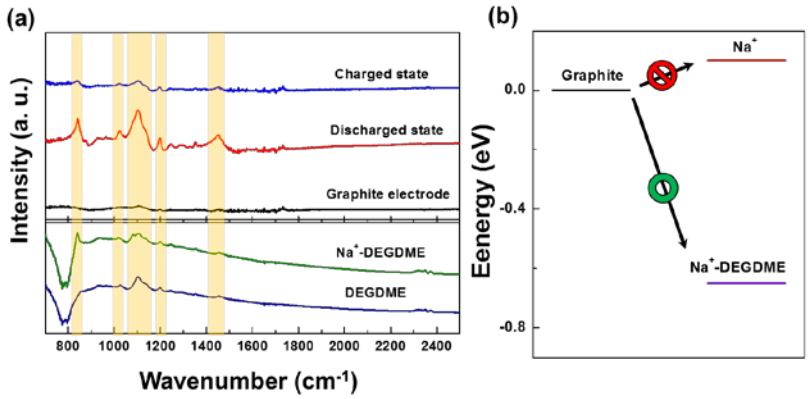

Figure 2-19. Confirmation of co-intercalation using FTIR analysis. (a) FTIR analysis demonstrates that Na storage occurs through solvated Na ion co-intercalation. **(b)** Schematic shows a proposed energetics of Na^+-intercalated graphite and N^+-solvent co-intercalated graphite.

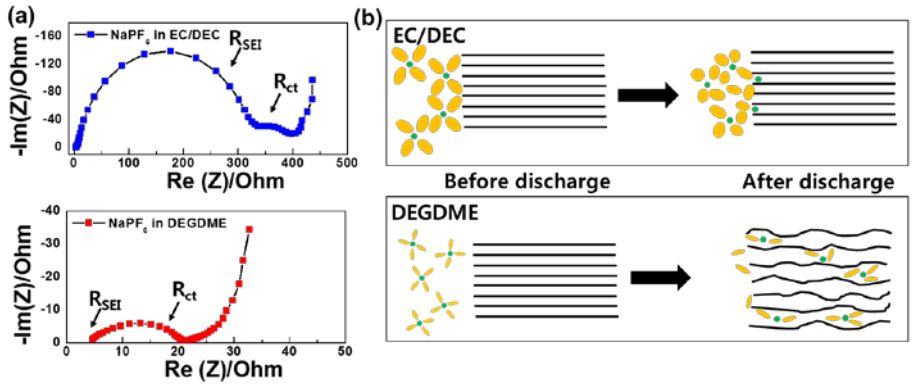

Figure 2-20. (a) EIS analysis after discharge in $NaPF_6$ in EC/DEC (above) and $NaPF_6$ in DEGDME (below). **(b)** A proposed schematic on how Na storage is possible in natural graphite with selected electrolyte systems.

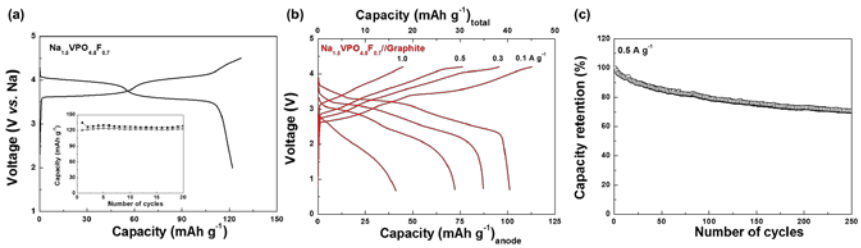

Figure 2-21. Electrochemical properties of full cells using $Na_{1.5}VPO_{4.8}F_{0.7}$ cathode and natural graphite anode. (a) Typical charge/discharge profile of $Na_{1.5}VPO_{4.8}F_{0.7}$ cathode in $NaPF_6$ in DEGDME electrolyte. **(b)** Galvanostatic charge/discharge profiles of the full cells at various current rates. **(c)** Cycle stability of the full cells at 0.5 A g^{-1}.

2.1.5 References

1. Chen, Z.; Augustyn, V.; Jia, X.; Xiao, Q.; Dunn, B.; Lu, Y. High-Performance Sodium-Ion Pseudocapacitors Based on Hierarchically Porous Nanowire Composites. *ACS Nano* **2012,** *6*, 4319-4327.

2. Wang, X.; Li, G.; Chen, Z.; Augustyn, V.; Ma, X.; Wang, G.; Dunn, B.; Lu, Y. High-Performance Supercapacitors Based on Nanocomposites of Nb2O5 Nanocrystals and Carbon Nanotubes. *Adv. Energy Mater.* **2011,** *1*, 1089-1093.

3. Wang, J.; Polleux, J.; Lim, J.; Dunn, B. Pseudocapacitive Contributions to Electrochemical Energy Storage in TiO2 (Anatase) Nanoparticles. *J. Phys. Chem. C* **2007,** *111*, 14925-14931.

4. Augustyn, V.; Come, J.; Lowe, M. A.; Kim, J. W.; Taberna, P.-L.; Tolbert, S. H.; Abruña, H. D.; Simon, P.; Dunn, B. High-rate electrochemical energy storage through Li+ intercalation pseudocapacitance. *Nat. Mater.* **2013,** *12*, 518-522.

5. Eckmann, A.; Felten, A.; Mishchenko, A.; Britnell, L.; Krupke, R.; Novoselov, K. S.; Casiraghi, C. Probing the Nature of Defects in Graphene by Raman Spectroscopy. *Nano Lett.* **2012,** *12*, 3925-3930.

6. Martins Ferreira, E. H.; Moutinho, M. V. O.; Stavale, F.; Lucchese, M. M.; Capaz, R. B.; Achete, C. A.; Jorio, A. Evolution of the Raman spectra from single-, few-, and many-layer graphene with increasing disorder. *Phys. Rev. B* **2010,** *82*, 125429.

7. Abe, T.; Fukuda, H.; Iriyama, Y.; Ogumi, Z. Solvated Li-Ion Transfer at Interface Between Graphite and Electrolyte. *J. Electrochem. Soc.*

2004, *151*, A1120-A1123.

8. Santhanam, R.; Noel, M. Effect of solvents on the intercalation/de-intercalation behaviour of monovalent ionic species from non-aqueous solvents on polypropylene-graphite composite electrode. *J. Power Sources* **1997,** *66*, 47-54.

9. Park, Y.-U.; Seo, D.-H.; Kwon, H.-S.; Kim, B.; Kim, J.; Kim, H.; Kim, I.; Yoo, H.-I.; Kang, K. A New High-Energy Cathode for a Na-Ion Battery with Ultrahigh Stability. *J. Am. Chem. Soc.* **2013,** *135*, 13870-13878.

Chapter 3. Transition metal free cathodes

3.1 Functionalized graphene for Li rechargeable batteries

3.1.1 Research background

The development of electrode materials that combine high energy and power density with low cost is an ongoing challenge for energy storage.[1] Current lithium ion batteries (LIBs) use intercalation compounds that contain transition metals for positive electrode materials. While the high redox potential of transition metals in the electrode materials contributes to the high voltage of LIBs, the presence of heavy transition metals increases the molecular weight, thus substantially decreasing the capacity. For example, about 60% of the molecular weight of $LiCoO_2$ (mw = 97.874 g mol^{-1}), the most widely used cathode, comes from Co (mw = 58.933 g mol^{-1}), and transition metals constitute a major portion of the material cost.[2–4]

Furthermore, some transition metals that are commonly used for redox reactions in cathodes are not environmentally benign.

Current electrode chemistry based on intercalation does not supply sufficient power density for LIBs applications because (i) relatively slow solid-state lithium diffusion should take place during intercalation and (ii) the electrical conductivity of such compounds is often semi-conducting or even insulating.[5–7] This has, in turn, given rise to rigorous research on the synthesis of nanostructured electrodes hybridized with conductive carbonaceous materials.[8–25] However, the synthesis of nanostructured electrodes is not trivial and often induces structural defects, which are detrimental to Li diffusion during intercalation. Also, the additional weight from the conductive agent decreases the energy density per total electrode weight.

A promising resolution to both energy and power density limitations is the use of a transition-metal-free conductive agent, itself, as an active material with a non-intercalation-based lithium storage reaction.[26–31] Here, I propose new type of electrode materials for LIBs using functionalized graphene nano-platelets with tunable power and energy density. It is noted that the previous research on graphene electrodes has been focused primarily on anode applications.[32, 33] The electrochemical reaction mechanisms and redox potentials of anode and cathode are certainly different and it is generally accepted that the discovery of cathode material is more challenging because the hosting material should store lithium with much higher potential (*e.g.* much lower lithium chemical potential). Only certain chemistries allow the

lithium to be stored in the host with potentials suitable for cathode. This work manipulating graphene from conventional anode activity to cathode region will point at an interesting new direction for electrode materials development.

The simple and cost-effective process suggested here could produce graphene nano-platelets with programmed functionalities in a porous microstructure. The fast surface Faradaic reactions of functional groups in graphene nano-platelets, combined with high electrical conductivity and porous morphology, could significantly increase energy and power density.

3.1.1.1 References

1. Yang, Z. *et al*. Electrochemical energy storage for green grid. *Chem. Rev.* **2011,** 111, 3577-3613.

2. Gaines, L., Cuenca, R. *Report#ANL/ESD-42.*, **2000**, *Argonne National Laboratory* May.

3. M. S. Whittingham. Lithium batteries and cathodes materials. *Chem. Rev.* **2004**, 104, 4271-4301.

4. Howard, W. F., Spontnitz, R. M. Theoretical evaluation of high-energy lithium metal phosphate cathode materials in Li0ion batteries. *J. Power Sources* **2007**, 165, 887-891

5. Meethong, N., Shadow, H. –Y., Speakman, S. A., Carter, W. C., Chiang, Y. –M. Strain accommodation during phase transformations in olivine-based cathodes as a materials selection criterion for high-power rechargeable batteries. *Adv. Funct. Mater.* **2007**, 17, 1115-1123.

6. Ellis, B. L., Makahnouk, W. R. M., Makimura, Y., Toghill, K., Nazar, L. F. A multifunctional 3.5 V iron-based phosphate cathode for rechargeable batteries. *Nat. Mater.* **2007**, 6, 749-753.

7. Bruce, P. G., Armstrong, A. R., Gitzendanner, R. L. New intercalation compounds for lithium batteries: layered $LiMnO_2$. *J. Mater. Chem.* **1999,** 9, 193-198.

8. Kang, B., Ceder, G. Battery materials for ultrafast charging and discharging. *Nature* **2009**, 458, 190-193.

9. Arico, A. S., Bruce, P., Scrosati, B., Tarascon, J. –M., Schalkwijk, W. V. Nanostructured materials for advanced energy conversion and storage

devices. *Nat. Mater.* **2005**, 4, 366-377.

10. Armand, M., Tarascon, J. –M. Building better batteries. *Nature* **2008**, 451, 652-657.

11. Chan, C. K. *et al.* High-performance lithium battery anodes using silicon nanowires. *Nat. Nanotech.* **2008**, 3, 31-35.

12. Kim, M. G., Cho, J. Reversible and high-capacity nanostructured electrode materials for Li-ion batteries. *Adv. Funct. Mater.* **2009**, 19, 1497-1514.

13. Cheng, F., Tao, Z., Liang, J., Chen, J. Template-directed materials for rechargeable lithium-ion batteries. *Chem. Mater.* **2008**, 20, 667-681.

14. Kim, S. –W *et al.* Fabrication and electrochemical characterization of TiO_2 three-dimensional nanonetwork based on peptide assembly. *ACS Nano* **2009**, 3, 1085-1090.

15. Lee, Y. J *et al.* Fabricating genetically engineered high-power lithium-ion batteries using multiple virus genes. *Science* **2009**, 324, 1051-1055.

16. Kim, H. *et al.* Nano-graphite platelet loaded with $LiFePO_4$ nanoparticles used as the cathode in a high performance Li-ion battery. *Carbon* **2012**, 50, 1966-1971.

17. Wang, H. *et al.* $LiMn_{1-x}Fe_xPO_4$ nanorods grown on graphene sheets for ultrahigh-rate-performance lithium ion batteries. *Angew. Chem.* **2011**, 123, 7502-7506.

18. Zhou, Y., Wang, J., Hu, Y., O'Hayre, R., Shao, Z. A porous $LiFePO_4$ and carbon nanotube composite. *Chem. Commun.* **2010**, 46, 7151-7153.

19. Kim, S. –W., Seo, D. –H., Gwon, H., Kim, J., Kang, K. A porous

$LiFePO_4$ and carbon nanotube composite. *Adv. Mater.* **2010**, 22, 5260-5264.

20. Sathiya, M., Prakash, A. S., Ramesha, K., Tarascon, J. –M., Shukla, A. K. V_2O_5-anchored carbon nanotubes for enhanced electrochemical energy storage. *J. Am. Chem. Soc.* **2011**, 133, 16291-16299.

21. Ding, K. *et al.* Preparation of nano-structured $LiFePO_4$/graphene composites by co-precipitation method. *Electrochem. Commun.* **2010**, 12, 10-13.

22. Bak, S. –M. *et al.* Spinel $LiMn_2O_4$/reduced graphene oxide hybrid for high rate lithium ion batteries. *J. Mater. Chem.* **2011**, 21, 17309-17315.

23. Zhou, X., Wang, F., Zhu, Y., Liu, Z. Graphene modified $LiFePO_4$ cathode materials for high power lithium ion batteries. *J. Mater. Chem.* **2011**, 21, 3353-3358.

24. Sun, Y., Wu, Q., Shi, G. Graphene based new energy materials. *Energy Enviorn. Sci.* **2011**, 4, 1113-1132.

25. Gwon, H. *et al.* Flexible energy storage devices based on graphene paper. *Energy Environ. Sci.* **2011**, 4, 1277-1283.

26. Simon, P., Gogotsi, Y. Materials for electrochemical capacitors. *Nat. Mater.* **2008**, **7**, 845-854.

27. Oda, H., Yamashita, A., Minoura, S., Okamoto, M., Morimoto, T. Modification of the oxygen-containing functional group on activated carbon fiber in electrodes of an electric double-layer capacitor. *J. Power Sources* **2006**, 158, 1510-1516.

28. Fan, X., Lu, Y., Xu, H., Kong, X., Wang, J. Reversible redox reaction on the oxygen-containing functional groups of an electrochemically

modified graphite electrode for the pseudo-capacitance. *J. Mater. Chem*. **2011**, 21, 18753-18760.

29. Lee, S. W. *et al.* High-power lithium batteries from functionalized carbon-nanotube electrodes. *Nat. Nanotech.* **2010**, 5, 531-537.

30. Lee, S. W., Gallant, B. M., Byon, H. R., Hammond, P. T., Shao-Horn, Y. Nanostructured carbon-based electrodes: bridging the gap between thin-film lithium-ion batteries and electrochemical capacitors. *Energy Environ. Sci.* **2011**, 4, 1972-1985.

31 . Lee, S. W. *et al.* Self-standing positive electrodes of oxidized few-walled carbon nanotubes for light-weight and high-power lithium batteries. *Energy Environ. Sci.***2012**, 5, 5437-5444.

32. Yoo, E. *et al.* Large reversible Li storage of graphene nanosheet families for use in rechargeable lithium ion batteries. *Nano Lett.* **2008**, 8, 2277-2282.

33. Reddy, A. L. M. *et al.* Synthesis of nitrogen-doped graphene films for lithium battery application. *ACS Nano* **2010**, 4, 6337-6342.

3.1.2 Experiments

$NaNO_3$ (1 g) and H_2SO_4 (45 mL) were added to graphite (1 g) and stirred for 30 min in an ice bath. Varying amounts (4–6 g) of an oxidizing agent, $KMnO_4$, were added to the resulting solution to control the degree of oxidation of the functionalized graphene nano-platelets, followed by stirring at 50°C for 2 h. Deionized (DI) water (100 mL) and H_2O_2 (6 mL, 35%) were slowly added to the solution and filtered with HCl (150 mL, 10%). Additional filtering with concentrated HCl (100 mL, 37%) was performed to retrieve the GO powder. Then, the samples were annealed at 120°C for 6 h. At this point, the color of the GO changed from dark brown to black, and the volume expanded significantly. It should be noted that functionalized graphene nano-platelets were not obtained below 120°C and without concentrated HCl treatment. As a control, treatment was also carried out with NH_3 and H_2O instead of HCl. The degree of oxidation in the functionalized graphene nano-platelets was controlled by simply changing the amount of oxidizing agent from 4 g to 6 g and by additional heat treatment. The samples were labeled HFG, MFG, LFG, and MFG-400, representing samples with high, medium, and low contents of functional groups, while the MFG-400 sample underwent additional heat treatment at 400°C. All the samples were annealed at 120°C after HCl treatment to generate a porous morphology.

The morphologies of graphite, GO, and functionalized graphene nano-platelets were investigated using field-emission scanning electron microscopy (FE-SEM, SUPRA 55VP) and high-resolution transmission

electron microscopy (HR-TEM, JEM-3000F). The structures were analyzed with an X-ray diffractometer (XRD, D8-Advance) using Cu Kα radiation over a scan range of 5–45° and Fourier transform infrared (FT-IR, Hyperion 3000) spectroscopy. X-ray photoelectron spectroscopy (XPS, AXIS-HSi) and an element analyzer (EA, EA11110-FISONS and FlashEA 1112) were used to determine the degree of oxidation of GO and the amount of functional groups in functionalized graphene nano-platelets. *Ex-situ* and *in-situ* mass spectrometry (MS, HPR-20, Hiden Analytical) were used to understand the effect of HCl on pore formation and the reduction of GO. The electrical conductivities of the functionalized graphene nano-platelets with different degrees of oxidation were measured using a four-point probe method for pelletized powder.

Electrodes were prepared by mixing the active material (functionalized graphene nano-platelets with different degrees of oxidation, 72 wt%) with polyvinylidene fluoride binder (18 wt%) and super-P (10 wt%) in an *N*-methyl-2-pyrrolidone solvent. The resulting slurry was uniformly pasted onto Al foil, dried at 120°C for 2 h, and roll-pressed. Test cells were assembled into a two-electrode configuration with a Li metal counter electrode, a separator (Celgard 2400), and an electrolyte of 1 M lithium hexafluorophosphate in a 1:1 mixture of ethylene carbonate and dimethyl carbonate (Techno Semichem) in a glove box. The loading density of the electrodes was 1.4-1.6 mg cm^{-2}. Electrochemical profiles were obtained over a voltage range from 4.5 to 1.5 V at varying current rates from 0.1 to 10.0 A g^{-1} using a multichannel potentio-galvanostat (WonATech). Cyclic

voltammetry (CV) measurements were performed using the same cell configuration with potentiao-galvanostat tests in the voltage range from 4.5 to 1.5 V at a scan rate of 0.1 mV sec^{-1}. The capacitance values were calculated from the CV curves by dividing the current by the voltage scan rate.

3.1.3 Results and discussion

Functionalized graphene nano-platelets were synthesized by controlled oxidation of pristine graphite and subsequent one-step low-temperature (~120°C) annealing. To obtain samples with different amounts of functional groups, graphite was oxidized while adjusting the amount of oxidizing agent. The primary focus was to partly reduce the graphite oxide (GO) and obtain a porous microstructure using a simple process. An optimal porous microstructure was expected to facilitate the efficient transport of lithium ions from the electrolyte through the micropores during fast charge and discharge. In one-step partial reduction process, I found that the solvent molecules, which were trapped in the interlayer galleries of hydrophilic GO during the washing step, played an important role in the generation of a porous structure upon annealing at 120°C. Various solvents were considered to optimize the porous morphology of the functionalized graphene nano-platelets from HBr to NH_3 with different vapor pressure, as shown in Figure 3-1a[1] (order of increasing vapor pressure: NH_3 > HCl > DI, H_2SO_4, CH_3COOH, HNO_3, HBr). Figure 3-1 shows that pristine graphite (Figure 3-1b) was oxidized to GO (Figure 3-1c) with interlayer expansion. During annealing at 120°C, the GO (washed in deionized (DI) water), showed mild exfoliation with visible pores along the graphene nano-platelets (Figure 3-1d). Previous reports have described similar behavior; pore formation was attributed to the sudden evaporation of water molecules trapped between the GO layers and to gas generation by thermal decomposition of labile oxygen functionalities.[2–4] Inspired by this, I decided to use solutions with higher

vapor pressures than water to enhance the effect. GO washed with an additional HCl solution (37 wt%) was annealed (Figure. 2-1e), resulting in uniform pores with sizes ranging from a few tens to a few hundred nanometers; the 10-nm-thick graphene nano-platelets covered a large area, with simultaneous partial reduction. The pore formation by the gas evolution implies that the pores are interconnected from the inside to the surface of the material. It is believed this pore formation mechanism is advantageous in that facile accessibility of the electrolyte is also possible.[5, 6] The gas evolution path which interconnects the inside and the surface of the material is expected to provide the efficient transport route for lithium ions in the electrolyte through the micropores during fast charge and discharge. From the laser scanning confocal microscopic analysis in Figure 3-2, we could have a glance at the micropores that are connected throughout the graphene cathode. Evidence of the partial reduction of GO is provided in the following paragraph. It is believed that the HCl solution trapped in the interlayer galleries of GO exhibited stronger exfoliation than HCl-free water when heated to 120°C because the vapor pressure of the HCl solution was higher than that of water. The bottom inset in Figure 3-1e shows a photograph of the resultant sample, indicating a large expansion of the powder volume compared to the pristine graphite (inset in Figure 3-1b). In order to confirm the pore generation was mainly affected by the vapor pressure, it was examined whether acidic media catalyze GO's thermal decomposition or not. However, other acidic media such as CH_3COOH and H_2SO_4 did not show any notable catalytic effects on generating pores (Figure

3-3). The use of a solution with even higher vapor pressure, NH_3 solution (30 wt%), however, did not exfoliate the GO (Figure 3-1f). This was probably because the NH_3 molecules could be easily evaporated from the sample before reaching the boiling temperature of the NH_3 solution. Finally, the scalability of the process was examined by preparing a large quantity of functionalized graphene nano-platelet samples with 30 gram scales as shown in Figure 3-4. By proportionally increasing the amount of precursor materials, the fabrication was easily scalable with a high yield about 95 %. X-ray photoelectron spectroscopy (XPS) and X-ray diffraction (XRD) analysis of the functionalized graphene nano-platelets revealed that the GO was reduced by low-temperature annealing. The XRD pattern in Figure 3-5a (above) shows that the main GO peak shifted from 10° to 24° and broadened because of the reduction of GO and the loss of long-range ordering of graphene planes.[7, 8] The bottom of Figure 3-5a compares the sample before and after annealing. The presence of two distinct peaks (286.6 and 287.6 eV) in the C 1*s* spectrum was attributed to carbon atoms in C–O moieties on the basal planes of nano-platelets and C=O moieties at the edges of nano-platelets.[9–11] Both C–O and C=O bonds in GO were significantly reduced after annealing. Fourier transform infrared (FT-IR) spectroscopy (Figure 3-6) further identified the partial reduction of GO. Simultaneous reduction and exfoliation during low-temperature annealing was monitored with *ex-situ* and *in-situ* mass spectrometry (MS), as shown in Figure 3-5b and Figure 3-7. Gas evolution of CO, H_2O, H_2, CO_2, and H_2O_2 resulted from reactions between functional groups and carbon atoms in GO.[12, 13] Gas evolution

occurred in a relatively short time, as shown in the *in-situ* MS results in Figure 3-7, which may explain the exfoliation at this temperature. The detection of gas species with molecular weights greater than 60 was attributed to the reaction of HCl with functional groups. The formation of Cl-containing molecules, such as CH_2ClOH, ClOOH, $CCOClCH_3$, and CH_3ClO_2, indicates additional reduction effects of HCl. The reduction effects of HCl were further identified by XPS analysis (Figure 3-8). HCl-washed samples contained significantly fewer functional groups than water-washed and NH_3-washed samples, suggesting that the introduction of HCl treatment enhanced the reduction of GO at 120°C more effectively than water or even NH_3 which is known to reduce GO.

The schematic illustration in Figure 3-9 shows the proposed mechanism of pore formation and reduction when GO is heated to 120°C after HCl treatment. During HCl treatment, HCl and H_2O molecules are intercalated into the interlayer galleries of hydrophilic GO. As a result of dramatically increased vapor pressure in the presence of HCl upon heating, simultaneous exfoliation and pore formation occur. During gas evaporation, the paths of escaping gases create interconnected micropores within the sample. It is worthwhile to note that the connectivity of pores is important in facile lithium transport within the electrode during battery operation.

Samples containing different amounts of functional groups were prepared by adjusting the amount of oxidizing agent in preparing GO but using the same one-step low-temperature reduction. Four samples with different target amounts of functional groups are denoted as HFG (high-

content functional group), MFG (medium-content functional group), LFG (low-content functional group), and MFG-400, which denotes the MFG sample with an additional thermal reduction at 400°C. The label of HFG, MFG, and LFG were based on the content of functional groups, especially, C=O group. It should be noted that the sample in the previous section was MFG, and the porous morphology of all the samples were identical regardless of the amount of functional groups (Figure 3-10). XPS analysis revealed that the amount of residual functional groups could be systematically controlled by modifying the oxidation processes proposed in this work (Figure 3-11a). The peaks from C-O and C=O bonding in the C1*s* XPS spectra correspond well with the targeted degree of functionalization of the samples. HFG contained the highest content of C–O and C=O, while MFG-400 contained the lowest content of C–O and C=O bonds.

The atomic composition of each sample was further analyzed with an element analyzer (EA) and tabulated in Figure 3-12 along with the values obtained from XPS analysis. The O/C ratio is about 1.12 for GO, and was reduced to 0.45 for HFG and 0.33 for MFG-400. The different O/C ratios obtained by XPS and EA analysis may be due to the experimental conditions of the analysis, *i.e.*, vacuum (XPS) and ambient air (EA) atmospheres, but the overall trend of the O/C ratio was consistent. Because the reduction occurred rapidly, the uniformity of the O/C ratio within a sample was also carefully investigated. I randomly chose 10 points in the LFG sample and analyzed the O/C ratio. The O/C ratios at the 10 points were similar, as shown in F (right), which indicated that the O/C ratio was uniform

throughout the sample, despite the rapid reduction process.

Cyclic voltammetry (CV) data of the functionalized graphene nano-platelets demonstrated that surface Faradaic reactions were responsible for the electrochemical reactivity (Figure 3-11b). CV measurements of the samples were conducted in the voltage range of 1.5 to 4.5 V with 0.1 mV s^{-1} scan rate. Gravimetric capacitance was increased from 133.2 F g^{-1} (LFG sample) to 291.6 F g^{-1} (HFG sample), which coincided with the degree of oxidation of each sample. Increased capacitance was mainly observed over a voltage range from 3.0 to 1.5 V, as illustrated in the shaded region of Figure 3-11b. Recently, it was reported that carbonyl (C=O) groups can be reversibly reduced and oxidized with Li ions over a voltage range from 3.5 to 1.5 V in aromatic carbonyl derivative organic materials such as $Li_2C_6O_6$,[14] 3, 4, 9, 10-perylene-tetracarboxylicacid-dianhydride sulfide polymer,[15] and poly (2,5-dihydoxy-1,4-benzoquinon-3,6-methylene).[16] Higher gravimetric capacitance due to the higher degree of oxidation was attributed to an increase in Faradaic reactions of surface functional groups on the functionalized graphene nano-platelets.

The specific capacitance values of the functionalized graphene nano-platelets (MFG sample) before and after heat treatment were compared to further confirm the role of functional groups in providing high capacitance. Functional groups on the MFG were further removed with heat treatment at 400°C without changing the morphology of graphene nano-platelets (Figure 3-10). Gravimetric current and capacitance values were decreased by a factor of ~0.3 after heat treatment (Figure 3-11c). As shown in Figure 3-11a and

Figure 3-12, heat treatment decreased the O/C ratio; thus, this experiment strongly suggests that the Faradaic reactions of functional groups with lithium ions are responsible for the large gravimetric capacitance of the functionalized graphene nano-platelets. Additionally, the linear relationship between the O/C ratio and gravimetric capacitance (Figure 3-11d) provides further evidence that the redox reactions of oxygen-containing functional groups with lithium ions primarily contributed to the high gravimetric capacitances.

The dependence of lithium storage capability on functionality was identified by potentio-galvanostat tests. Figure 3-13 shows that the specific capacity of the functionalized graphene nano-platelets increased according to the amount of functional groups. The specific capacities were ~239, 178, and 150 mAh g^{-1} for HFG, MFG, and LFG, respectively, at a current density of ~100 mA g^{-1}. The charge/discharge profiles of each sample were identical, indicating that they undergo an identical electrochemical reaction. The linear increase in specific capacity with increasing functional groups supports the proposed redox reaction mechanism between functional groups and lithium. To identify the redox center for lithium storage, *ex-situ* XPS and *ex-situ* FT-IR analysis were used (Figure 3-14, and Figure 3-15). It was found that the lithium ions are stored *via* the reaction with the C=O functional groups. Figure 3-14b reveals that the lithium ions were stored in in the discharged state. Correspondingly, XPS peak from C=O functional group was reduced and that from C-O functional group was substantially increased in Figure 3-14c. This indicates the lithium ions were stored at C=O functional groups by

breaking the double bonds and forming the single bonds between carbon and oxygen.

Cycle stability of the electrodes was tested for 100 cycles, where no noticeable capacity fading was observed with high Coulombic efficiencies (Figure 3-16). A long-lasting cyclability test was also conducted with the MFG sample at a current density of 1 A g^{-1}. Figure 3-17 shows that the MFG sample can be tested over 2,000 cycles without capacity degradation. Field-emission scanning electron microscopy (FE-SEM) and FT-IR analysis of the cycled electrodes indicated that there were no distinctive changes in morphology and surface functional groups such as C=O, which further supports superior cycle stability (Figure 3-18). Excellent cycle stability is thought to be related to stable covalent bonding of surface functional groups on the functionalized graphene nano-platelets and lithium storage without significant volume change, which is typically observed in intercalation-based cathodes.

Functionalized graphene nano-platelets may also exhibit a respectably high rate capability depending on the degree of functionalization. At a current rate of 2.0 A g^{-1}, HFG, MFG, and LFG delivered 175, 150, and 125 mAh g^{-1}, respectively. Even at 10 A g^{-1}, all the samples delivered ~100 mAh g^{-1}. The exceptional rate capability was attributed to the porous morphology of the functionalized graphene nano-platelets, allowing the electrolyte to easily penetrate into the pores, thus improving lithium ion transport from the electrolyte to the functionalized graphene nano-platelets. It should be noted that, compared to the capacities delivered at a low current

rate, higher rate performance was found in less oxidized samples (Figure 3-19). It is believed that at high current densities, slight differences in the electrical conductivity of the samples led to substantial differences in rate performance. Figure 3-20 and 2-21 show that electrical conductivity increased with decreasing functional group content. The highest power performance was obtained from LFG, while the highest energy density was achieved with HFG. This indicates that power and energy density can be tuned simply by controlling the functional group content on graphene nano-platelets.

The dependence of power and energy density on functionalization is clearly shown in the Ragone plot of Figure 3-22. The power capability of the functionalized graphene nano-platelets was reduced with an increasing degree of oxidation. Nevertheless, HFG still exhibited a very high gravimetric energy of ~250 Wh kg^{-1} at a gravimetric power over 10 kW kg^{-1} (at few minutes charge/discharge rate). The gravimetric energy of the functionalized graphene nano-platelets approached that of a commercially available high-power $LiMn_2O_4$ cathode. At current rates higher than 6 kW kg^{-1}, the functionalized graphene nano-platelets delivered significantly greater gravimetric energy (>1.5 – 1.8 times) than $LiMn_2O_4$ nanowires having the highest reported power capability.[17]

The high gravimetric energy and power were attributed to the fast surface Faradaic reaction between functional groups and lithium ions combined with the three-dimensional network framework of the functionalized graphene nano-platelets (Figure 3-23) and high electrical

conductivity throughout the graphitic region (Figure 3-23b). The lithium storage occurs at functional groups on the surface or at the edge of the graphene nano-platelets. It means that the delivery of lithium ions and electrons to the surface is likely the limiting factor for the electrochemical reaction similarly with Ref. 8. Therefore, it is important to form porous morphology to facilitate the accessibility of electrolyte to the electrode material. The suitable control of the electrode architecture by increasing active surface area with a stable interconnection of the electrode is expected to further increase the electrochemical performance of electrode materials based on C=O redox centers.

3.1.4 Conclusion

Functionalized graphene nano-platelets derived from a simple mass-scalable chemical method were found to be extremely promising as an electrode material for rechargeable batteries that can deliver high gravimetric energies (~250 Wh kg^{-1}) at a power over 20 kW kg^{-1} for more than a thousand cycles. Moreover, we have demonstrated that gravimetric energy and power can be simply tuned by controlling the degree of oxidation, suggesting that further development of the electrode based on the same chemistry is possible. Low material cost and simple fabrication, combined with the tunable high power and energy density of this new class of cathodes, will open up new possibilities for the development of high-performance energy storage devices for various applications.

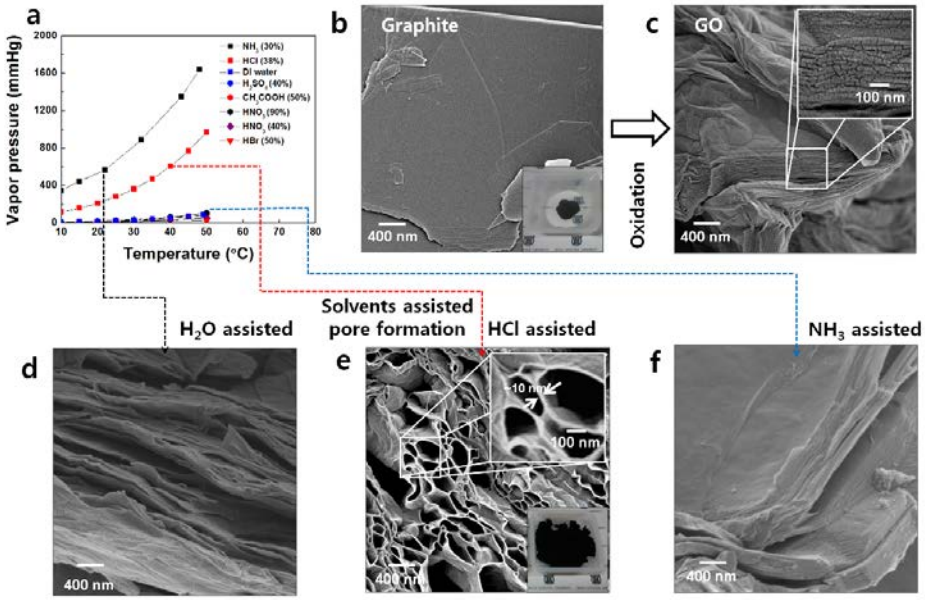

Figure 3-1. Solvent-assisted pore formation of the functionalized graphene nano-platelets. a. Vapor pressures of various solvents (NH_3, HCl, water, H_2SO_4, CH_3COOH, HNO_3, HBr) from 10 to 50°C, obtained from literature data (Ref. 35). **b.** FE-SEM images of pristine graphite (inset: photo of pristine graphite). **c.** GO oxidized from pristine graphite. FE-SEM images of GO samples that were assisted by **d.** H_2O, **e.** HCl (inset: photo of HCl-assisted sample after annealing), and **f.** NH_3. NH_3- and H_2O-assisted samples do not show porous morphology; the HCl-assisted sample had pores (a few hundred nanometers in diameter).

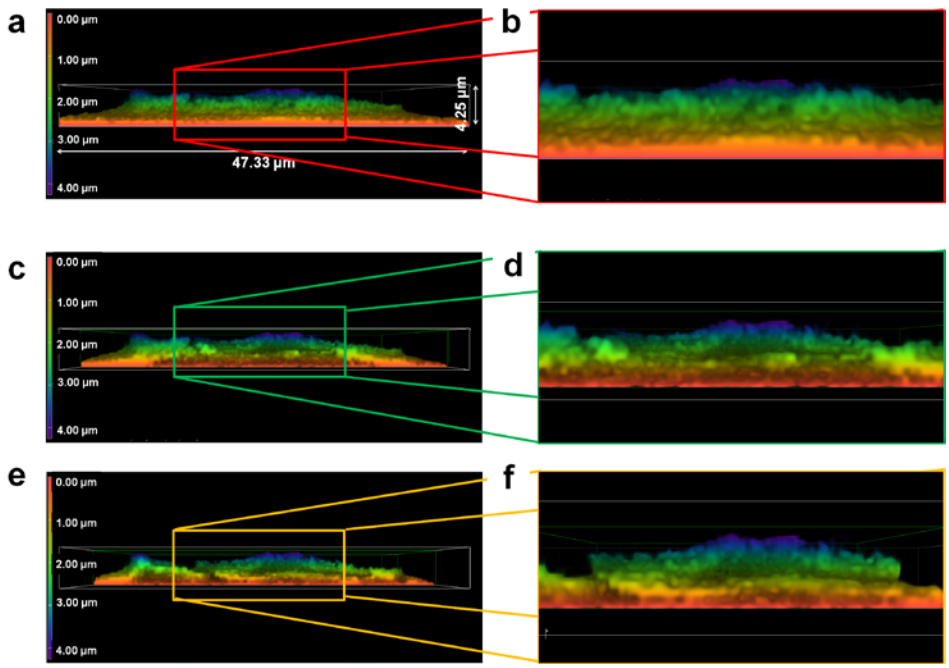

Figure 3-2. The cross-sectional images of the functionalized graphene cathode for as drop-casted (**a** and **b**) and after slicing the sample to investigate the internal structure (**c** – **f**).

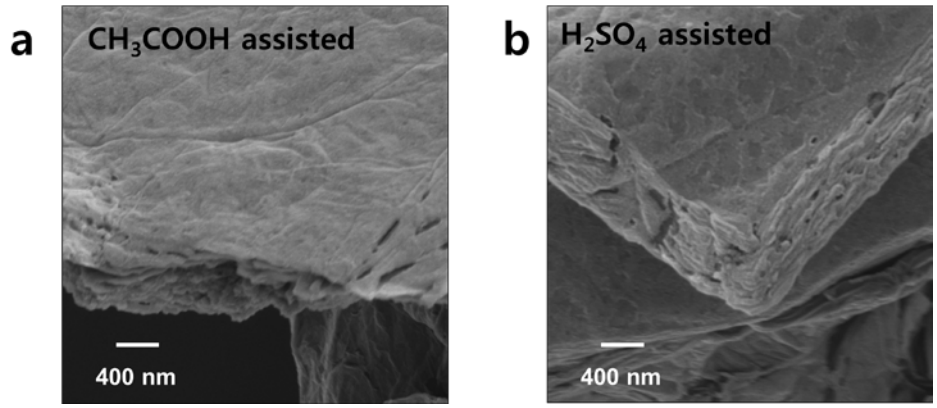

Figure 3-3. FE-SEM images of GO samples that were assisted by **a.** CH_3COOH and **b.** H_2SO_4.

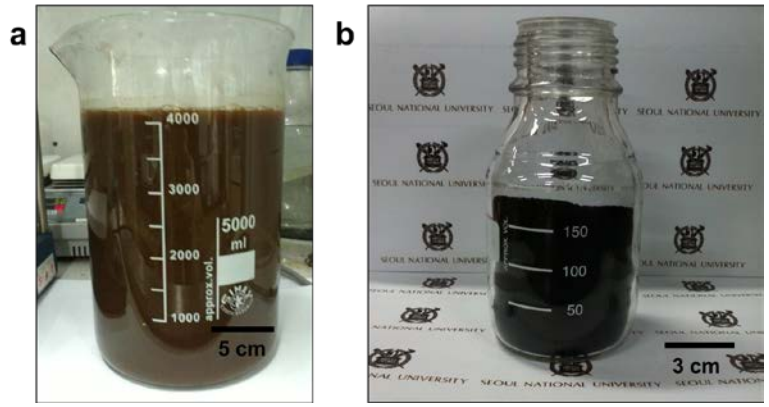

Figure 3-4. Demonstration of scalability of the functionalized graphene nano-platelets. a. GO slurry before filtering process (using 30 g of graphite) and **b.** funtionalized graphene nano-platelets after low temperature (120 ˚C) heat treatment (approximately 28.5 g, e.g. 95 % yield from 30 g of graphite).

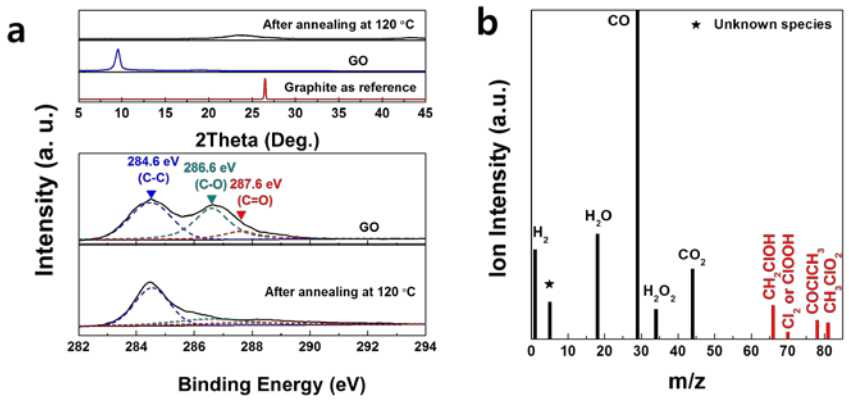

Figure 3-5. Pore formation and reduction mechanism. a. XRD (above) and XPS (bottom) analysis results for GO and functionalized graphene nano-platelets after annealing at 120°C **b.** MS analysis result of gases that evolved after HCl-treated GO sample were heated at 120°C. Gas species with high molecular weights were thought to be Cl-containing molecules such as CH_2ClOH, ClOOH, $CCOClCH_3$, and CH_3ClO_2, which explains the reduction effects of HCl on GO.

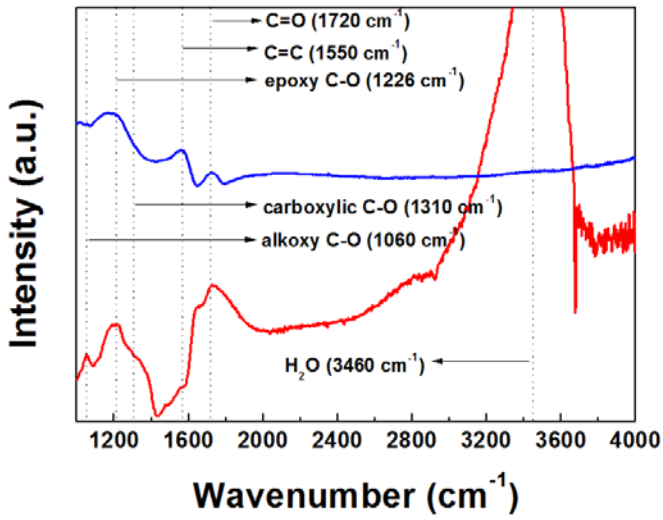

Figure 3-6. FT-IR spectra of GO (red) and functionalized graphene nano-platelets (blue).

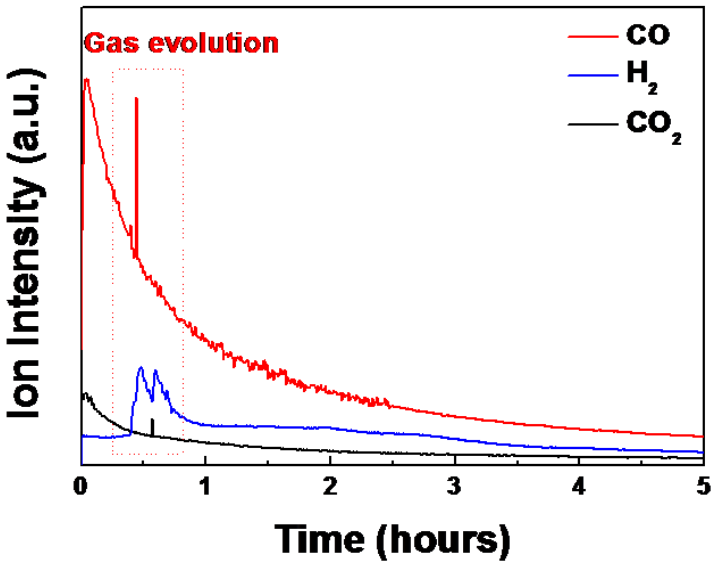

Figure 3-7. ***In-situ*** **MS analysis result of HCl-treated samples** annealed at less than 120°C.

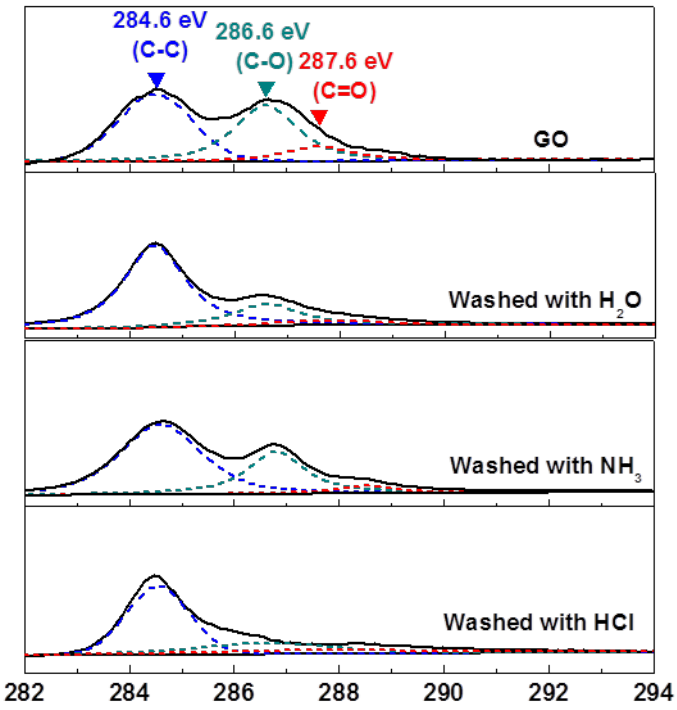

Figure 3-8. XPS spectra of H_2O-washed, NH_3-washed GO and HCl-washed samples after heat treatment at 120°C.

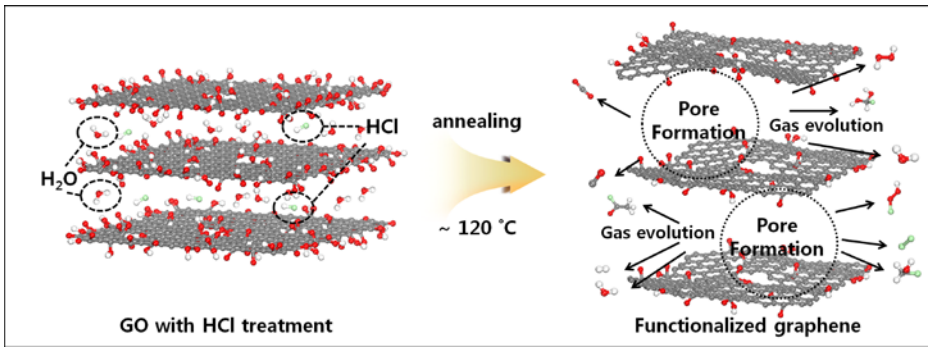

Figure 3-9. Schematic drawing of the pore formation and reduction mechanism.

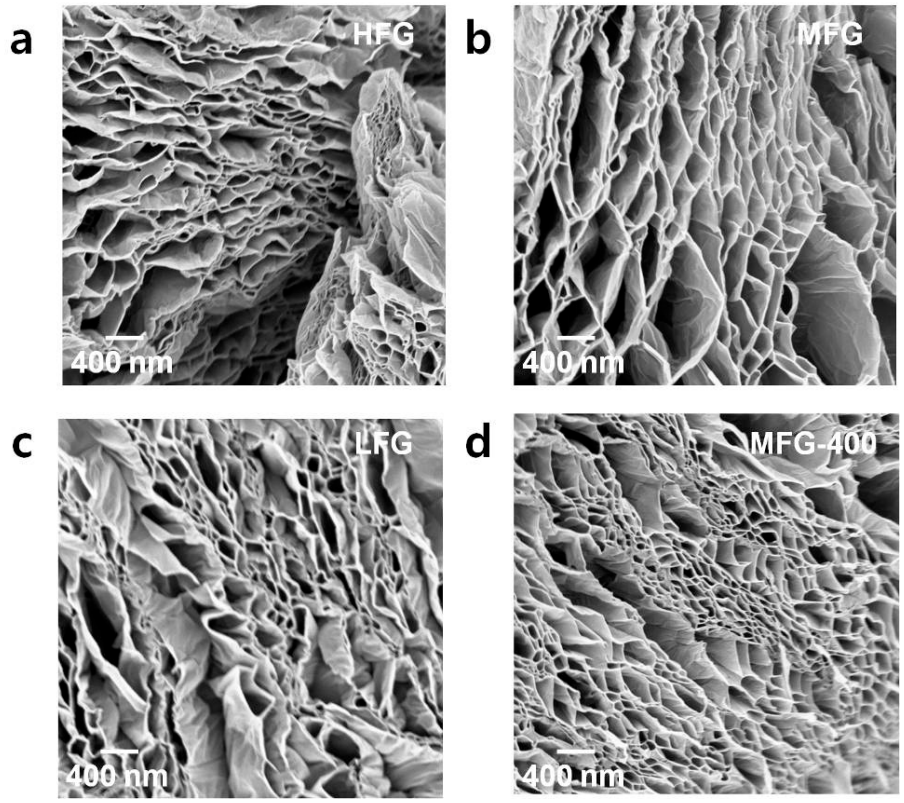

Figure 3-10. FE-SEM images of HFG, MFG, LFG, and MFG-400 samples. FE-SEM images of **a.** HFG, **b.** MFG, **c.** LFG, and **d.** MFG-400 samples. Functionalities were controlled by adjusting the amount of oxidizing agent and subsequent heat treatment; however, their porous morphologies did not change significantly.

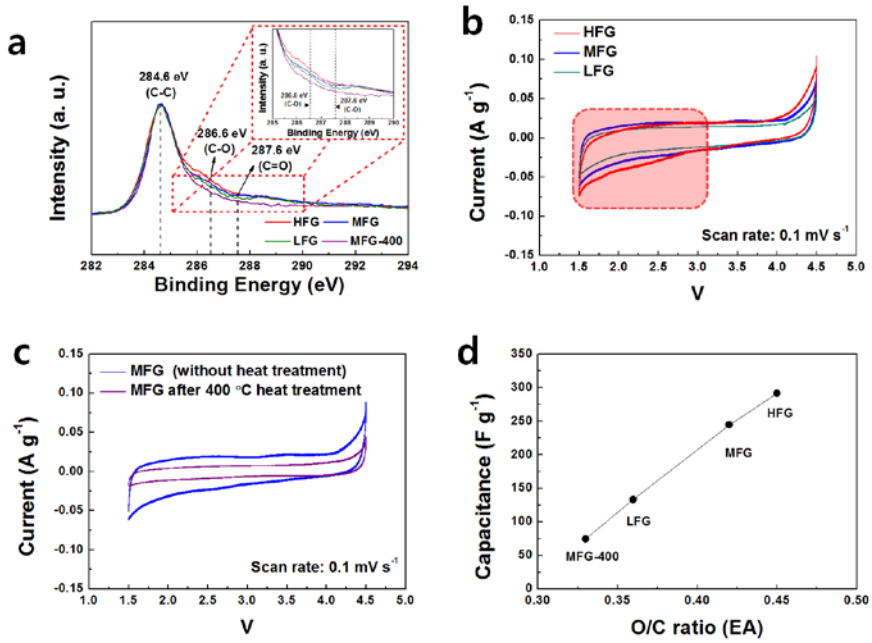

Figure 3-11. Functionality-dependant electrochemical behavior of the functionalized graphene nano-platelets. a. XPS C 1*s* spectra of the functionalized graphene nano-platelets with different degrees of oxidation. **b.** CV data for the functionalized graphene nano-platelet samples over a voltage range from 1.5 to 4.5 V with a scan rate of 0.1 mV s^{-1}. **c.** CV data for the functionalized graphene nano-platelets with and without heat treatment at 400°C under an Ar atmosphere for 6 h. **d.** Relationship between the O/C ratio and gravimetric capacitance, which indicates that the gravimetric capacitance increased linearly with the O/C ratio of the functionalized graphene nano-platelets.

	O/C ratio (XPS)	O/C ratio (EA)
GO	1.26	1.12
HFG	0.47	0.45
MFG	0.34	0.42
LFG	0.30	0.36
MFG-400	0.28	0.33

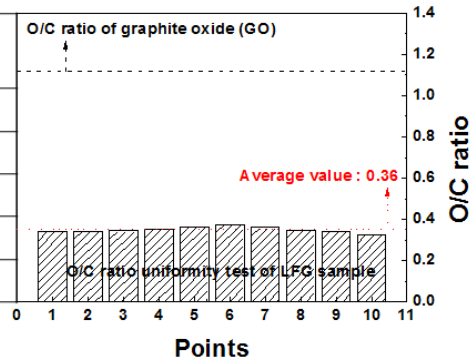

Figure 3-12. O/C ratio analysis of the functionalized graphene nano-platelets and O/C ratio uniformity. O/C ratio analysis data obtained from XPS and EA (left table). (The differences in the O/C ratios for XPS and EA results were related to the analysis conditions, *i.e.*, vacuum and ambient air atmospheres. The trend in the O/C ratio for the two techniques was consistent.) The O/C ratio uniformity of the LFG sample was tested using the EA (right figure). Ten points were randomly collected from the LFG sample. The O/C ratio shows only a small variation from the average value of 0.36.

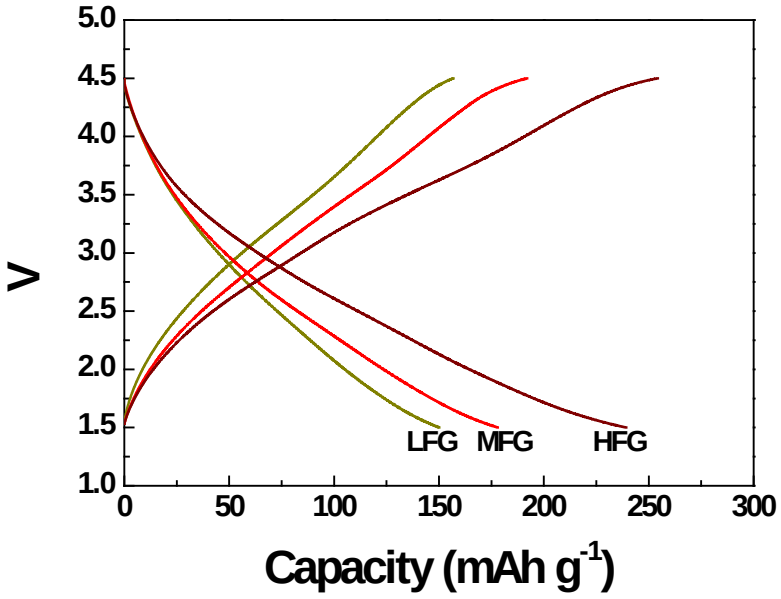

Figure 3-13. Charge/discharge profiles of the samples in which the profile shapes of the samples are similar to one another, demonstrating that the electrochemical reaction mechanism of each sample is similar.

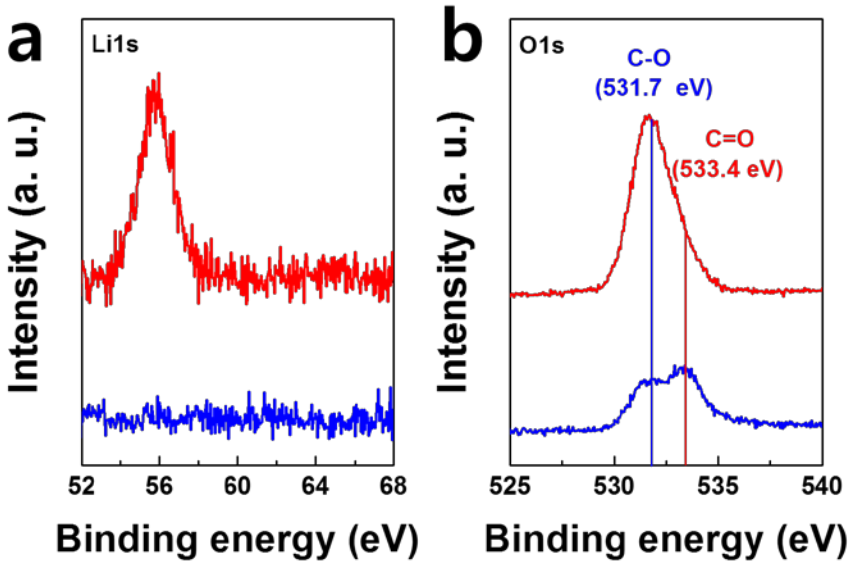

Figure 3-14. Ex-situ XPS analyses a. *Ex-situ* XPS in Li1s region shows lithium ions are stored after discharge, **b.** *Ex-situ* XPS in O1s region reveals that the C=O functional group becomes C-O after discharge process, indicating C=O functional group is the redox center for lithium storage.

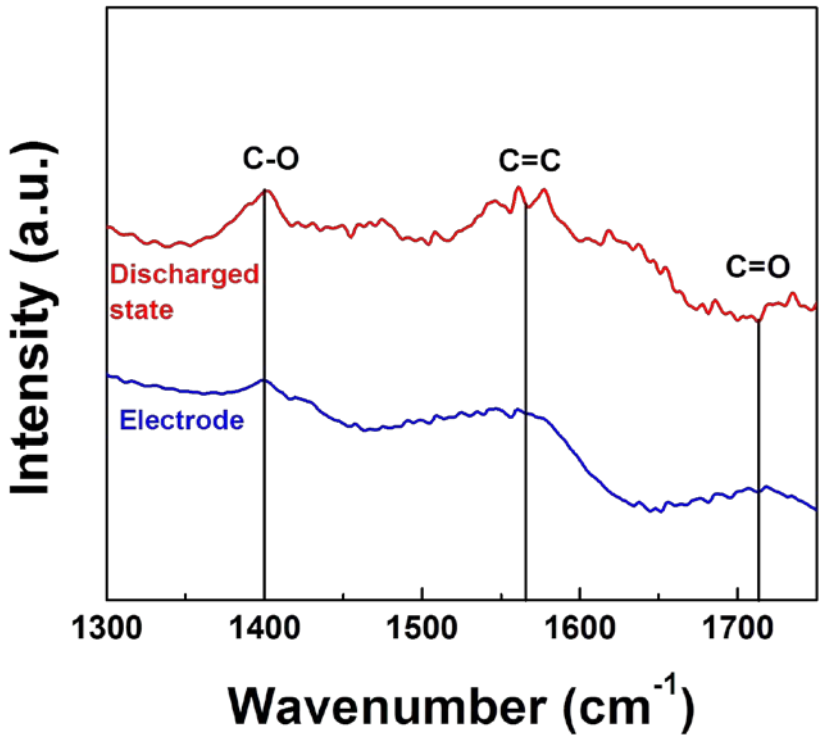

Figure 3-15. *Ex-situ* FTIR analysis identifies that the C=O functional group participates in the lithium storage.

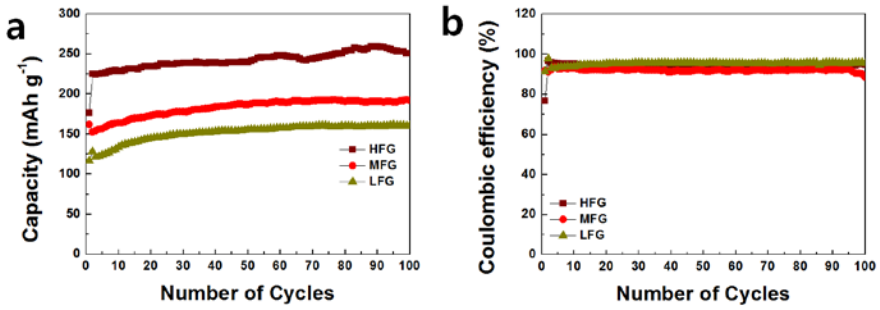

Figure 3-16. Cycle stability data over a voltage range from 1.5 to 4.5 V with a current rate of 0.1 A g^{-1}. a. Discharge capacities and **b.** Coulombic efficiency of HFG, MFG, and LFG samples up to 100 cycles.

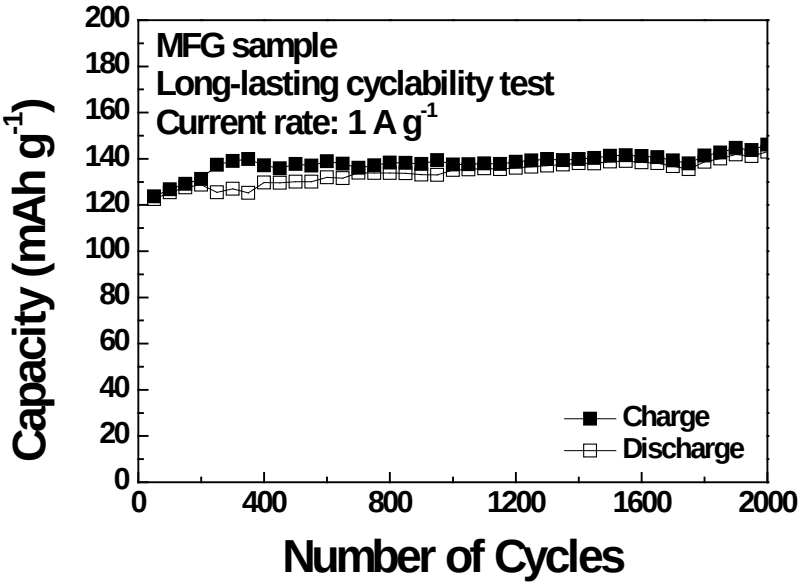

Figure 3-17. Long-lasting cyclability test of the MFG sample at a high current rate of 1 Ag^{-1} up to 2,000 cycles.

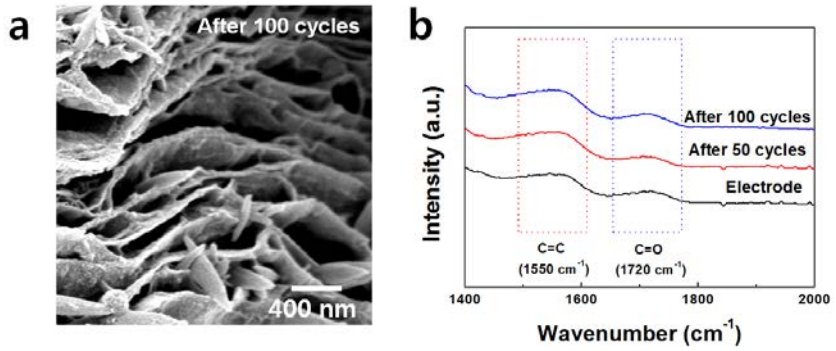

Figure 3-18. Morphology and chemical composition stability during battery cycling. a. SEM and **b.** FT-IR analysis results after battery cycling, which demonstrate cycle stability of the functionalized graphene sheet.

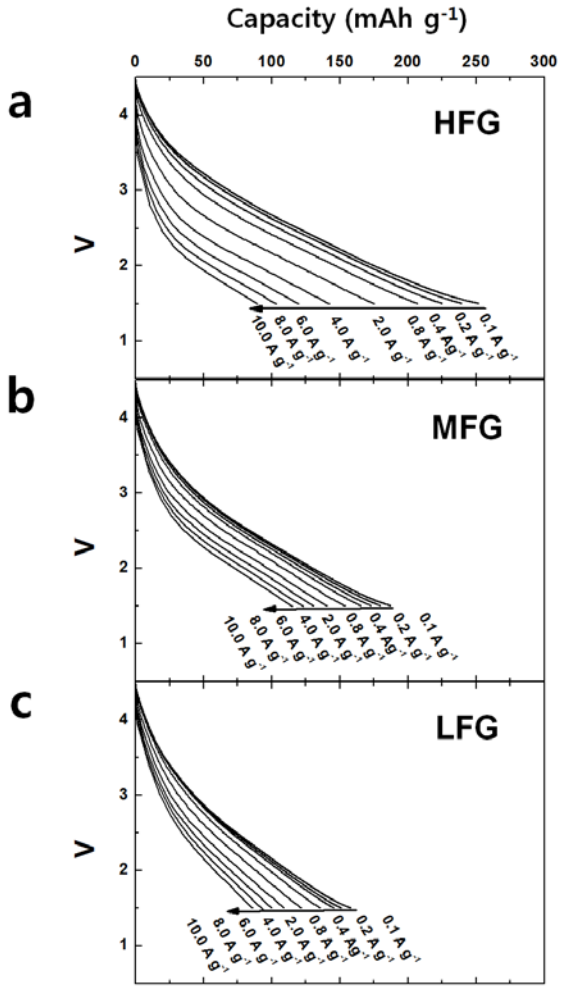

Figure 3-19. Discharge profiles at various current rates from 0.1 to 10.0 A g^{-1} of **a.** HFG, **b.** MFG, and **c.** LFG samples. While HFG exhibits large specific capacity at low current rates, MFG and LFG show better capacity retention properties at higher current rates.

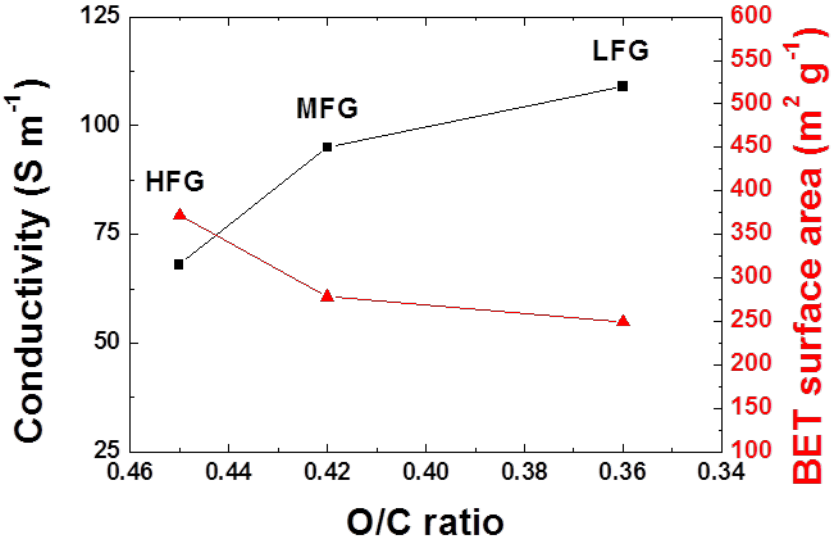

Figure 3-20. Electrical conductivities and BET surface areas of HFG, MFG, LFG, and MFG-400 samples. Electrical conductivities ranged from 68 to 114 S m^{-1} and BET surface areas ranged from 249 to 371 m^2 g^{-1}.

	HFG	MFG	LFG
Conductivity (S m^{-1})	68	95	109
BET surface area (m^2 g^{-1})	371.4232	278.3184	249.1466

Figure 3-21. Electrical conductivities and BET surface areas of HFG, MFG, LFG, and MFG-400 samples.

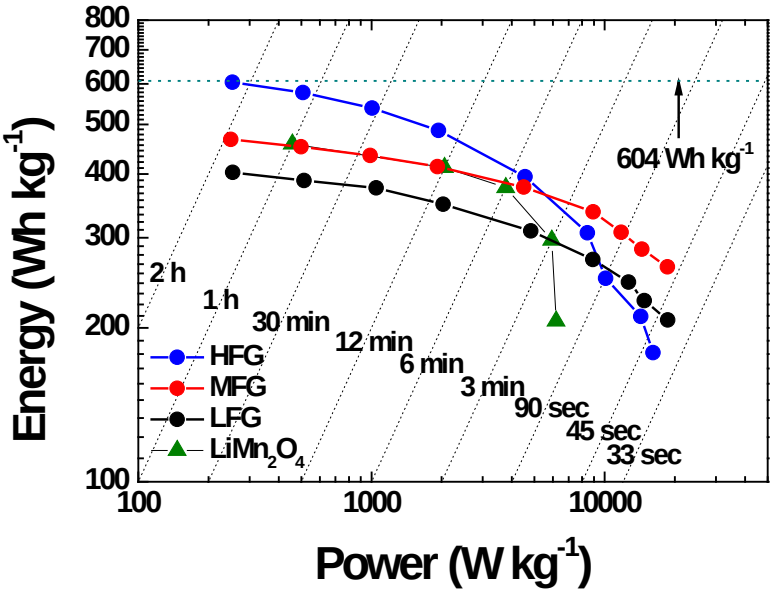

Figure 3-22. Ragone plot for the functionalized graphene nano-platelet electrodes with different amounts of functional groups; a conventional electrode material, $LiMn_2O_4$, is shown for comparison. Only the functionalized graphene nano-platelet weight was considered in the gravimetric energy and power calculations.

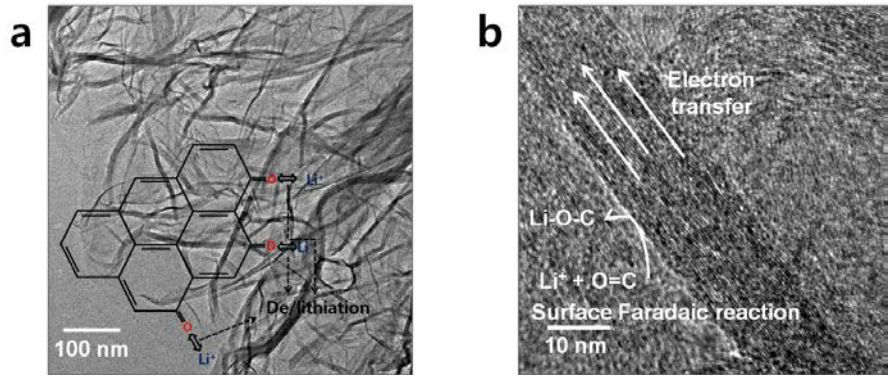

Figure 3-23. HR-TEM images of the functionalized graphene nano-platelets. a. Three-dimensional network structure of the functionalized graphene nano-platelets confirmed by HR-TEM analysis and a schematic drawing of the proposed surface Faradaic reactions on the functionalized graphene nano-platelets (inset). **b.** Magnified HR-TEM image of the functionalized graphene nano-platelets where graphitic regions act as electron transfer paths and surfaces contribute to the surface Faradaic reaction.

3.1.5 References

1. Perry, R. H., Green, D. W. *Perry's chemical engineers' handbook*, 7th ed., New York, McGraw-Hill. **1997**

2. Dikin, D. A. *et al.* Preparation and characterization of grahene oxide paper. *Nature* **2007**, 448, 457-460.

3. Park, S. *et al.* Aqueous suspension and characterization of chemically modified graphene sheets. *Chem. Mater.* **2008**, 20, 6592-6594.

4. Park, S. *et al.* Colloidal suspensions of highly reduced graphene oxide in a wide variety of organic solvents. *Nano Lett.* **2009**, 9, 1593-1597.

5. Yuan, Y. F., Xia, X. H., Yang, J. L., Chen, Y. B., Guo, S. Y. Hierarchically ordered porous nickel oxide array film with enhanced electrochemical properties for lithium ion batteries. *Electrochem. Commun.* **2010**, 12, 890-893.

6. Demir-Cakan, R., Hu, Y. –S., Antonietti, M., Maier, J., Titirici, M. –M. Facile one-pot synthesis of mesoporous SnO_2 microspheres via nanoparticles assembly and lithium storage properties. *Chem. Mater.* **2008**, 20, 1227-1229.

7. Kim, H. *et al.* Nano-graphite platelet loaded with $LiFePO_4$ nanoparticles used as the cathode in a high performance Li-ion battery. *Carbon* **2012**, 50, 1966-1971.

8. Kim, H. *et al.* Graphene-based hybrid electrode material for high-power lithium-ion batteries. *J. Electrochem. Soc.* **2011**, 158, A930-A935.

9. Stanokovich, S. *et al.* Synthesis of graphene-based nano-plateletss via chemical reduction of exfoliated graphite oxide. *Carbon* **2007**, 45, 1558-1565.

10. Dreyer, D. R., Park, S., Bielawski, C. W., Ruoff, R. S. The chemistry of graphene oxide. *Chem. Soc. Rev*. **2010**, 39, 228-240.

11. Park, S. *et al.* Chemical structures of hydrazine-treated graphene oxide and generation of aromatic nitrogen doping. *Nat. Commun.* **2012**, 3, 638

12. Zhu, Y *et al.* Exfoliation of graphite oxide in propylene carbonate and thermal reduction of the resulting graphene oxide platelets. *ACS Nano* **2010**, 4, 1227-1233.

13. Lu, G., Ocola, L. E., Chen, J. Reduced graphene oxide for room-temperature gas sensors. *Nanotechnology* **2009**, 20, 445502

14. Chen, H. *et al.* From biomass to a renewable $Li_xC_6O_6$ organic electrode for sustainable Li-ion batteries. *ChemSusChem* **2008**, 1, 348-355.

15. Han, X., Chang, C., Yuan, L., Sun, T., Sun, J. Aromatic carbonyl derivative polymers as high-performance Li-ion storage materials. *Adv. Mater.* **2007**, 19, 1616-1621.

16. Gall, T. L., Reiman, K. H., Grossel, M. C., Owen, J. R. Poly(2,5-dihydroxy-1,4-benzoquinon-3,6-methylene): a new organic polymer as positive electrode material for rechargeable lithium batteries. *J. Power Sources* **2003**, 119-121, 316-320.

17. Lee, H. –W. *et al.* Ultrathin spinel $LiMn_2O_4$ nanowires as high power cathode materials for Li-ion batteries. *Nano Lett.* **2010**, 10, 3852-3856.

3.2 Functionalized graphene for Na rechargeable batteries

(The content of this chapter has been published in *Nano Energy*, 4, 97 (2014) DOI:10.1016/j.nanoen.2013.12.009. Reprinted from H. Kim *et al.* Novel transition-metal-free cathode for high energy and power sodium rechargeable batteries. *Nano Energy*, 4, 97 (2014) with permission from Elsevier. Copyright 2014.)

3.2.1 Research background

Developing a reliable energy storage system (ESS) is one of the most important issues in moving toward a sustainable society.[1-3] Because electricity production from renewable energy (*i.e.* solar, wind and geothermal energy) does not coincide with consumption time, the ESS is required to account for the discrepancy. Lithium ion batteries (LIBs) have been considered as the leading candidates for large-scale ESS due to their relatively high energy, power density and stable cyclability.[4-9] Nevertheless, the high cost of LIBs (partly due to the use of transition metals such as Co and Ni), and the arguable shortage of Li resources can limit their applications.[10-14]

In the respect of materials cost, this issue can be addressed by exploring energy storage chemistry based solely on earth-abundant elements. Recently, Na ion batteries (NIBs) have been extensively studied as an alternative to LIBs, since Na is earth-abundant and shares similar chemical properties with

Li. Recent studies on NIB have reported an electrochemical performance comparable to LIB.[15-17] However, NIB at present uses cathodes based on transition metal redox elements, which are typically much more expensive than Li or Na and account for the majority of the cathode cost. This significantly dilutes the cost merit of NIB. Furthermore, during the battery operation, the larger ionic size of Na than Li induces large lattice expansion and contraction during insertion and extraction in typical intercalation compounds, which can lead to the slow Na diffusion and cause cycle deterioration.[13, 18-20]

In resolving these issues and taking advantage of cost-effective Na chemistry, here, we propose a novel NIB cathode based on a transition-metal-free carbonaceous material with a non-intercalation-based Na storage mechanism. Starting from natural graphite, functionalized graphite nanoplatelets were fabricated *via* simple scalable routes. By adopting surface reactions between Na and functionalized graphite nanoplatelets, (i) no significant lattice change occurred during battery cycling, and (ii) much faster Na kinetics could be achieved without solid-state diffusion.[21-22] Furthermore, the high electrical conductivity of carbonaceous materials could aid in improving the rate capability.[23-24] While previous studies of graphite-based electrodes are found in anode applications for NIB,[25-26] this work manipulated the material to store Na ions within an acceptable cathode potential by chemical modification.

3.2.1.1 References

1. Tarascon, J. M.; Armand, M. Issues and challenges facing rechargeable lithium batteries. *Nature* **2001,** *414*, 359-367.

2. Han, J.; Zhang, L. L.; Lee, S.; Oh, J.; Lee, K.-S.; Potts, J. R.; Ji, J.; Zhao, X.; Ruoff, R. S.; Park, S. Generation of B-Doped Graphene Nanoplatelets Using a Solution Process and Their Supercapacitor Applications. *ACS Nano* **2012,** *7*, 19-26.

3. Guo, W.; Yin, Y.-X.; Xin, S.; Guo, Y.-G.; Wan, L.-J. Superior radical polymer cathode material with a two-electron process redox reaction promoted by graphene. *Energy Environ. Sci.* **2012,** *5*, 5221-5225.

4. Zhao, L.; Hu, Y.-S.; Li, H.; Wang, Z.; Chen, L. Porous Li4Ti5O12 Coated with N-Doped Carbon from Ionic Liquids for Li-Ion Batteries. *Adv. Mater.* **2011,** *23*, 1385-1388.

5. Hsu, K.-F.; Tsay, S.-Y.; Hwang, B.-J. Synthesis and characterization of nano-sized LiFePO4 cathode materials prepared by a citric acid-based sol-gel route. *J. Mater. Chem.* **2004,** *14*, 2690-2695.

6. Kang, K.; Meng, Y. S.; Bréger, J.; Grey, C. P.; Ceder, G. Electrodes with High Power and High Capacity for Rechargeable Lithium Batteries. *Science* **2006,** *311*, 977-980.

7. Lu, J.; Peng, Q.; Wang, W.; Nan, C.; Li, L.; Li, Y. Nanoscale Coating of LiMO2 (M = Ni, Co, Mn) Nanobelts with Li+-Conductive Li2TiO3: Toward Better Rate Capabilities for Li-Ion Batteries. *J. Am. Chem. Soc.* **2013,** *135*, 1649-1652.

8. Oumellal, Y.; Rougier, A.; Nazri, G. A.; Tarascon, J. M.; Aymard, L.

Metal hydrides for lithium-ion batteries. *Nat. Mater.* **2008,** *7*, 916-921.

9. Kim, J.-S.; Kim, K.; Cho, W.; Shin, W. H.; Kanno, R.; Choi, J. W. A Truncated Manganese Spinel Cathode for Excellent Power and Lifetime in Lithium-Ion Batteries. *Nano Lett.* **2012,** *12*, 6358-6365.

10. Tarascon, J.-M. Is lithium the new gold? *Nat. Chem.* **2010,** *2*, 510-510.

11. Sun, Y.; Zhao, L.; Pan, H.; Lu, X.; Gu, L.; Hu, Y.-S.; Li, H.; Armand, M.; Ikuhara, Y.; Chen, L., et al. Direct atomic-scale confirmation of three-phase storage mechanism in Li4Ti5O12 anodes for room-temperature sodium-ion batteries. *Nat. Commun.* **2013,** *4*, 1870.

12. Kim, S.-W.; Seo, D.-H.; Ma, X.; Ceder, G.; Kang, K. Electrode Materials for Rechargeable Sodium-Ion Batteries: Potential Alternatives to Current Lithium-Ion Batteries. *Adv. Energy Mater.* **2012,** *2*, 710-721.

13. Cao, Y.; Xiao, L.; Wang, W.; Choi, D.; Nie, Z.; Yu, J.; Saraf, L. V.; Yang, Z.; Liu, J. Reversible Sodium Ion Insertion in Single Crystalline Manganese Oxide Nanowires with Long Cycle Life. *Adv. Mater.* **2011,** *23*, 3155-3160.

14. Komaba, S.; Murata, W.; Ishikawa, T.; Yabuuchi, N.; Ozeki, T.; Nakayama, T.; Ogata, A.; Gotoh, K.; Fujiwara, K. Electrochemical Na Insertion and Solid Electrolyte Interphase for Hard-Carbon Electrodes and Application to Na-Ion Batteries. *Adv. Funct. Mater.* **2011,** *21*, 3859-3867.

15. Saravanan, K.; Mason, C. W.; Rudola, A.; Wong, K. H.; Balaya, P. The First Report on Excellent Cycling Stability and Superior Rate Capability of Na3V2(PO4)3 for Sodium Ion Batteries. *Adv. Energy Mater.* **2013,** *3*, 444-

450.

16. Wang, L.; Lu, Y.; Liu, J.; Xu, M.; Cheng, J.; Zhang, D.; Goodenough, J. B. A Superior Low-Cost Cathode for a Na-Ion Battery. *Angew. Chem. Int. Ed.* **2013,** *52*, 1964-1967.

17. Yabuuchi, N.; Kajiyama, M.; Iwatate, J.; Nishikawa, H.; Hitomi, S.; Okuyama, R.; Usui, R.; Yamada, Y.; Komaba, S. P2-type Nax[Fe1/2Mn1/2]O2 made from earth-abundant elements for rechargeable Na batteries. *Nat. Mater.* **2012,** *11*, 512-517.

18. Zhu, Y.; Xu, Y.; Liu, Y.; Luo, C.; Wang, C. Comparison of electrochemical performances of olivine NaFePO4 in sodium-ion batteries and olivine LiFePO4 in lithium-ion batteries. *Nanoscale* **2013,** *5*, 780-787.

19. Casas-Cabanas, M.; Roddatis, V. V.; Saurel, D.; Kubiak, P.; Carretero-Gonzalez, J.; Palomares, V.; Serras, P.; Rojo, T. Crystal chemistry of Na insertion/deinsertion in FePO4-NaFePO4. *J. Mater. Chem.* **2012,** *22*, 17421-17423.

20. Sauvage, F.; Laffont, L.; Tarascon, J. M.; Baudrin, E. Study of the Insertion/Deinsertion Mechanism of Sodium into Na0.44MnO2. *Inorg. Chem.* **2007,** *46*, 3289-3294.

21. Kim, H.; Lim, H.-D.; Kim, S.-W.; Hong, J.; Seo, D.-H.; Kim, D.-c.; Jeon, S.; Park, S.; Kang, K. Scalable Functionalized Graphene Nano-platelets as Tunable Cathodes for High-performance Lithium Rechargeable Batteries. *Sci. Rep.* **2013,** *3*, 1506.

22. Lee, S. W.; Yabuuchi, N.; Gallant, B. M.; Chen, S.; Kim, B.-S.; Hammond, P. T.; Shao-Horn, Y. High-power lithium batteries from

functionalized carbon-nanotube electrodes. *Nat. Nanotechnol.* **2010,** *5*, 531-537.

23. Kawabe, Y.; Yabuuchi, N.; Kajiyama, M.; Fukuhara, N.; Inamasu, T.; Okuyama, R.; Nakai, I.; Komaba, S. Synthesis and electrode performance of carbon coated Na2FePO4F for rechargeable Na batteries. *Electrochem. Commun.* **2011,** *13*, 1225-1228.

24. Oh, S.-M.; Myung, S.-T.; Hassoun, J.; Scrosati, B.; Sun, Y.-K. Reversible NaFePO4 electrode for sodium secondary batteries. *Electrochem. Commun.* **2012,** *22*, 149-152.

25. Wang, Y.-X.; Chou, S.-L.; Liu, H.-K.; Dou, S.-X. Reduced graphene oxide with superior cycling stability and rate capability for sodium storage. *Carbon* **2013,** *57*, 202-208.

26. Wang, Z.; Qie, L.; Yuan, L.; Zhang, W.; Hu, X.; Huang, Y. Functionalized N-doped interconnected carbon nanofibers as an anode material for sodium-ion storage with excellent performance. *Carbon* **2013,** *55*, 328-334.

3.2.2 Experiments

Graphite oxide (GO) was first fabricated by modifying the Hummers method.[1] Graphite (5 g) was dispersed in a solution of $NaNO_3$ (5 g) and H_2SO_4 (225 mL), which was stirred for 30 min in an ice bath. $KMnO_4$ (30 g) was added to the resulting solution, followed by stirring at 50˚C for 2 h. Deionized (DI) water (500 mL) and H_2O_2 (30 mL, 35%) were slowly added to the solution. The solution was filtered and washed with HCl (750 mL, 10%). Additional washing/filtering was performed using concentrated HCl (500 mL, 37%) to retrieve the GO powder. The samples were annealed at 120˚C for 6 h to generate the functionalized graphite nanoplatelets.

The structure of the functionalized graphite nanoplatelet was analyzed with an X-ray diffractometer (XRD, D2PHASER) using Cu Kα radiation. X-ray photoelectron spectroscopy (XPS, AXIS-HSi) was used to quantify the functionals in the samples. Morphology was examined using field-emission scanning electron microscopy (FE-SEM, SUPRA 55VP) and high-resolution transmission electron microscopy (HR-TEM, JEM-3000F). A focused ion beam (FIB, AURIGA) was used at 30 kV and 600 pA after Pt coating. The carbon structure was analyzed using a high-resolution dispersive Raman microscope (LabRAM HR UV/Vis/NIR). The surface area and pore volume were determined using the Brunauer-Emmett-Teller (BET) method. Electrochemical impedance spectroscopy (EIS) data were recorded from 1 MHz to 100 mHz using a potentiostat/galvanostat (VSP-300, Bio-Logic, France).

Electrodes were prepared by mixing the active material (70 wt%) with

polyvinylidene fluoride binder (20 wt%) and super-P (10 wt%) in an *N*-methyl-2-pyrrolidone solvent. The resulting slurry was uniformly pasted onto Al foil, dried at 120°C for 2 h, and then roll-pressed. A total of 1-2 mg cm^{-2} of the active material was loaded onto the electrode. Test cells were assembled into a two-electrode configuration with a Na metal counter electrode (Sigma-Aldrich), a glass microfiber filter separator (grade FG/G; Whatman, USA), and an electrolyte of 1 M $NaBF_4$ or $NaClO_4$ in propylene carbonate (PC, Sigma-Aldrich) in a glove box. Electrochemical profiles were obtained over a voltage range of 4.3 V to 1.0 V using a multichannel potentio-galvanostat (WBCS 3000, WonATech).

3.2.3 Results and discussion

Functionalized graphite nanoplatelets were synthesized by the controlled reduction of graphite oxides (GO) with a low-temperature annealing in the presence of residual HCl. After chemical oxidation, the XRD peak of pristine graphite (002) shifted to a lower angle, indicative of expansion of graphene interlayers as a result of a large amounts of C-O or C=O formation in the graphite (Figure 3-24a).[2] However, the characteristic XRD peak of GO disappeared after the annealing process at 120˚C, shown as the upper blue pattern in Figure 3-24a. This implied that C-O or C=O functional groups were removed and the long-range ordering along the perpendicular direction of basal graphene planes was lost at this temperature.[3] XPS analysis in Figure 3-24b and c confirmed the partial reduction of GO, in which the amount of functional groups of C-O (286.6 eV) and C=O (287.6 eV) were significantly reduced.[4] The partially reduced sample was further analyzed by Raman spectroscopy and compared with the pristine graphite. Figure 3-25 shows significant changes in both G and D bands. The broadened G band and the high intensity D band indicates that the sample contained significant amount of defects.[5]

It was noted that the annealing process of GO led to a dramatically different morphology. The FE-SEM and HR-TEM analysis in Figure 3-26d-g shows that the pristine graphite structure was partially exfoliated into the assembled thin layers of graphite (~10 nm), forming a two-dimensionally porous structure. It was observed that the pores were present throughout the sample, as shown in Figure 3-26f-g and 2-27 (hereafter we call the sample

functionalized graphite nanoplatelet.) In our previous study, we attributed the formation of these pores at such low temperatures (120˚C) to the rapid gas evolution of high-concentration HCl solution from GO. The HCl solution trapped in the interlayer galleries exhibited strong exfoliation capability because of the increased vapor pressure.[6] The gas escape paths are expected to make the pores interconnected throughout the sample. The pore analysis by N_2 adsorption and desorption revealed mesopores with a pore volume of 0.922 cm^3g^{-1} and a surface area of 278.318 m^2g^{-1} in Figure 3-28. I found that the functional groups were not locally formed, but rather distributed uniformly on the graphite nanoplatelet surface from EDS mapping and FE-SEM in line-scan mode (Figure 3-29). Furthermore, the functional groups were distributed evenly inside the sample, as shown in Figure 3-30.

The applicability of the functionalized graphite nanoplatelet as a cathode for NIB was examined in a half-cell within a voltage window of 1.0 V and 4.3 V at a current rate of 0.1 A g^{-1}. Figure 3-31 clearly shows the electrochemical activity of the graphite nanoplatelet with Na in the cathode potential. While the graphite or graphene is generally considered as an anode material due to its low potential, the functionalized graphite nanoplatelet exhibited a considerably higher operating voltage in the Na cell. The average voltage of the graphite nanoplatelet could reach 2.2 V (*vs.* Na) without an apparent voltage plateau. The first discharge capacity was about 190 mAh g^{-1} and increased to ~230 mAh g^{-1} after the first cycle, whose origin will be discussed later.

To illucidate the electrochemical acitivty of functionalized graphite

nanoplatelets with Na, *ex-situ* XPS analysis was performed. Figure 3-32 shows that after the initial discharge, a new peak at 1072.3 eV was detected in the Na 1s region, which reversibly disappeared upon recharge. Since the characteristic binding energy of Na 1s from Na-O is typically found at ~1072 eV, it suggests that a reversible Na incorporation occurs *via* Na-O binding.[7-8] Furthermore, the Na Auger peak was observed at 536.9 eV in O 1s of Figure 3-32b, which confirms the uptake of Na into the functionalized graphite nanoplatelet.[7] Closer examination of O 1s spectrum revealed that the binding nature of oxygen and carbon reversibly changed upon Na insertion and extraction. The intensity of the XPS peak from C=O at 533.5 eV decreased, while that from C-O increased significantly during discharge.[4] This proposes that the Na ions were chemically bound to C=O functional groups by breaking the double bonds and forming single bonds between carbon and oxygen. After charging the sample, the XPS peaks returned to their original state, which illustrates that the Na ion storage in C=O functional groups was reversible. To further confirm the role of functional groups on the electrochemical performance, the graphite nanoplatelet cathode after having fully removed functional groups at a high temperature was tested under the same electrochemical conditions. The pore volume, morphology, and the surface area did not change after being subjected to the 800˚C annealing process (Figure 3-33). Figure 3-34 shows that the absence of functional groups in the sample significantly reduced the specific capacity. Only negligible capacity was observed for the graphite nanoplatelet with few functional groups at the voltage region between 1.0 V and 4.3 V. It implies

that the degree of functionality in graphite nanoplatelets was important for the activation of the electrochemical reaction within the cathode voltage region.

As noted above, the discharge capacity increased after the first cycle (Figure 3-31). To better understand this behavior, the functionalized graphite nanoplatelet cathode was first charged without the initial discharge process in the Na half-cell (Figure 3-35a). Interestingly, a considerably large capacity of ~80 mAh g^{-1} could be charged even without Na insertion to the electrode. We found that this extra capacity accompanied the adsorption of boron on the surface of the graphite nanoplatelet from the *ex situ* XPS analysis in Figure 3-35b. It strongly suggests the contribution of anion adsorption (such as BF_4^-) on the nanoplatelet surface to the capacity. This capacitor-like behavior was reminiscent of the anion participation in supercapacitors, where anions can be reversibly adsorbed on and desorbed from various carbonaceous materials at the high potential.[9] In this respect, the energy storage mechanism of the functionalized graphite nanoplatelet as a NIB cathode is proposed as in Figure 3-36: (i) Na ions bind to the functional groups by breaking double bonds and forming single bonds between carbon and oxygen in the first discharge. (ii) During the initial charging process (<3.8 V *vs.* Na), Na ions are removed from the functionalized graphite nanoplatelet by reversible changes of the single to double C-O bonds. (iii) Further charging processes involve BF_4^- anions adsorbing on the nanoplatelet surface, delivering additional capacity (> 3.8V *vs.* Na). During the subsequent cycles, the combined energy storage reactions continue

reversibly. I found that these series of reactions are so reversible that nearly no capacity decay was observed over cycles in Figure 3-37.

To further explore the participation of anions in the electrochemical reaction, the performance of functionalized graphite nanoplatelet cathodes was tested in Na half-cells with different Na salts in the electrolyte. Figure 3-38a compares the charge/discharge profiles of Na cells using $NaBF_4$ and $NaClO_4$ at a current rate of 1.0 A g^{-1}. While the electrochemical profiles were similar for both cases, significant capacity decay after 300 cycles was observed for the Na cell using $NaClO_4$ (Figure 3-38b). It was found that the capacity decay of the Na cell using $NaClO_4$ accompanied a significant increase in the charge transfer resistance upon repeated battery cycling from EIS analysis, which contrasted to the case of $NaBF_4$ (Figure 3-39). The increase in the resistance was attributed to the gradual formation of an insulating layer on the graphite nanoplatelet with cycling, which is speculated to stem from the electrolyte instability of $NaClO_4$ in PC with high-voltage cycling (above 4 V *vs.* Na).[10] The notable difference in cyclability suggests that the selection of Na electrolytes can be an important factor in utilizing the electrochemical reaction of the functionalized graphite nanoplatelet cathode in NIBs. Nevertheless, it is worth to note that an excellent cycle stability over 300 cycles could be achieved for the functionalized graphite when $NaBF_4$ was used as the Na salt. It is believed that this notable cycle stability originates from the robustness of the chemical and morphological structures of functionalized graphite without involving intercalation of Na ions during battery cycling. Figure 3-40 shows that no significant changes in chemical

and morphological structures are detected after the extended battery cycling. The energy density of the functionalized graphite nanoplatelet cathode could reach 500 Wh kg^{-1} based on the average voltage of 2.2 V (*vs.* Na) and the specific capacity of ~230 mAh g^{-1} (Figure 3-41). Previously reported cathodes for NIB, such as $Na_3V_2(PO_4)_3$, $NaCrO_2$, or $NaCoO_2$, ranged between 300–400 Wh kg^{-1}, whereas few cathode materials, such as bipolar porous organic electrode (BPOE), approach 500 Wh kg^{-1}.[11-20] The functionalized graphite nanoplatelet could deliver exceptionally high power capabilities, and could outperform the high-energy BPOE cathode. The Ragone plot in Figure 3-42 provides the trade-off between energy and power densities of several state-of-the-art NIB cathodes.[11, 21-27] It shows that functionalized graphite can retain an energy of ~100 Wh kg^{-1} with a 10-s charge/discharge rate, which exceeds the recently reported high-power NIB cathodes, such as $Na_3V_2(PO_4)_3$ and $Na_{1.72}MnFe(CN)_6$ (NMHFC). We believe that this unprecedently high power capability in NIB can be attributed to the aforementioned fast surface reactions of Na ion and anion without involving the intercalation and the unique interconnected porous morphology of the functionalized graphite that enabled the facile ionic transport in the battery.

3.2.4 Conclusion

Porous functionalized graphite nanoplatelets were proposed as a novel high-performance cathode for NIBs. The porous functionalized graphite nanoplatelet exhibited a specific capacity of ~230 mAh g^{-1}, delivering a high energy of ~500 Wh kg^{-1} *via* fast surface Faradaic reaction combined with the capacitive anion adsorption. The high energy could be retained even with 10-s charge/discharge rates, which could lead to the development of high-power NIB. The promising electrochemical performance of the functionalized graphite nanoplatelet cathode was attributed to the following aspects: (i) the light carbonaceous framework in the absence of heavy transition metals, (ii) fast surface reactions rather than intercalation-based Na storage reactions, (iii) the interconnected porous morphology enabling facile and rapid Na ion transport, and (iv) rapid electron transport through the carbonaceous framework.[6] This development of a novel class of cathode materials provides new possibilities for the design of high-performance NIBs based on graphites.

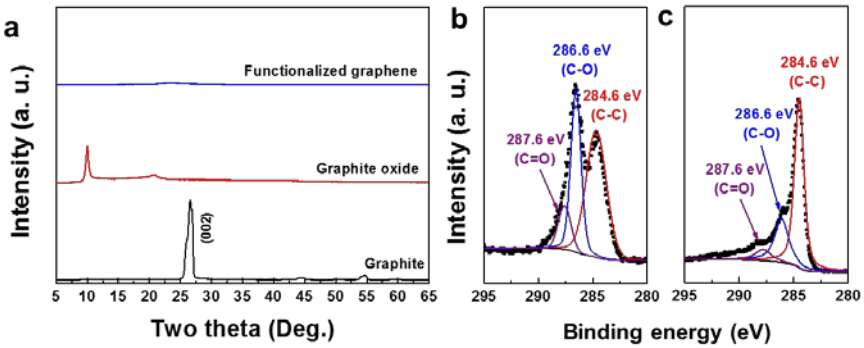

Figure 3-24. Fabrication of functionalized graphite nanoplatelets with porous structures. (a) XRD patterns of graphite oxide and functionalized graphite nanoplatelets with a graphite reference. XPS analysis results of **(b)** graphite oxide and **(c)** functionalized graphite nanoplatelets.

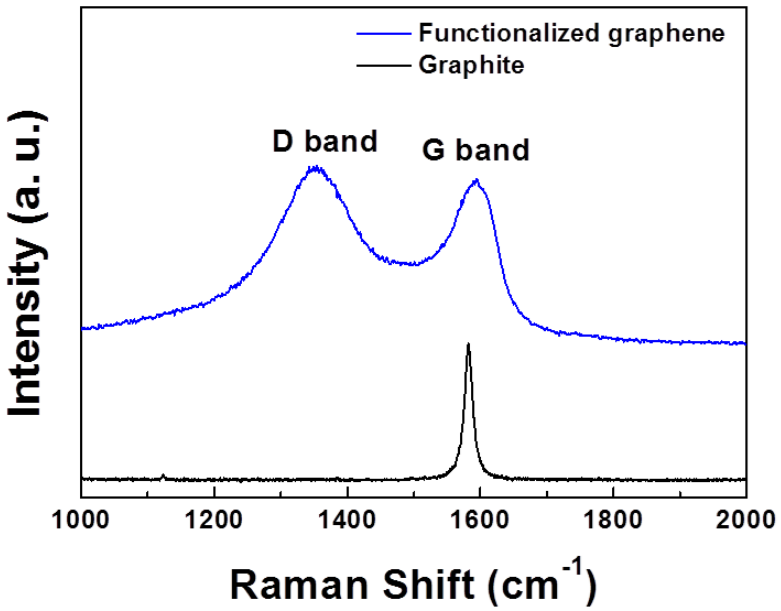

Figure 3-25. Raman analysis of functionalized graphite nanoplatelets with a graphite reference.

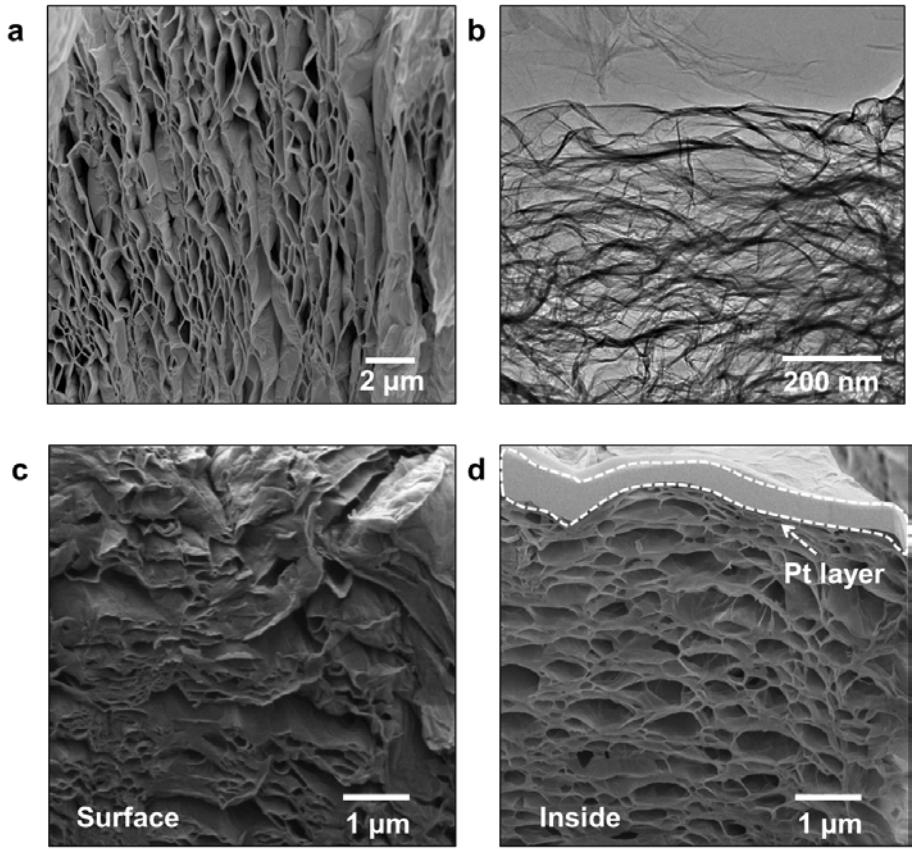

Figure 3-26. (a) FE-SEM image and **(b)** HR-TEM image of functionalized graphite nanoplatelets. FE-SEM images of functionalized graphite nanoplatelets **(c)** at the surface and **(d)** inside after FIB cutting revealed that the pores were interconnected from the surface to the inside of functionalized graphite nanoplatelets. To prevent damage from FIB cutting, Pt was deposited on the surface of the graphite nanoplatelets.

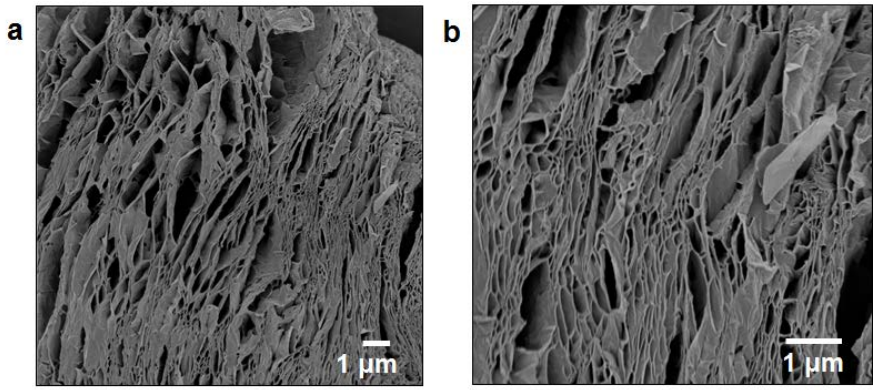

Figure 3-27. FE-SEM images of several cross-sectioned regions of functionalized graphite nanoplatelets showing that the pores are also present inside the sample.

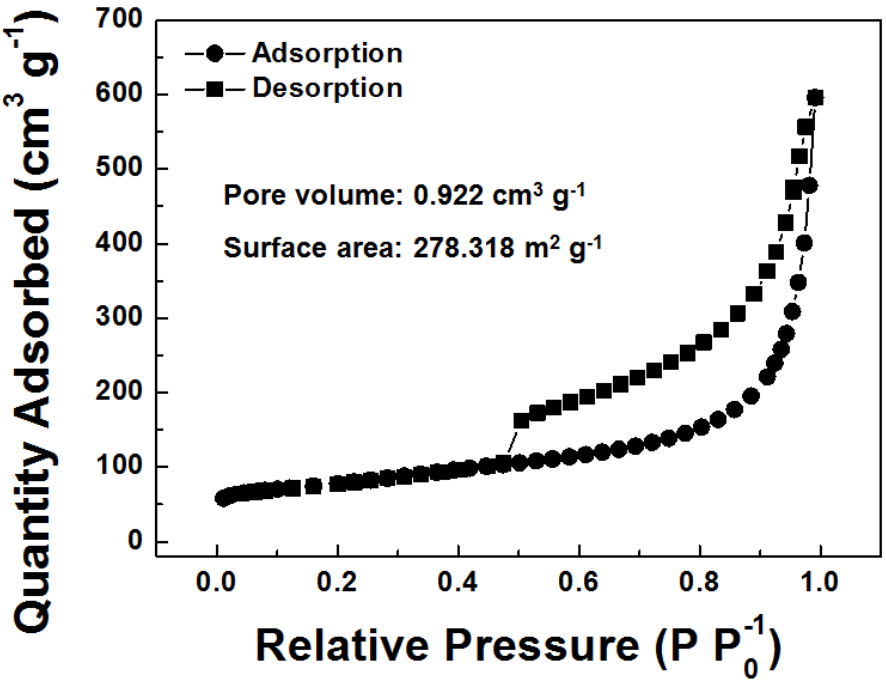

Figure 3-28. N_2 adsorption/desorption isotherm plot of functionalized graphite nanoplatelets. The hysteresis between adsorption and desorption curves revealed mesopores.

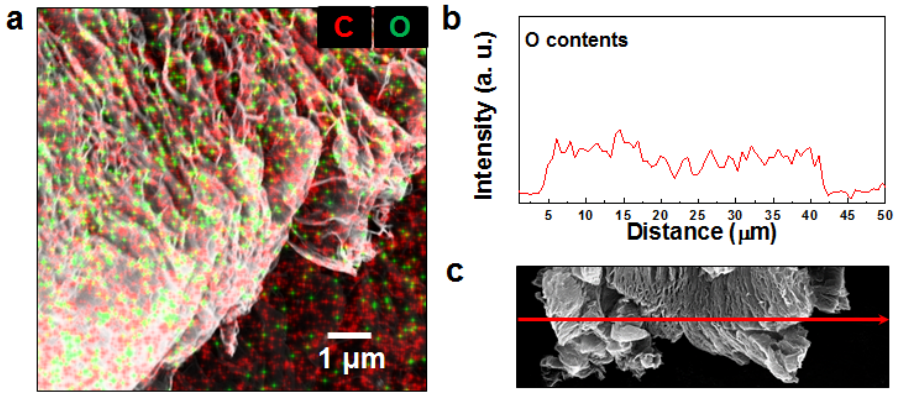

Figure 3-29. Macroscopic distribution of functional groups in the sample. **(a)** FE-SEM image merged with EDS mapping, **(b)** EDS line scan and **(c)** the corresponding FE-SEM image showing that the functional groups were distributed uniformly on the graphite nanoplatelet surface.

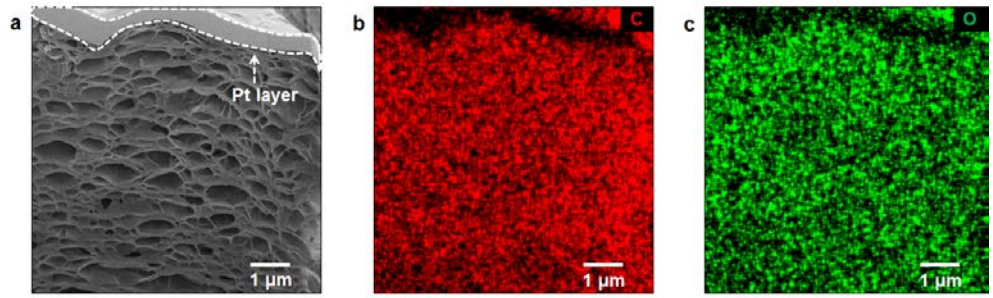

Figure 3-30. FE-SEM images with EDS mapping analysis. (a) FE-SEM image after FIB cutting. To prevent damage from FIB cutting, the Pt layer was deposited on the surface of the sample. EDS mapping image of **(b)** carbon and **(c)** oxygen, which showed that functional groups were distributed uniformly, even inside the sample.

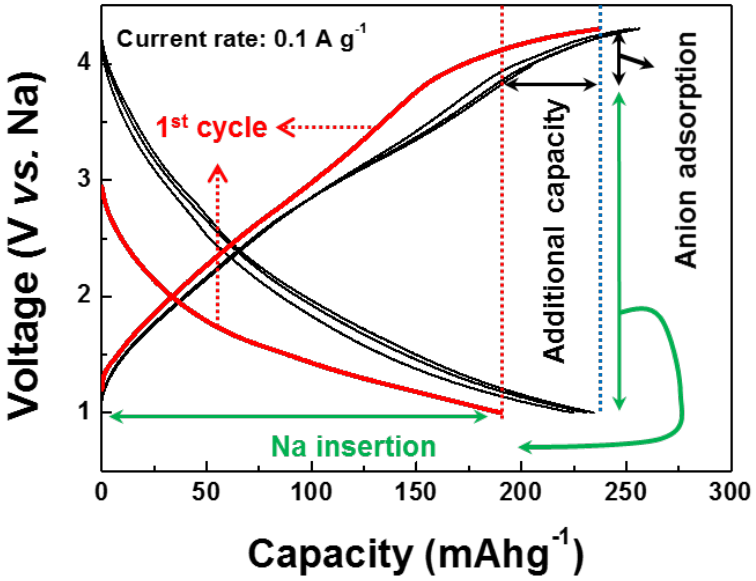

Figure 3-31. Energy storage capability and reaction mechanism. Charge/discharge profiles of functionalized graphite nanoplatelet cathodes during the initial cycles.

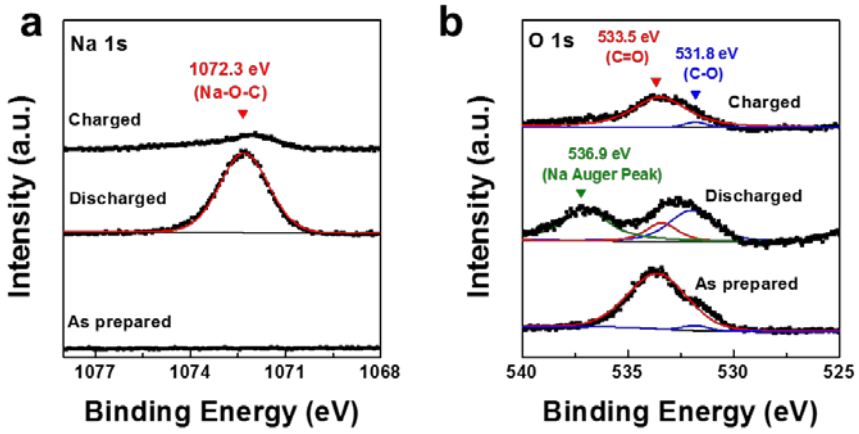

Figure 3-32. ***Ex-situ*** **XPS analyses for Na storage mechanism.** The Na ion storage mechanism was confirmed by *ex situ* XPS analysis at the **(a)** Na 1s and **(b)** O 1s region.

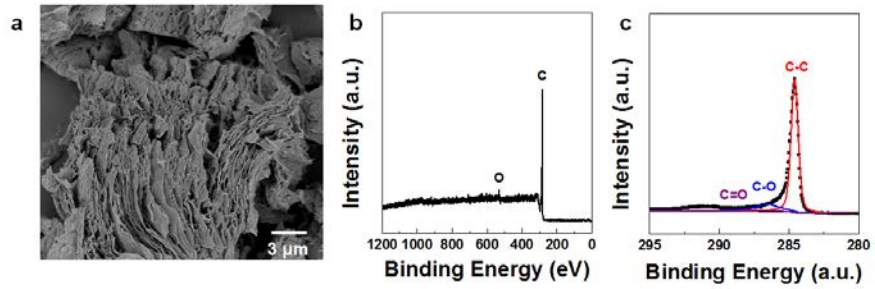

Figure 3-33. Material characterization of reduced graphite nanoplatelets. **(a)** FE-SEM image of reduced graphite nanoplatelets. The porous structure was maintained after the high-temperature annealing process. **(b)** XPS full scan and **(c)** XPS spectrum in C1s region reveals that the functional groups were completely removed at a high temperature annealing process. The BET surface area and pore volume were 234.1051 m^2g^{-1} and 0.837639 cm^3g^{-1}, respectively.

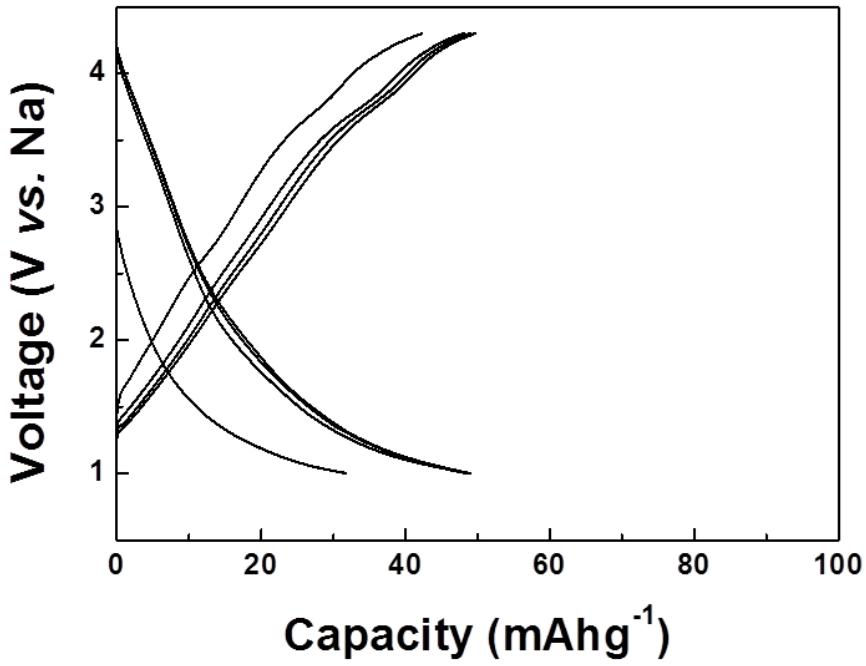

Figure 3-34. The electrochemical profile of graphite nanoplatelets with few functional groups in the voltage range from 1.0 V to 4.3 V at a current rate of 0.1 A g^{-1}.

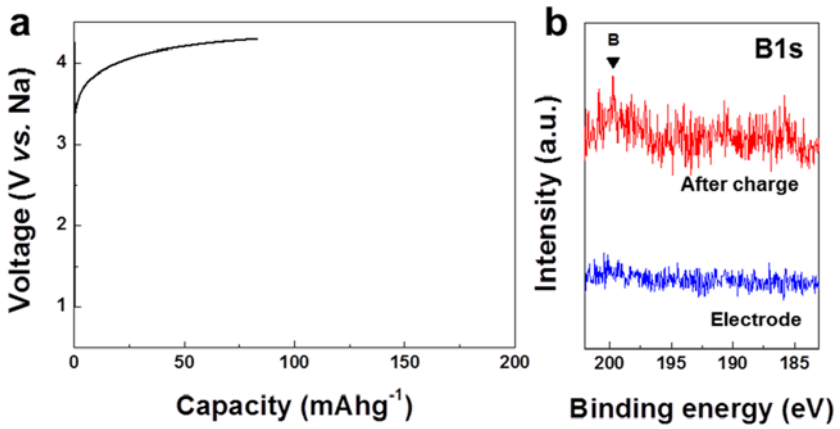

Figure 3-35. Anion adsorption on functionalized graphite nanoplatelet cathode. (a) The electrochemical profile when the functionalized graphite nanoplatelet cathode was first charged. **(b)** XPS analysis results when functionalized graphite nanoplatelet cathodes were first charged. When a functionalized graphite nanoplatelet cathode was charged to high voltage, BF_4^- anion could be adsorbed on its surface, delivering a specific capacity of ~80 mAh g^{-1} at a low current rate of 0.05 A g^{-1}.

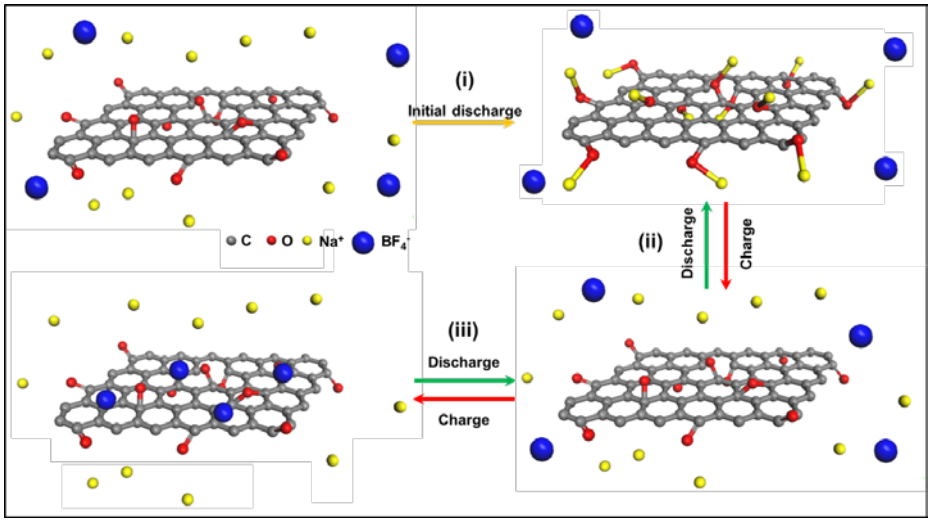

Figure 3-36. Schematic illustration of the energy storage mechanism of functionalized graphite nanoplatelet cathodes.

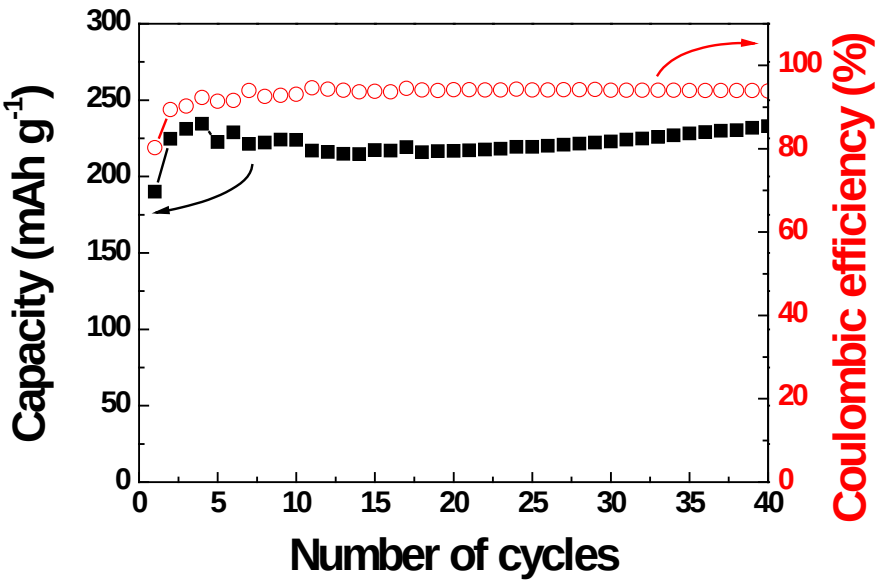

Figure 3-37. Cyclability of functionalized graphite nanoplatelets upon 40 cycles. The electrochemical cells were tested at a current rate of 0.1 A g^{-1} in the voltage window between 1.0 V and 4.3 V using the electrolyte $NaBF_4$.

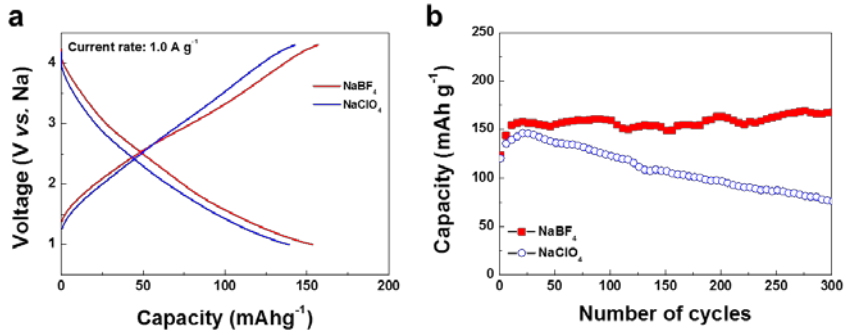

Figure 3-38. Electrochemical performance of functionalized graphite nanoplatelet cathode. (a) Charge/discharge profiles in the 20th cycle and **(b)** cyclability of functionalized graphite nanoplatelet cathode at a current rate of 1.0 A g^{-1} with $NaBF_4$ and $NaClO_4$.

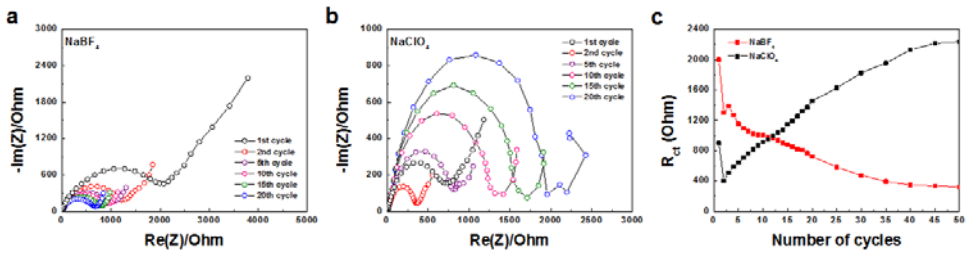

Figure 3-39. Electrochemical impedance spectroscopy (EIS) spectra of functionalized graphite nanoplatelets when **(a)** $NaBF_4$ and **(b)** $NaClO_4$ were used as Na salts in the voltage range from 4.3 V to 1.0 V at a current rate of 1.0 A g^{-1}. The EIS spectra were recorded at the end of charge of each cycle. Representative EIS spectra at the 1^{st}, 2^{nd}, 5^{th}, 10^{th}, 15^{th}, and 20^{th} cycles are shown in Figure 3-39a and 2-39b. Figure 3-39c shows the charge transfer resistance (R_{ct}) in each cycle. The R_{ct} values were obtained by the one-circle fitting of the EIS data using the equivalent circuit by EC-Lab software.

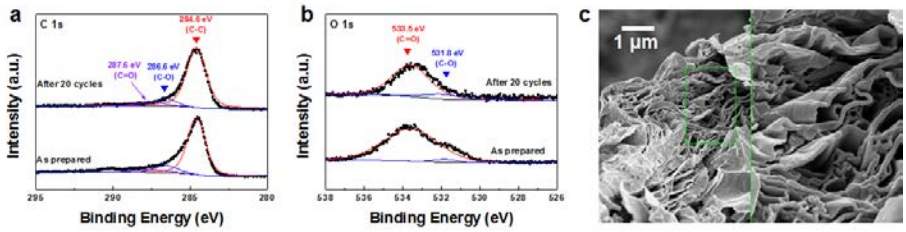

Figure 3-40. Chemical and morphological stability upon battery cycling. *Ex situ* XPS analysis results of functionalized graphite nanoplatelet cathodes before battery cycling and after 20 cycles in **(a)** the C1s region, and **(b)** the O1S region. **(c)** *Ex situ* FE-SEM image after 20 cycles. For *ex situ* analysis, functionalized graphite nanoplatelet cathodes were cycled at a current rate of 0.1 A g^{-1} in the voltage range from 1.0 V to 4.3 V.

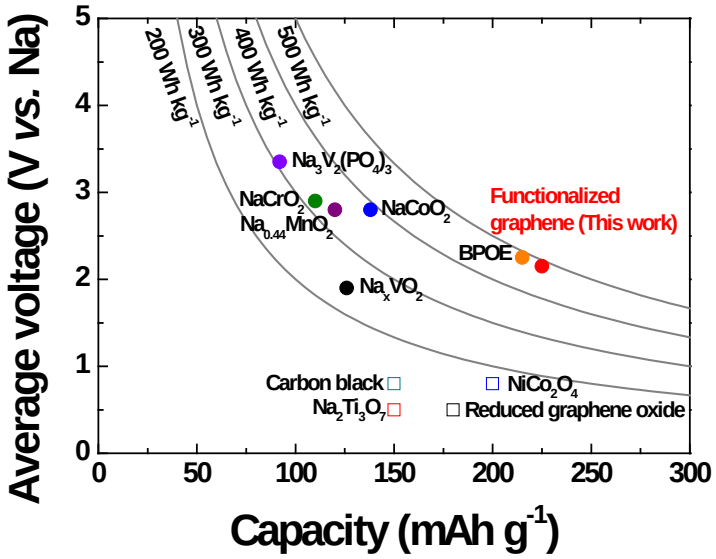

Figure 3-41. Energy density of various cathode materials for NIB. The average operation voltage (*vs.* Na) was used to calculate the energy density for cathodes.

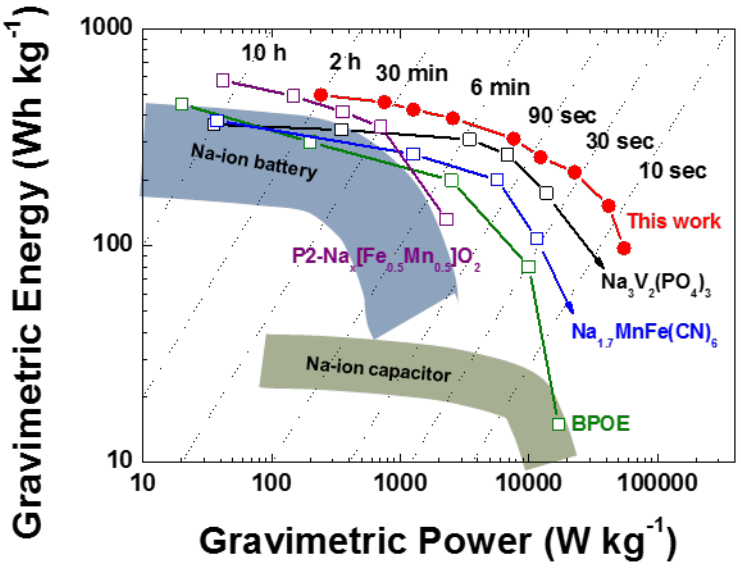

Figure 3-42. Ragone plot of functionalized graphite nanoplatelet cathodes compared to other cathode materials for NIB and Na-ion capacitors. The Ragone plot of the functionalized graphite cathode was calculated from the discharge profiles at various current rates (Figure 3-43).

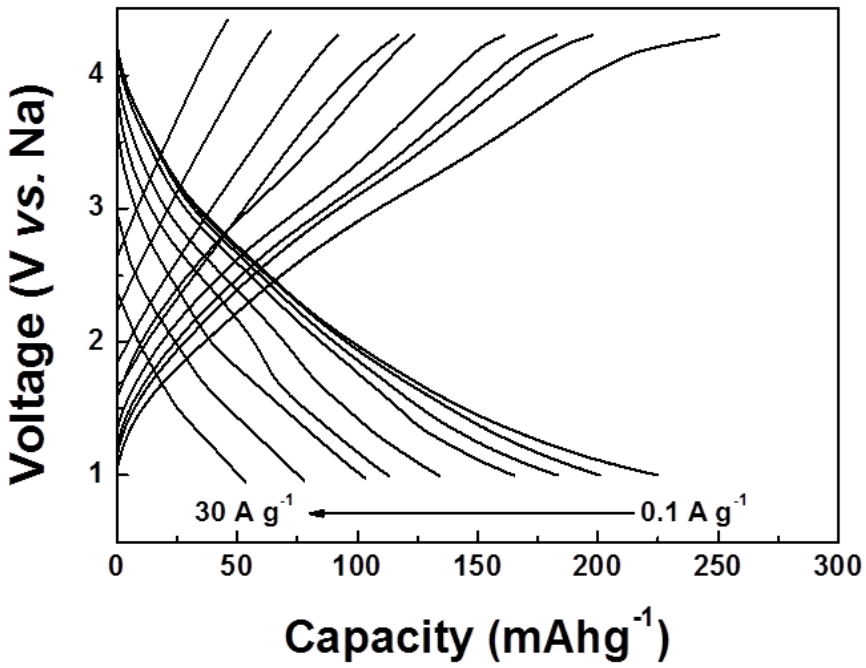

Figure 3-43. Charge/discharge profiles at various current rates from 0.1 A g^{-1} to 30 A g^{-1}. The cut-off voltages were 1.0 V and 4.3 V.

3.2.5 References

1. Hummers, W. S.; Offeman, R. E. Preparation of Graphitic Oxide. *J. Am. Chem. Soc.* **1958,** *80*, 1339-1339.

2. Shin, H.-J.; Kim, K. K.; Benayad, A.; Yoon, S.-M.; Park, H. K.; Jung, I.-S.; Jin, M. H.; Jeong, H.-K.; Kim, J. M.; Choi, J.-Y., et al. Efficient Reduction of Graphite Oxide by Sodium Borohydride and Its Effect on Electrical Conductance. *Adv. Funct. Mater.* **2009,** *19*, 1987-1992.

3. McAllister, M. J.; Li, J.-L.; Adamson, D. H.; Schniepp, H. C.; Abdala, A. A.; Liu, J.; Herrera-Alonso, M.; Milius, D. L.; Car, R.; Prud'homme, R. K., et al. Single Sheet Functionalized Graphene by Oxidation and Thermal Expansion of Graphite. *Chem. Mater.* **2007,** *19*, 4396-4404.

4. Park, S.; An, J.; Jung, I.; Piner, R. D.; An, S. J.; Li, X.; Velamakanni, A.; Ruoff, R. S. Colloidal Suspensions of Highly Reduced Graphene Oxide in a Wide Variety of Organic Solvents. *Nano Lett.* **2009,** *9*, 1593-1597.

5. Kudin, K. N.; Ozbas, B.; Schniepp, H. C.; Prud'homme, R. K.; Aksay, I. A.; Car, R. Raman Spectra of Graphite Oxide and Functionalized Graphene Sheets. *Nano Lett.* **2007,** *8*, 36-41.

6. Kim, H.; Lim, H.-D.; Kim, S.-W.; Hong, J.; Seo, D.-H.; Kim, D.-c.; Jeon, S.; Park, S.; Kang, K. Scalable Functionalized Graphene Nano-platelets as Tunable Cathodes for High-performance Lithium Rechargeable Batteries. *Sci. Rep.* **2013,** *3*, 1506.

7. Nesbitt, H. W.; Bancroft, G. M.; Henderson, G. S.; Ho, R.; Dalby, K. N.; Huang, Y.; Yan, Z. Bridging, non-bridging and free (O2–) oxygen in

Na2O-SiO2 glasses: An X-ray Photoelectron Spectroscopic (XPS) and Nuclear Magnetic Resonance (NMR) study. *J. Non-Cryst. Solids* **2011,** *357*, 170-180.

8. Seah, D. B. a. M. P. Practical Surface Analysis. *John Wiley & Sons, New York, NY, USA, 2nd edition* **1993**.

9. Wang, Q.; Wen, Z. H.; Li, J. H. A Hybrid Supercapacitor Fabricated with a Carbon Nanotube Cathode and a TiO2–B Nanowire Anode. *Adv. Funct. Mater.* **2006,** *16*, 2141-2146.

10. Jian, Z.; Yu, H.; Zhou, H. Designing High-Capacity Cathode Materials for Sodium-Ion Batteries. *Electrochem. Commun.* **2013,** *In press*, http://dx.doi.org/10.1016/j.elecom.2013.06.017.

11. Sakaushi, K.; Hosono, E.; Nickerl, G.; Gemming, T.; Zhou, H.; Kaskel, S.; Eckert, J. Aromatic porous-honeycomb electrodes for a sodium-organic energy storage device. *Nat. Commun.* **2013,** *4*, 1485.

12. Sauvage, F.; Laffont, L.; Tarascon, J. M.; Baudrin, E. Study of the Insertion/Deinsertion Mechanism of Sodium into Na0.44MnO2. *Inorg. Chem.* **2007,** *46*, 3289-3294.

13. Jian, Z.; Zhao, L.; Pan, H.; Hu, Y.-S.; Li, H.; Chen, W.; Chen, L. Carbon coated Na3V2(PO4)3 as novel electrode material for sodium ion batteries. *Electrochem. Commun.* **2012,** *14*, 86-89.

14. Berthelot, R.; Carlier, D.; Delmas, C. Electrochemical investigation of the P2–NaxCoO2 phase diagram. *Nat. Mater.* **2011,** *10*, 74-80.

15. Komaba, S.; Takei, C.; Nakayama, T.; Ogata, A.; Yabuuchi, N. Electrochemical intercalation activity of layered NaCrO2 vs. LiCrO2.

Electrochem. Commun. **2010,** *12*, 355-358.

16. Guignard, M.; Didier, C.; Darriet, J.; Bordet, P.; Elkaïm, E.; Delmas, C. P2-NaxVO2 system as electrodes for batteries and electron-correlated materials. *Nat. Mater.* **2013,** *12*, 74-80.

17. Wang, Y.-X.; Chou, S.-L.; Liu, H.-K.; Dou, S.-X. Reduced graphene oxide with superior cycling stability and rate capability for sodium storage. *Carbon* **2013,** *57*, 202-208.

18. Alcántara, R.; Jiménez-Mateos, J. M.; Lavela, P.; Tirado, J. L. Carbon black: a promising electrode material for sodium-ion batteries. *Electrochem. Commun.* **2001,** *3*, 639-642.

19. Alcántara, R.; Jaraba, M.; Lavela, P.; Tirado, J. L. NiCo2O4 Spinel: First Report on a Transition Metal Oxide for the Negative Electrode of Sodium-Ion Batteries. *Chem. Mater.* **2002,** *14*, 2847-2848.

20. Rudola, A.; Saravanan, K.; Mason, C. W.; Balaya, P. Na2Ti3O7: an intercalation based anode for sodium-ion battery applications. *J. Mater. Chem. A* **2013,** *1*, 2653-2662.

21. Kim, D.; Kang, S.-H.; Slater, M.; Rood, S.; Vaughey, J. T.; Karan, N.; Balasubramanian, M.; Johnson, C. S. Enabling Sodium Batteries Using Lithium-Substituted Sodium Layered Transition Metal Oxide Cathodes. *Adv. Energy Mater.* **2011,** *1*, 333-336.

22. Oh, S.-M.; Myung, S.-T.; Hassoun, J.; Scrosati, B.; Sun, Y.-K. Reversible NaFePO4 electrode for sodium secondary batteries. *Electrochem. Commun.* **2012,** *22*, 149-152.

23. Kawabe, Y.; Yabuuchi, N.; Kajiyama, M.; Fukuhara, N.; Inamasu,

T.; Okuyama, R.; Nakai, I.; Komaba, S. Synthesis and electrode performance of carbon coated Na2FePO4F for rechargeable Na batteries. *Electrochem. Commun.* **2011,** *13*, 1225-1228.

24. Wang, L.; Lu, Y.; Liu, J.; Xu, M.; Cheng, J.; Zhang, D.; Goodenough, J. B. A Superior Low-Cost Cathode for a Na-Ion Battery. *Angew. Chem. Int. Ed.* **2013,** *52*, 1964-1967.

25. Saravanan, K.; Mason, C. W.; Rudola, A.; Wong, K. H.; Balaya, P. The First Report on Excellent Cycling Stability and Superior Rate Capability of Na3V2(PO4)3 for Sodium Ion Batteries. *Adv. Energy Mater.* **2013,** *3*, 444-450.

26. Chen, Z.; Augustyn, V.; Jia, X.; Xiao, Q.; Dunn, B.; Lu, Y. High-Performance Sodium-Ion Pseudocapacitors Based on Hierarchically Porous Nanowire Composites. *ACS Nano* **2012,** *6*, 4319-4327.

27. Yabuuchi, N.; Kajiyama, M.; Iwatate, J.; Nishikawa, H.; Hitomi, S.; Okuyama, R.; Usui, R.; Yamada, Y.; Komaba, S. P2-type Nax[Fe1/2Mn1/2]O2 made from earth-abundant elements for rechargeable Na batteries. *Nat. Mater.* **2012,** *11*, 512-517.

Chapter 4. All-graphene-battery

4.1 A new type all-graphene-battery

4.1.1 Research background

The global energy paradigm is rapidly transforming from fossil fuels to sustainable energy resources, including solar, wind, and geothermal energies.[1-2] However, power production from those energy resources is not always coincident with energy demand. Therefore, the development of large-scale energy-storage systems that resolve this discrepancy is vitally important. Considerable efforts have been expended on the development of high-performance energy-storage devices such as lithium-ion batteries (LIBs), supercapacitors, and hybrid supercapacitors.[3-15] A major hurdle remains: the development of a novel energy storage system that combines high energy and power density.

LIBs are promising candidates because of their high energy density, which is

attributed to the high operating potential and the large charge-storage capability of conventional LIB electrode materials.[4-5] However, the power density of available LIBs is not suitable for large-scale applications, and the cost is too high. These issues – low power density and high cost – are closely related to the fundamental electrode reaction characteristic of LIBs, which relies on intercalation-based reactions of transition metal oxides accompanied by intrinsically slow solid-state lithium diffusion[16-17] and generally low electronic conductivity.[4, 17] In this respect, there have been intensive researches on hybrid supercapacitors using a lithium intercalation electrode in one electrode and a capacitive electrode in the other electrode to achieve battery-level energy density combined with the power density of supercapacitors.[18-22] However, despite the recent advancement of hybrid supercapacitors, the imbalance in kinetics between two electrodes still remain as a major drawback that should be overcome. It is because the intercalation reaction in one electrode is generally far slower than the surface reaction in the other electrode.

One approach to resolving the aforementioned challenge is to adopt fast surface electrode reactions in both electrodes while maintaining high energy density.[23-26] Recently, we demonstrated that the functionalization of graphene to enable fast surface reaction could lead to exceptionally high Li storage capability.[4] The functional groups on the graphene cathode acted as radical centers to store Li ions at acceptably high potential.[4, 27]

In this study, we expanded the advantages of exploiting fast surface electrode reactions on functionalized graphene cathodes by matching them

with reduced graphene oxide anodes, thereby introducing an advanced asymmetric hybrid supercapacitors. While similar concept was introduced in the literature, they still used lithium particles or foils in the anode side incorporating with graphene.[28] Also, the fabrication of graphene was not mass-scalable. To realize, herein, advanced asymmetric full cells, mass-scalable functionalized graphene and prelithiated reduced graphene oxide are used in cathode and anode, respectively, without utilizing lithium metals. The advanced hybrid supercapacitor delivers exceptionally high power density because both the anode and cathode exhibit fast surface reactions combined with porous morphology and high electrical conductivity. Furthermore, their similar chemistry and microstructure maximizes the performance of each electrode in the full cell without introducing a power imbalance, which is commonly observed in hybrid supercapacitors.[11]

4.1.1.1 References

1. Turner, J. A. A Realizable Renewable Energy Future. *Science* **1999,** *285*, 687-689.

2. Kim, H.; Park, Y.-U.; Park, K.-Y.; Lim, H.-D.; Hong, J.; Kang, K. Novel transition-metal-free cathode for high energy and power sodium rechargeable batteries. *Nano Energy* **2014,** *4*, 97-104.

3. Kang, K.; Meng, Y. S.; Bréger, J.; Grey, C. P.; Ceder, G. Electrodes with High Power and High Capacity for Rechargeable Lithium Batteries. *Science* **2006,** *311*, 977-980.

4. Slater, M. D.; Kim, D.; Lee, E.; Johnson, C. S. Sodium-Ion Batteries. *Adv. Funct. Mater.* **2013,** *23*, 947-958.

5. Armand, M.; Tarascon, J. M. Building better batteries. *Nature* **2008,** *451*, 652-657.

6. Wu, X.-L.; Jiang, L.-Y.; Cao, F.-F.; Guo, Y.-G.; Wan, L.-J. LiFePO4 Nanoparticles Embedded in a Nanoporous Carbon Matrix: Superior Cathode Material for Electrochemical Energy-Storage Devices. *Adv. Mater.* **2009,** *21*, 2710-2714.

7. Shi, Y.; Guo, B.; Corr, S. A.; Shi, Q.; Hu, Y.-S.; Heier, K. R.; Chen, L.; Seshadri, R.; Stucky, G. D. Ordered Mesoporous Metallic MoO2 Materials with Highly Reversible Lithium Storage Capacity. *Nano Lett.* **2009,** *9*, 4215-4220.

8. Hsu, K.-F.; Tsay, S.-Y.; Hwang, B.-J. Synthesis and characterization of nano-sized LiFePO4 cathode materials prepared by a citric acid-based sol-

gel route. *J. Mater. Chem.* **2004,** *14*, 2690-2695.

9. Lee, S. W.; Yabuuchi, N.; Gallant, B. M.; Chen, S.; Kim, B.-S.; Hammond, P. T.; Shao-Horn, Y. High-power lithium batteries from functionalized carbon-nanotube electrodes. *Nat. Nanotechnol.* **2010,** *5*, 531-537.

10. Tarascon, J. M.; Armand, M. Issues and challenges facing rechargeable lithium batteries. *Nature* **2001,** *414*, 359-367.

11. Park, Y.-U.; Seo, D.-H.; Kwon, H.-S.; Kim, B.; Kim, J.; Kim, H.; Kim, I.; Yoo, H.-I.; Kang, K. A New High-Energy Cathode for a Na-Ion Battery with Ultrahigh Stability. *J. Am. Chem. Soc.* **2013,** *135*, 13870-13878.

12. Stoller, M. D.; Park, S.; Zhu, Y.; An, J.; Ruoff, R. S. Graphene-Based Ultracapacitors. *Nano Lett.* **2008,** *8*, 3498-3502.

13. Ye, T.; Barpanda, P.; Nishimura, S.-i.; Furuta, N.; Chung, S.-C.; Yamada, A. General Observation of Fe3+/Fe2+ Redox Couple Close to 4 V in Partially Substituted Li2FeP2O7 Pyrophosphate Solid-Solution Cathodes. *Chem. Mater.* **2013,** *25*, 3623-3629.

14. Kim, H.; Kim, H.; Kim, S.-W.; Park, K.-Y.; Kim, J.; Jeon, S.; Kang, K. Nano-graphite platelet loaded with LiFePO4 nanoparticles used as the cathode in a high performance Li-ion battery. *Carbon* **2012,** *50*, 1966-1971.

15. Choi, B. G.; Yang, M.; Hong, W. H.; Choi, J. W.; Huh, Y. S. 3D Macroporous Graphene Frameworks for Supercapacitors with High Energy and Power Densities. *ACS Nano* **2012,** *6*, 4020-4028.

16. Ellis, B.; Perry, L. K.; Ryan, D. H.; Nazar, L. F. Small Polaron Hopping in LixFePO4 Solid Solutions: Coupled Lithium-Ion and Electron

Mobility. *J. Am. Chem. Soc.* **2006,** *128*, 11416-11422.

17. Gaberscek, M.; Kuzma, M.; Jamnik, J. Electrochemical kinetics of porous, carbon-decorated LiFePO4 cathodes: separation of wiring effects from solid state diffusion. *Phys. Chem. Chem. Phys.* **2007,** *9*, 1815-1820.

18. Simon, P.; Gogotsi, Y.; Dunn, B. Where Do Batteries End and Supercapacitors Begin? *Science* **2014,** *343*, 1210-1211.

19. Kim, J.-H.; Kim, J.-S.; Lim, Y.-G.; Lee, J.-G.; Kim, Y.-J. Effect of carbon types on the electrochemical properties of negative electrodes for Li-ion capacitors. *J. Power Sources* **2011,** *196*, 10490-10495.

20. Sivakkumar, S. R.; Pandolfo, A. G. Evaluation of lithium-ion capacitors assembled with pre-lithiated graphite anode and activated carbon cathode. *Electrochim. Acta* **2012,** *65*, 280-287.

21. Du Pasquier, A.; Plitz, I.; Menocal, S.; Amatucci, G. A comparative study of Li-ion battery, supercapacitor and nonaqueous asymmetric hybrid devices for automotive applications. *J. Power Sources* **2003,** *115*, 171-178.

22. Park, M.-S.; Lim, Y.-G.; Kim, J.-H.; Kim, Y.-J.; Cho, J.; Kim, J.-S. A Novel Lithium-Doping Approach for an Advanced Lithium Ion Capacitor. *Adv. Energy Mater.* **2011,** *1*, 1002-1006.

23. Wang, Z.-L.; Guo, R.; Ding, L.-X.; Tong, Y.-X.; Li, G.-R. Controllable Template-Assisted Electrodeposition of Single- and Multi-Walled Nanotube Arrays for Electrochemical Energy Storage. *Sci. Rep.* **2013,** *3*, 1204.

24. Zhang, G.; Lou, X. W. Controlled Growth of NiCo2O4 Nanorods and Ultrathin Nanosheets on Carbon Nanofibers for High-performance

Supercapacitors. *Sci. Rep.* **2013,** *3*, 1470.

25. An, K. H.; Kim, W. S.; Park, Y. S.; Moon, J. M.; Bae, D. J.; Lim, S. C.; Lee, Y. S.; Lee, Y. H. Electrochemical Properties of High-Power Supercapacitors Using Single-Walled Carbon Nanotube Electrodes. *Adv. Funct. Mater.* **2001,** *11*, 387-392.

26. Winter, M.; Brodd, R. J. What Are Batteries, Fuel Cells, and Supercapacitors? *Chem. Rev.* **2004,** *104*, 4245-4270.

27. Wang, D.-W.; Sun, C.; Zhou, G.; Li, F.; Wen, L.; Donose, B. C.; Lu, G. Q.; Cheng, H.-M.; Gentle, I. R. The examination of graphene oxide for rechargeable lithium storage as a novel cathode material. *J. Mater. Chem. A* **2013,** *1*, 3607-3612.

28. Jang, B. Z.; Liu, C.; Neff, D.; Yu, Z.; Wang, M. C.; Xiong, W.; Zhamu, A. Graphene Surface-Enabled Lithium Ion-Exchanging Cells: Next-Generation High-Power Energy Storage Devices. *Nano Lett.* **2011,** *11*, 3785-3791.

4.1.2 Experiments

$NaNO_3$ (5 g) and H_2SO_4 (225 mL) were added to graphite (5 g) and stirred for 30 min in an ice bath. $KMnO_4$ (25 g) was added to the resulting solution, and then the solution was stirred at 50°C for 2 h. Deionized (DI) water (500 mL) and H_2O_2 (30 mL, 35%) were then slowly added to the solution, and the solution was washed with HCl (750 mL, 10%). Additional washing with concentrated HCl (500 mL, 37%) afforded the GO product as a powder. Next, the GO powder samples were annealed at 120°C for 6 h to synthesize functionalized graphene. The reduced graphene oxide was prepared by high temperature treatment of the functionalized graphene sample at 800°C.

The structure of the samples was analyzed with an X-ray diffactometer (XRD, D2PHASER) using Cu Kα radiation. X-ray photoelectron spectroscopy (XPS, AXIS-HSi) was used to determine the degree of oxidation of the samples. The morphology of the samples was verified using field-emission scanning electron microscopy (FE-SEM, SUPRA 55VP) and high-resolution transmission electron microscopy (HR-TEM, JEM-3000F). Focused ion beam (FIB, AURIGA) analysis was carried out at 30 kV and 600 pA after Pt deposition. The samples were further analyzed using a high-resolution dispersive Raman microscope (LabRAM HR UV/Vis/NIR). The surface area and pore volume were quantified using the Brunauer–Emmett–Teller (BET) method.

Electrodes were prepared by mixing the active material (functionalized graphene or reduced graphene oxide, 70 wt%) with polyvinylidene fluoride

binder (PVDF, 20 wt%) and Super-P® conductive carbon black (10 wt%) in an *N*-methyl-2-pyrrolidone (NMP) solvent. The resulting slurry was uniformly pasted onto Al or Cu foil, dried at 120°C for 2 h, and roll-pressed. Test half-cells were assembled in a glove box into a two-electrode configuration with a Li metal counter electrode, a separator (Celgard 2400), and a 1 M lithium hexafluorophosphate electrolyte in a 1:1 mixture of ethylene carbonate and dimethyl carbonate (Techno Semichem). Electrochemical profiles were obtained over a voltage range from 4.5 to 1.5 V for the functionalized graphene cathode, and over a voltage range from 3.0 to 0.01 V for the reduced graphene oxide anode using a multichannel potentio-galvanostat (WonATech). Before constructing full cells, each electrode was cycled twice as a formation step in half-cells at a current rate of 50 mA g^{-1}, and then the cells were disassembled and re-collected in a full cell. The reduced graphene oxide was fully discharged (lithiated) up to 0.01 V (*vs.* Li) before used in the full cells. The mass balance in the test cells was about 2.5 : 1 (cathode : anode). The mass loading of the electrode including a cathode and an anode was 1.1-1.2 mg. The full cells were assembled in a glove box into a two-electrode configuration with a separator (Celgard 2400), and a 1 M lithium hexafluorophosphate electrolyte in a 1:1 mixture of ethylene carbonate and dimethyl carbonate (Techno Semichem). The fabricated cells were tested in the voltage range from 0.01 to 4.3 V.

4.1.3 Results and discussion

Simple chemical modification was used to tune the graphene for either the anode or cathode. Starting from natural graphite, the modified Hummers method was used to obtain both the functionalized graphene cathode and the reduced graphene oxide anode. The characteristic XRD peak of graphite at 26° shifted to a lower angle after oxidation; this shift was attributed to the extended interlayers in graphite oxide (Figure 4-1). XPS analysis revealed that the oxygen content increased from 2.1 to 33% after the oxidation process (Figure 4-2).[1] The resulting graphite oxides were reduced partially or fully to yield cathode graphene (functionalized graphene) or anode graphene (reduced graphene oxide), respectively. In our previous work, we demonstrated that porous functionalized graphene can be obtained in a one-step annealing process at low temperature (120°C) in a controlled atmosphere.[2] The reduction at low temperature was verified by XRD and XPS analyses, as shown in Figure 4-1. No significant XRD peaks were detected after the reduction process, thus indicating the loss of long-range ordering of the graphene planes.[3] In addition, the XPS spectra (Figure 4-1bc) indicated that functional groups, such as C–O and C=O, were reduced either partially (upper spectrum) or almost fully (lower spectrum) compared to graphite oxide (Figure 4-2 and 4-3). The oxygen contents in each sample were approximately 24.5% and 5.8%, respectively. Raman spectroscopy in Figure 4-4 also showed that the D band (a disordered band caused by the graphite edges) and G band (associated with in-plane vibration of the

graphite lattice) were observed at 1350 cm^{-1} and 1590 cm^{-1} in both the functionalized and reduced graphene oxide samples. [4-5] However, the intensity ratios of the D and G bands (D/G) were 1.11 and 1.04 in the functionalized and reduced graphene oxide samples, respectively, thereby confirming a difference between the two materials.[6] The partially reduced graphene oxide with some remaining functional groups functioned as a cathode, while the reduced graphene oxide with a minimal amount of functional groups functioned as an anode in the cell.

Both materials exhibited a similar porous morphology, as indicated by FE-SEM and HR-TEM analyses (Figure 4-5 and 4-6). The pores in the functionalized graphene were formed by rapid gas evolution under the high vapor pressure generated upon treatment with the concentrated HCl (37 wt%) (Figure 4-5).[2] The reduced graphene oxide with minimal functional groups exhibited a similar microstructure, as illustrated in Figure 4-6. Because the pores were formed by gas evolution, the pores were interconnected and extended from the inside to the surface of the materials, which will be discussed later. The porous electrode structures are expected to be advantageous for electrochemical reactions, because they enable greater penetration of the electrolyte into the interior of the electroactive materials. Moreover, the identical porous structures of both electrodes are expected to be capable of minimizing the power imbalance between the anode and cathode that is a commonly observed drawback of high-power hybrid supercapacitors.[7] The surface area and pore volume of the samples were further characterized by BET and N_2 adsorption/desorption isotherm

analyses (Table 4-1, Figure 4-7 and 4-8); the results of both analyses gave similar values for both materials. The slightly lower results observed for the fully reduced graphene originated from partial restacking of graphene layers and locally blocked pores.[8]

EDS line scanning and mapping analyses were carried out to evaluate the spatial distribution of functional groups on the samples (Figure 4-9, 4-11, 4-12). The graphene surface of the cathode was extensively functionalized (Figure 4-9), while far less functionalization was observed on the reduced graphene oxide anode (Figure 4-10). Mapping images from both HR-TEM and FE-SEM (Figure 4-11, 4-12) further indicated that the functional groups were uniformly distributed on the graphene surface. Uniform distribution of functional groups is critical to delivering a large Li capacity because the entire surface of the functionalized graphene cathode can participate in the electrochemical reaction. Cross-sectional images of the functionalized graphene cathode indicated well-developed interconnection of pores within the sample (Figure 4-13) and verified that the functional groups were uniformly distributed even inside the material (Figure 4-14).

Prior to construction of full cells with the functionalized graphene cathode and reduced graphene oxide anode, the electrochemical performances of each electrode were separately characterized in Li half-cell configurations. First, the functionalized graphene cathode was tested in the voltage window between 1.5 and 4.5 V at a current rate of 0.1 A g^{-1} (Figure 4-15). Within this voltage range, the cathode initially delivered approximately 150 mAh g^{-1} at an average discharge voltage of 2.5 V. The capacity increased slightly to

~200 mAh g^{-1} over 100 cycles, likely because of the gradual activation of functional groups within the electrode.[9] *Ex situ* XPS analysis indicated that the C=O functional group was responsible for Li storage at high potential. As shown in Figure 4-16, in the discharged state, the XPS peak corresponding to Li–O–C was emerging. In addition, the intensity of the peak associated with C=O decreased simultaneously with an increase in the peak associated with C–O. This behavior indicated that, in this voltage range, the C=O functional group acted as a redox center for storage of Li ions. Upon repeated cycles, the high specific capacity was maintained with a coulombic efficiency of ~93%. This outstanding cyclability was attributed to C=O/C–O faradaic surface reactions, which resemble pseudocapacitance that does not accompany a significant lattice expansion or contraction. The rate capability test (Figure 4-15b) indicated remarkably fast Li storage capability in the functionalized graphene cathode. A capacity of greater than 100 mAh g^{-1} was delivered at current density of 3,000 mA g^{-1}; furthermore, even at a current density of 8,000 mA g^{-1}, 47% of the initial capacity (~70 mAh g^{-1}) was maintained.

The reduced graphene oxide anode was evaluated in the voltage range from 0.01 to 3.0 V at a current density of 0.1 A g^{-1} (Figure 4-17). A capacity of 540 mAh g^{-1} was reversibly obtained over 100 cycles, while the first irreversible capacity was relatively high. Wang *et al.* reported that Li ions can be stored on both sides of graphene, forming C_3Li.[10] Accordingly, graphene can deliver about twice the capacity of a conventional graphite anode. In our case, >72% of the theoretical capacity was achieved with a

coulombic efficiency near 100% after 100 cycles. Because the reduced graphene oxide fabricated in this study was multilayer rather than single-layer graphene, it delivered slightly lower capacity than the theoretical value. The reduced graphene oxide anode also exhibited outstanding rate capability. At 8,000 mA g^{-1}, 220 mAh g^{-1} of the capacity was delivered without any noticeable capacity degradation (Figure 4-17b). The high-power capability of both electrodes was attributed to the fast surface reactions on the graphene that enabled rapid Li storage capability. The linear relationship between current peaks and scan rates measured by cyclic voltammetry (CV), as shown in Figure 4-18, confirmed that the electrochemical reactions in the functionalized graphene cathode and reduced graphene oxide anode were not diffusion-limited but confined to the surface.[11]

The similar chemical composition and microstructure of both electrodes in the advanced hybrid supercapacitor maximized the performance of each electrode while avoiding the commonly observed power imbalance in the full cell. The advanced hybrid supercapacitor was prepared by combining a functionalized graphene cathode with a reduced graphene oxide anode in a lithiated state, as shown in Figure 4-19. The electrochemical properties of the advanced hybrid supercapacitor were evaluated at a current density of 0.05 A g^{-1} in the voltage window between 0.01 and 4.3 V (Figure 4-20). The specific capacity was approximately 170 mAh g^{-1} based on the weight of the cathode, which corresponded to nearly 100% utilization of the functionalized graphene cathode. The graphene anode delivered a capacity of 430 mAh g^{-1}, which corresponded to ~80% utilization. The total capacity was ~120 mAh

g^{-1} when calculated from the total active material weights of both the cathode and the anode. The charge/discharge profiles were not significantly altered upon repeated cycling, thereby indicating that the electrochemical reaction was highly reversible. High coulombic efficiency (~98%) was achieved after 50 cycles. Extended cycle stability tests were conducted at a current density of 0.5 A g^{-1} (Figure 4-20c). Approximately 75% of the initial capacity was maintained after 400 cycles with a coulombic efficiency of ~99% (Figure 4-20c); approximately 56% of the capacity could be still delivered stably after 2,000 cycles, indicating the robustness of the electrode reaction.

A Ragone plot was used to represent the trade-off between energy and power density from discharge profiles at various current rates, which is important for practical applications. (Figure 4-21). The power (P) and energy (E) were calculated from the equation used in literatures as follows:[7, 12]

$$P = \Delta V \times i/m$$

$$E = P \times t/3600$$

$$\Delta V = (E_{max} + E_{min})/2$$

where, E_{max} and E_{min} are the voltages at the beginning and end of the discharge (V), i is the discharge current (A), t is the discharge time (sec.), and m is the total mass of active materials in the anode and cathode (g).

The advanced hybrid supercapacitor exhibited an energy density of ~225 Wh kg^{-1}. The energy density was comparable to that of conventional LIBs,[13] and it was retained even at second-level charge/discharge rates providing ~ 6,450 W kg^{-1}, which also makes the advanced hybrid supercapacitor comparable to

supercapacitor systems.[14] The power and energy of this advanced hybrid supercapacitor rivaled other high performance hybrid supercapacitors previously reported,[12, 15-17] which have aroused considerable recent interests. The unique performance of the advanced hybrid supercapacitor is attributed to the following factors: (i) the electrochemical reactions in both the anode and cathode are based on fast surface reactions and are similar to those typically associated with supercapacitors, but (ii) the Li storage capability is not compromised due to the large amount of Li storage sites in graphene-derived materials. Additionally, the interconnected porous structure and high electrical conductivity of graphene-based materials boosted the power capability.

4.1.4 Conclusion

An advanced hybrid supercapacitor based on a functionalized graphene cathode combined with a reduced graphene oxide anode was proposed as an alternative high-performance energy storage technology. Simple chemical modification of graphene was used to tune the material for use as either an anode or a cathode. The similar chemical composition and microstructure of the electrodes in the advanced hybrid supercapacitor enabled maximized performance by each electrode and avoided the power imbalance commonly observed in conventional hybrid supercapacitors. As a result, the advanced hybrid supercapacitor delivered a power density of 2,150 W $kg^{-1}_{\text{total electrode}}$ and an energy density of 130 Wh $kg^{-1}_{\text{total electrode}}$, thereby positioning its performance in a region inaccessible to LIBs and supercapacitors. By utilizing carbonaceous materials in both the anode and cathode, this work offers a novel approach to the development of energy-storage devices that bridge the performance gap between LIBs and supercapacitors.

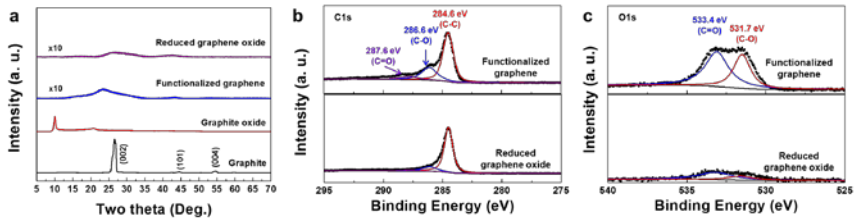

Figure 4-1. Structural and morphological characterization of the functionalized graphene cathode and the reduced graphene oxide anode. **a.** XRD patterns of the functionalized graphene and reduced graphene oxide with comparison to graphite oxide and graphite. XPS analysis of the functionalized graphene and reduced graphene oxide at **b.** the C1s region and **c.** the O1s region. The functionalized graphene contained a large amount of oxygen (24.5%), and the reduced graphene oxide contained a negligible amount of oxygen (5.8%).

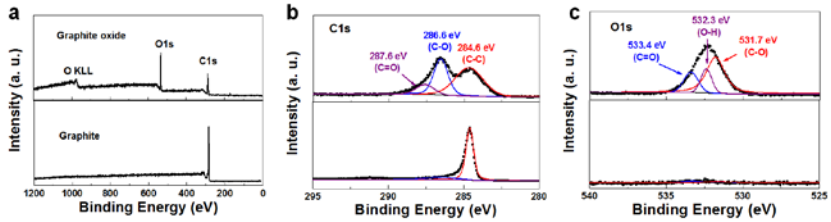

Figure 4-2. XPS analysis of graphite and graphite oxide. **a.** Full scan mode, **b.** C1s region, and **c.** O1s region. The quantitative analysis based the area below each peaks indicates oxygen contents in graphite and graphite oxide are 2.1 % and 33 %, respectively.

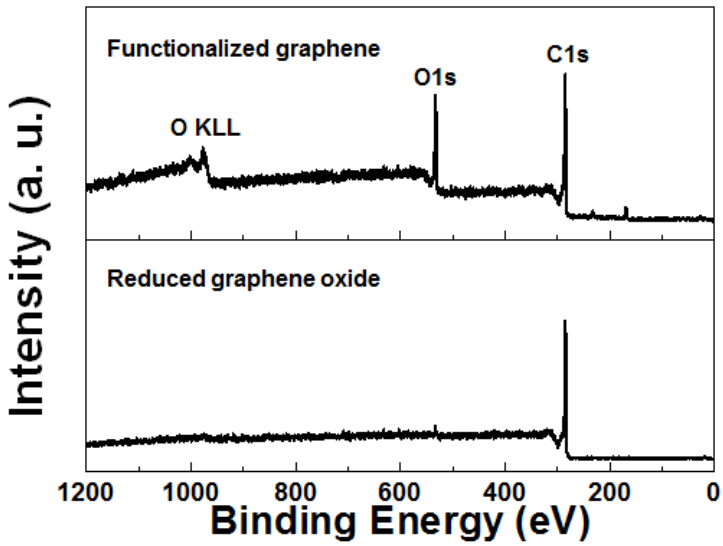

Figure 4-3. XPS analysis of functionalized graphene and reduced graphene oxide at full scan mode.

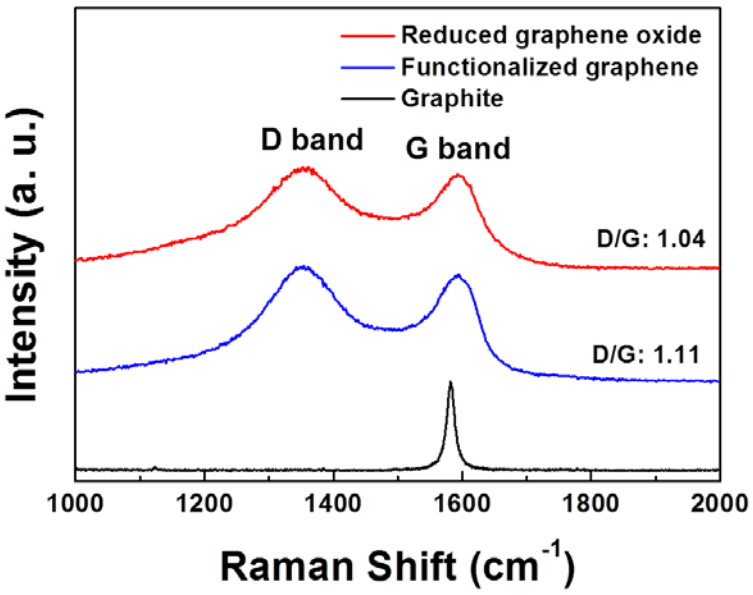

Figure 4-4. Raman analysis of graphite, functionalized graphene, and reduced graphene oxide.

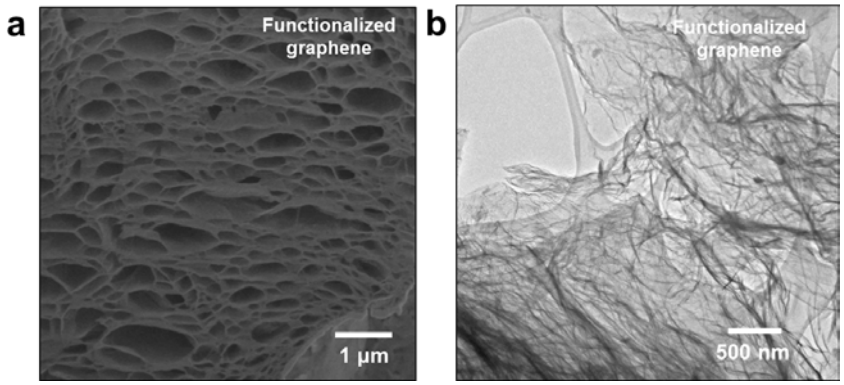

Figure 4-5. Images **a.** and **b.** are FE-SEM and HR-TEM images of the functionalized graphene, respectively.

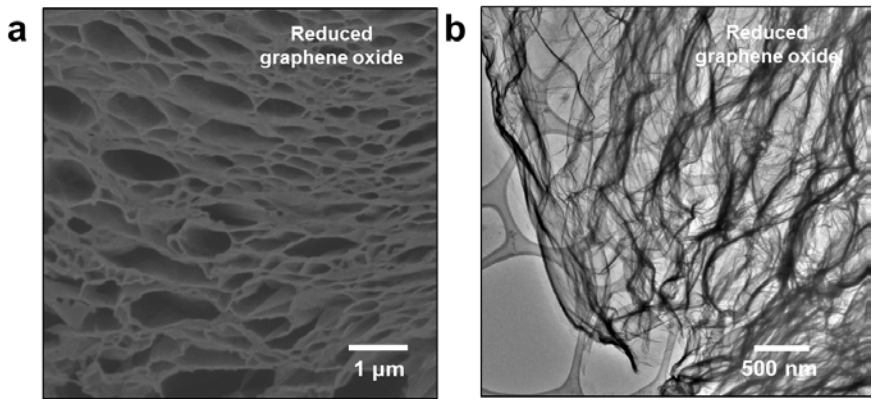

Figure 4-6. Images **a.** and **b.** are FE-SEM and HR-TEM images of the reduced graphene oxide, respectively. The FE-SEM images were obtained by cutting the sample using an FIB.

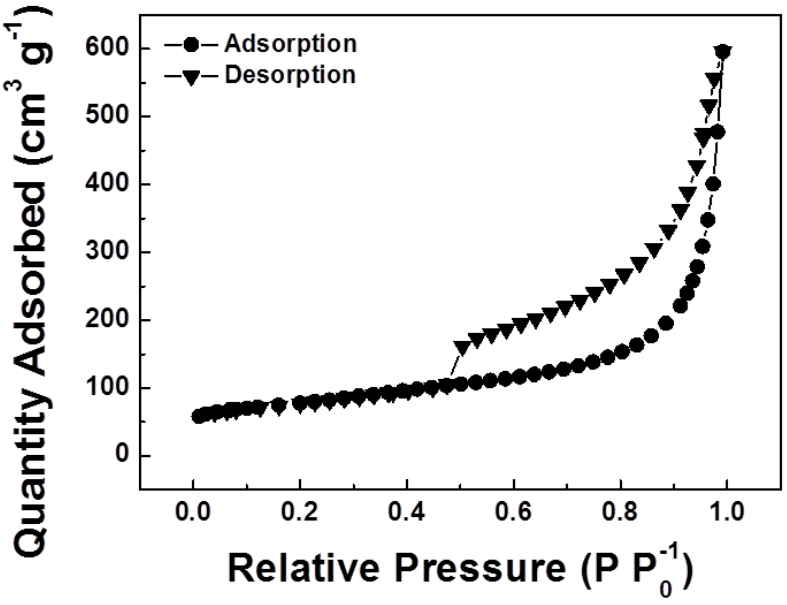

Figure 4-7. The isotherm linear plot of functionalized graphene sample.

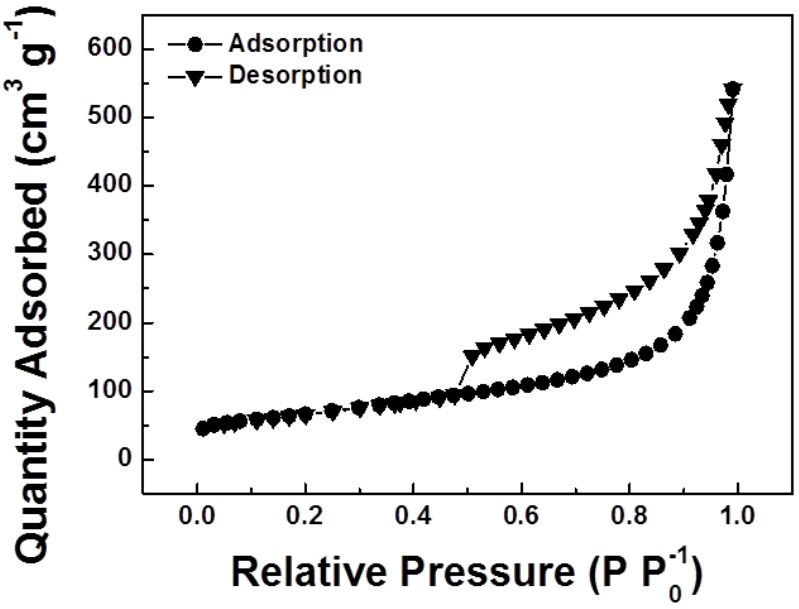

Figure 4-8. The isotherm linear plot of reduced graphene oxide sample.

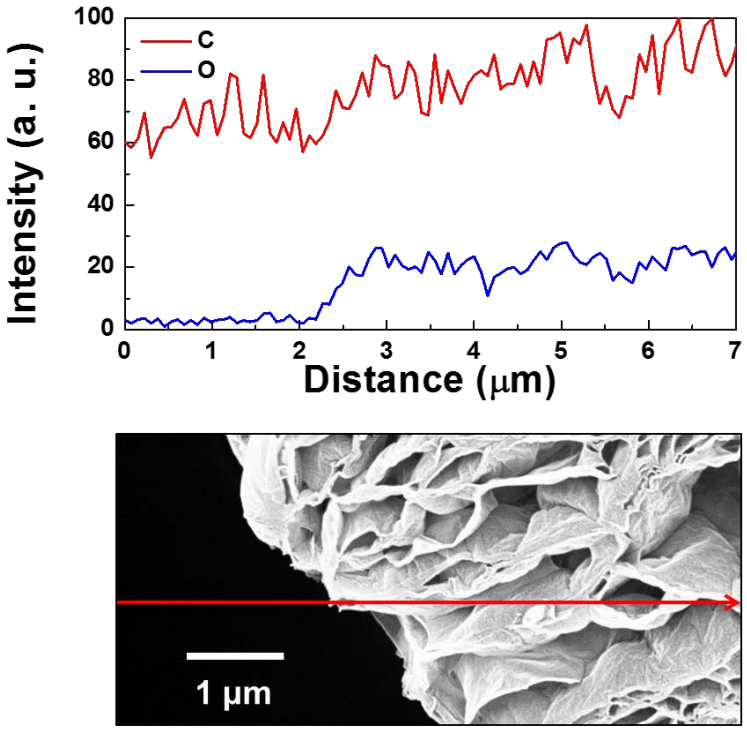

Figure 4-9. Uniformity of functional groups and interconnected pores of the functionalized graphene cathode. a. EDS line-scanning demonstrated that the functional groups were uniformly distributed on the graphene surface.

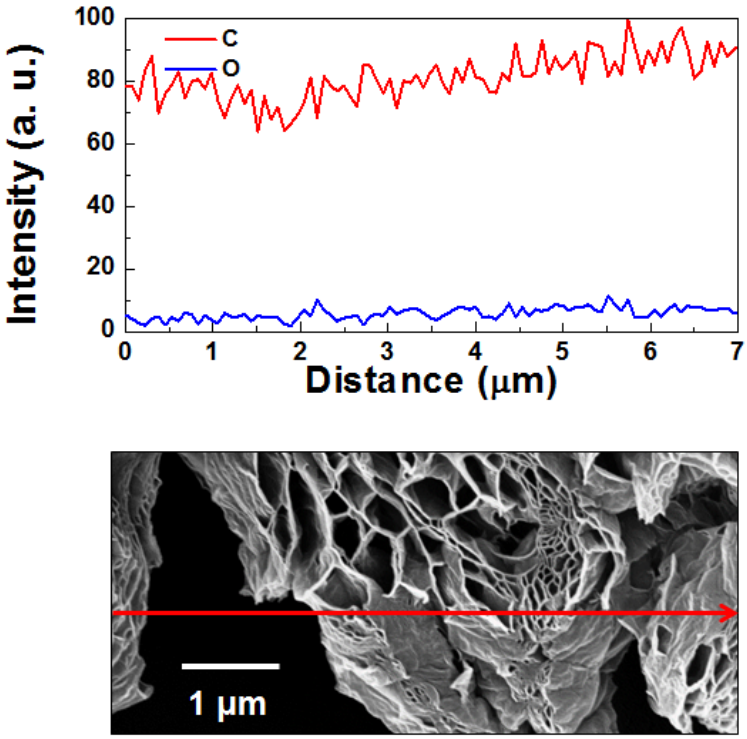

Figure 4-10. EDS line scanning of reduced graphene oxide sample.

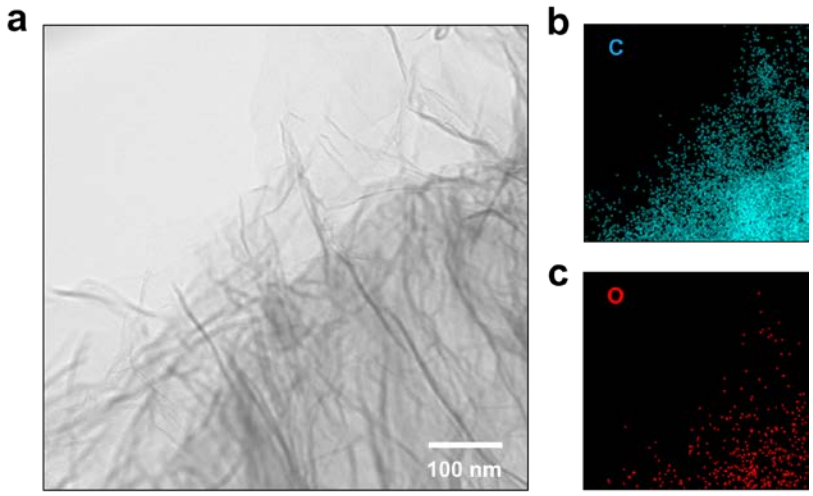

Figure 4-11. a. A TEM image of the functionalized graphene cathode. **b.** and **c.** represent the EDS mapping images of C and O atoms.

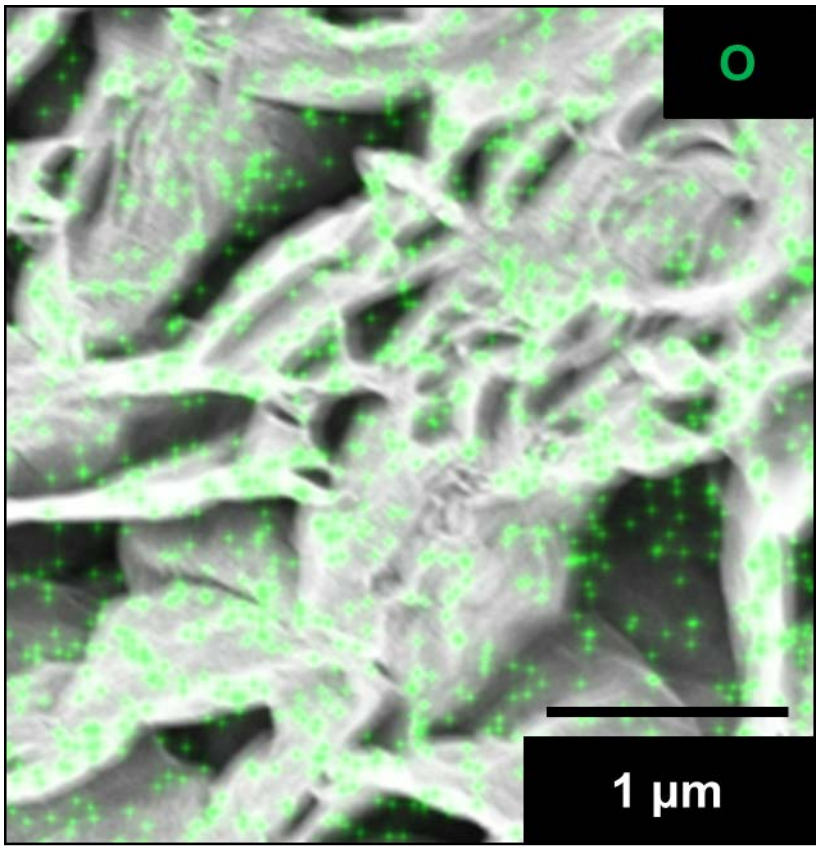

Figure 4-12. FE-SEM image of the functionalized graphene cathode, merging with O atoms acquired by EDS mapping analysis.

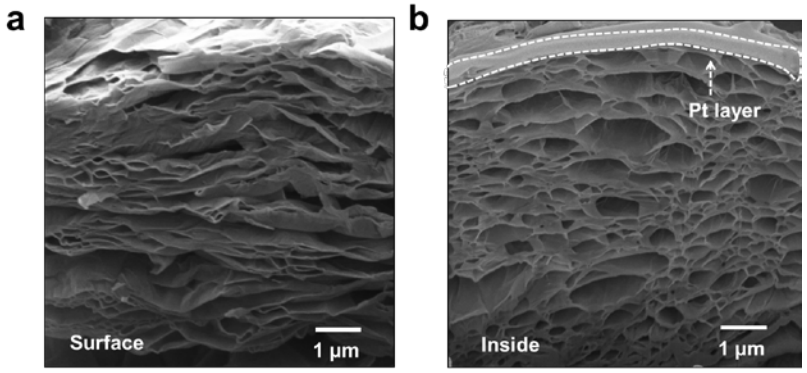

Figure 4-13. FE-SEM images of the functionalized graphene cathode a. at the surface (before FIB cutting) and **b.** inside (after FIB cutting). To prevent damage from FIB cutting, Pt was deposited on the surface of the sample.

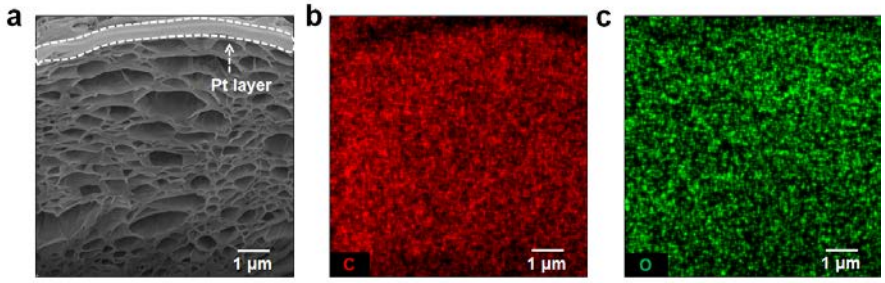

Figure 4-14. a. FE-SEM image of functionalized graphene after FIB cutting. **b.** EDS mapping of carbon. **c.** EDS mapping of oxygen.

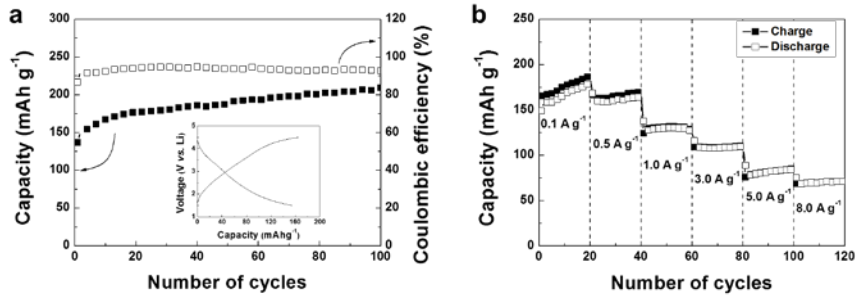

Figure 4-15. Electrochemical properties of functionalized graphene cathode. a. Cycle stability of the functionalized graphene cathode (inset: charge/discharge profile) in the voltage window between 1.5 and 4.5 V. **b.** Rate capability of the functionalized graphene cathode at different current rates from 0.1 to 8.0 A g^{-1}.

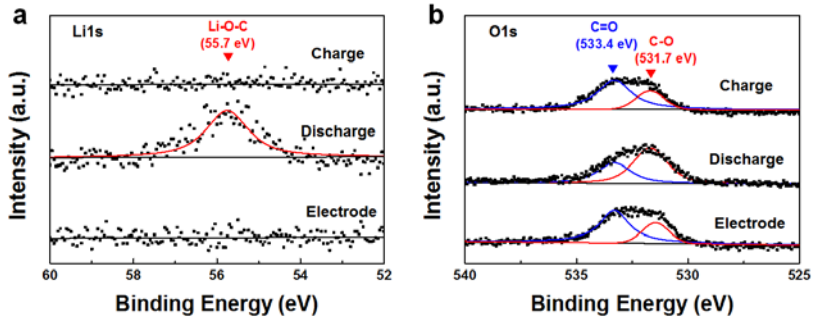

Figure 4-16. *Ex-situ* XPS analysis of functionalized graphene cathode at **a.** Li1s and **b.** O1s regions.

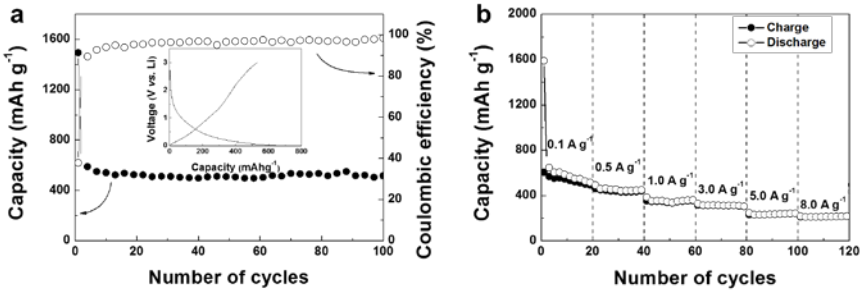

Figure 4-17. Electrochemical properties of reduced graphene oxide anode. a. Cycle stability of the reduced graphene oxide anode (inset: charge/discharge profile) in the voltage window between 0.01 and 3.0 V. **b.** Rate capability of the reduced graphene oxide anode at different current rates from 0.1 to 8.0 A g^{-1}.

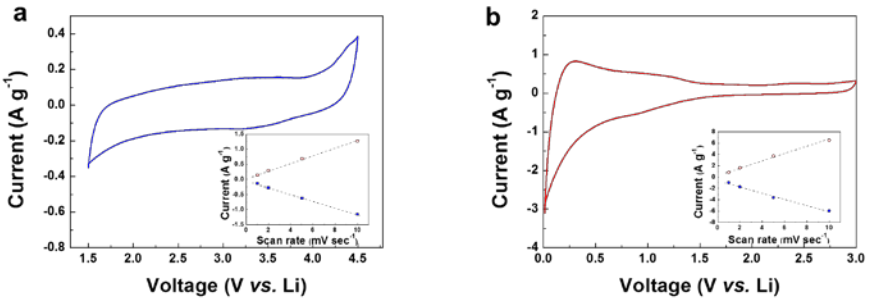

Figure 4-18. Cyclic voltammetry analysis for **a.** the functionalized graphene cathode and **b.** the reduced graphene oxide at a scan rate of 1.0 mV sec.$^{-1}$ (inset: linear relationship between redox peak current and scan rates).

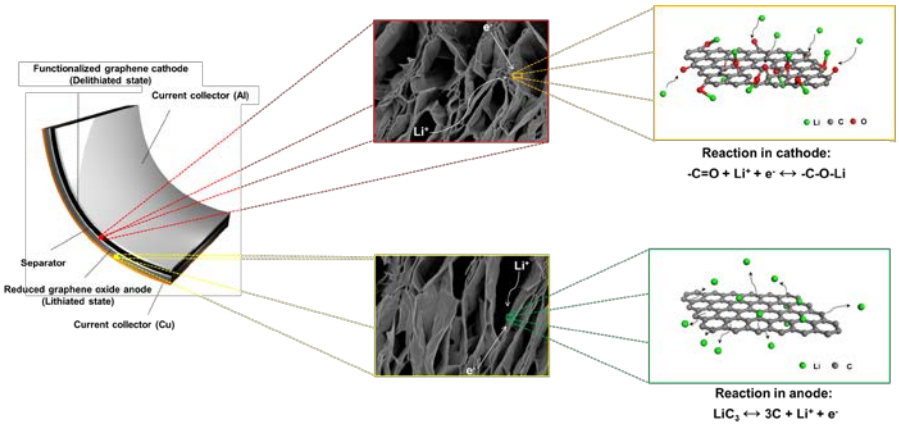

Figure 4-19. Schematic illustration of an advanced hybrid supercapacitor and its electrochemical reaction. In the functionalized graphene cathode, Li ions and electrons are stored in the functional groups on the graphene surface at a relatively high potential. On the other hand, Li ions and electrons are stored on the surface of graphene with low potential, in the reduced graphene oxide anode.

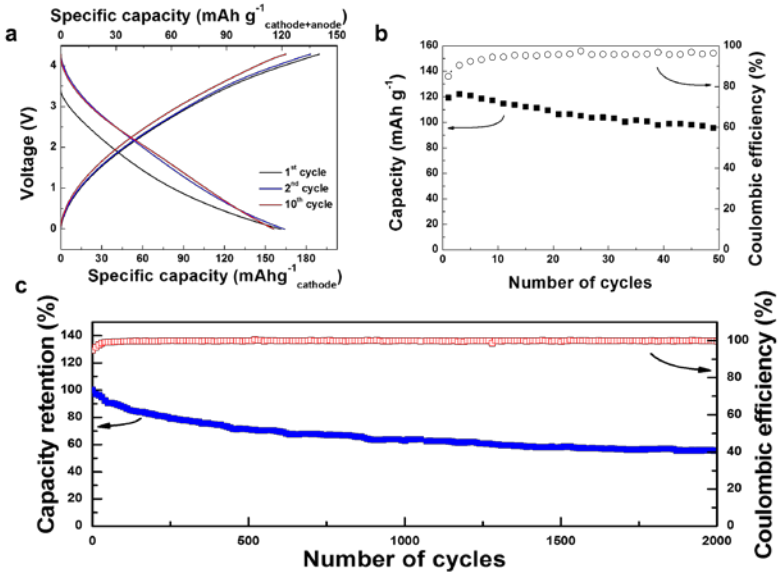

Figure 4-20. Electrochemical performance of an advanced hybrid supercapacitor composed of a functionalized graphene cathode and a reduced graphene oxide anode in a full cell system. a. Charge/discharge profiles at a current rate of 0.05 A $g^{-1}_{cathode+anode}$. Cycle stability of the advanced hybrid supercapacitor at a current rate of **b.** 50 mA g^{-1} and **c.** 500 mA g^{-1}.

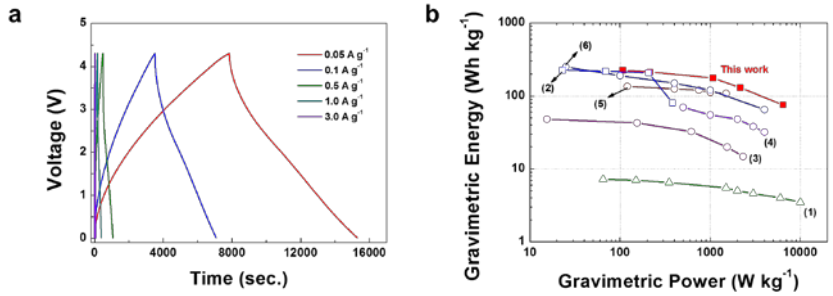

Figure 4-21. Rate capability of all-graphene energy storage devices. a. Charge/discharge profiles at various current rates from 50 mA g^{-1} to 3,000 mA g^{-1}. **b.** Ragone plot of the advanced hybrid supercapacitor that compares it to conventional Li batteries, supercapacitors, and other high performance hybrid supercapacitors based on the total weight of active materials (including both cathode and anode materials). (1) Symmetric supercapacitor (2) $LiMn_2O_4$/graphite (3) AC/G-$Li_4Ti_5O_{12}$ (4) ZHTP/$Li_4Ti_5O_{12}$ (5) URGO/MG (6) Fe_3O_4-G//3Dgraphene.

Table 4-1. BET surface area and pore volume of the functionalized graphene and the reduced graphene oxide.

	BET surface area	Pore volume
Functionalized graphene	278.3 m^2g^{-1}	0.921 cm^3g^{-1}
Reduced graphene	234.1 m^2g^{-1}	0.837 cm^3g^{-1}

3.3.5 References

1. McAllister, M. J.; Li, J.-L.; Adamson, D. H.; Schniepp, H. C.; Abdala, A. A.; Liu, J.; Herrera-Alonso, M.; Milius, D. L.; Car, R.; Prud'homme, R. K., et al. Single Sheet Functionalized Graphene by Oxidation and Thermal Expansion of Graphite. *Chem. Mater.* **2007,** *19*, 4396-4404.

2. Slater, M. D.; Kim, D.; Lee, E.; Johnson, C. S. Sodium-Ion Batteries. *Adv. Funct. Mater.* **2013,** *23*, 947-958.

3. Feng, H.; Cheng, R.; Zhao, X.; Duan, X.; Li, J. A low-temperature method to produce highly reduced graphene oxide. *Nat. Commun.* **2013,** *4*, 1539.

4. Chen, W.; Yan, L.; Bangal, P. R. Preparation of graphene by the rapid and mild thermal reduction of graphene oxide induced by microwaves. *Carbon* **2010,** *48*, 1146-1152.

5. Kudin, K. N.; Ozbas, B.; Schniepp, H. C.; Prud'homme, R. K.; Aksay, I. A.; Car, R. Raman Spectra of Graphite Oxide and Functionalized Graphene Sheets. *Nano Lett.* **2007,** *8*, 36-41.

6. Wang, H.; Robinson, J. T.; Li, X.; Dai, H. Solvothermal Reduction of Chemically Exfoliated Graphene Sheets. *J. Am. Chem. Soc.* **2009,** *131*, 9910-9911.

7. Park, Y.-U.; Seo, D.-H.; Kwon, H.-S.; Kim, B.; Kim, J.; Kim, H.; Kim, I.; Yoo, H.-I.; Kang, K. A New High-Energy Cathode for a Na-Ion Battery with Ultrahigh Stability. *J. Am. Chem. Soc.* **2013,** *135*, 13870-13878.

8. Yang, X.; Zhu, J.; Qiu, L.; Li, D. Bioinspired Effective Prevention

of Restacking in Multilayered Graphene Films: Towards the Next Generation of High-Performance Supercapacitors. *Adv. Mater.* **2011,** *23*, 2833-2838.

9. Simon, P.; Gogotsi, Y. Materials for electrochemical capacitors. *Nat. Mater.* **2008,** *7*, 845-854.

10. Wang, G.; Wang, B.; Wang, X.; Park, J.; Dou, S.; Ahn, H.; Kim, K. Sn/graphene nanocomposite with 3D architecture for enhanced reversible lithium storage in lithium ion batteries. *J. Mater. Chem.* **2009,** *19*, 8378-8384.

11. Lee, S. W.; Yabuuchi, N.; Gallant, B. M.; Chen, S.; Kim, B.-S.; Hammond, P. T.; Shao-Horn, Y. High-power lithium batteries from functionalized carbon-nanotube electrodes. *Nat. Nanotechnol.* **2010,** *5*, 531-537.

12. Kim, H.; Park, K.-Y.; Cho, M.-Y.; Kim, M.-H.; Hong, J.; Jung, S.-K.; Roh, K. C.; Kang, K. High-Performance Hybrid Supercapacitor Based on Graphene-Wrapped Li4Ti5O12 and Activated Carbon. *ChemElectroChem* **2014,** *1*, 125-130.

13. Appetecchi, G. B.; Prosini, P. P. 0.4 Ah class graphite/LiMn2O4 lithium-ion battery prototypes. *J. Power Sources* **2005,** *146*, 793-797.

14. Raymundo-Piñero, E.; Leroux, F.; Béguin, F. A High-Performance Carbon for Supercapacitors Obtained by Carbonization of a Seaweed Biopolymer. *Adv. Mater.* **2006,** *18*, 1877-1882.

15. Zhang, F.; Zhang, T.; Yang, X.; Zhang, L.; Leng, K.; Huang, Y.; Chen, Y. A high-performance supercapacitor-battery hybrid energy storage

device based on graphene-enhanced electrode materials with ultrahigh energy density. *Energy & Environ. Sci.* **2013,** *6*, 1623-1632.

16. Jain, A.; Aravindan, V.; Jayaraman, S.; Kumar, P. S.; Balasubramanian, R.; Ramakrishna, S.; Madhavi, S.; Srinivasan, M. P. Activated carbons derived from coconut shells as high energy density cathode material for Li-ion capacitors. *Sci. Rep.* **2013,** *3*, 3002.

17. Lee, J.; Shin, W.; Lim, S.; Kim, B.; Choi, J. Modified graphite and graphene electrodes for high-performance lithium ion hybrid capacitors. *Mater. Renew. Sustain. Energy* **2014,** *3*, 1-8.

Chapter 5. Summary

This thesis is composed of four parts: (i) natural graphite as an anode for Na rechargeable batteries, (ii) transition-metal-free cathode materials for Li and Na rechargeable batteries, (iii) all-graphene-battery, and (iv) advanced hybrid supercapacitors. In the first part, the thesis demonstrates that sodium intercalation into natural graphite is possible when ether-based electrolyte systems are used. Through sodium-solvent co-intercalation, natural graphite can deliver excellent cycle stability and rate performance. However, sodium storage mechanism is not yet clear and further study is needed. Also, it needs to discover why sodium-solvent co-intercalation is available only when specific electrolytes are used.

The second part demonstrates that the functionalized graphene nano-platelets with porous structures can be utilized as high performance cathode for Li and Na rechargeable battery. The functional groups can be redox centers storing Li and Na ions with acceptably high voltage for cathode applications. The functionalized graphene cathode uses surface Faradaic reactions differently from conventional inorganic electrode materials (*i.e.* $LiCoO_2$, $LiMn_2O_4$, and $LiFePO_4$) requiring solid-state diffusion. Therefore, the functionalized graphene nano-platelets cathode can provide much higher rate capability. Furthermore, the surface Faradaic reaction does not accompany large volume

change during battery operation. Thus, outstanding cycle performance could be achieved.

The third part demonstrates the all-graphene-battery which is composed of graphite derivative cathode and anode. In this device, the graphene with surface functional groups works as a cathode and that without functional groups functions as an anode. Because both electrodes use surface reactions, high power density can be obtained while maintaining high energy density.

The last part of this thesis introduces advanced hybrid supercapacitors. The hybrid supercapacitors typically use an intercalation based electrode and a capacitive electrode. The most important issue in the hybrid supercapacitors is the imbalance in kinetics between the two electrodes. The lithium de/intercalation reactions are kinetically slower than the surface reactions. So, it is vital to improve kinetics of intercalation based electrodes to deliver maximized performances in terms of energy and power. This thesis proposes novel approaches; (i) nanoparticles grown on graphene templates, (ii) bulk particles wrapped by graphene.

Chapter 6. Abstract in Korean

초 록

환경문제와 에너지 고갈의 문제로 인하여 고성능 에너지 저장 개발이 더욱 중요해지고 있다. 태양열, 풍력, 지열 등의 신재생 에너지를 적재적소에 사용하기 위해서는 에너지 저장장치의 개발이 필수 적이다. 또한, 현대사회의 에너지 사용량을 충족시키고 점점 대형화 되고 있는 전자 장치에 적용하기 위해서는 가격 경쟁력이 있는 소재를 사용해야 한다. 이러한 점에서 풍부한 매장량을 갖고 낮은 가격에 공정이 가능한 흑연계 소재는 차세대 전극소재로 여겨지고 있다. 하지만, 흑연계 전극소재는 주로 리튬 이차전지 음극으로의 활용으로만 제한되어 왔다. 본 논문은 흑연계 전극소재를 소듐 이차전지 음극으로 활용 할 수 있는 방법과 흑연계 전극소재를 리튬 및 소듐 이차전지 양극으로 활용할 수 있는 방법에 대해 논하였다.

제 2장은 지금까지 소듐이차전지 음극소재로 사용될 수 없다고 알려진 흑연을 소듐이차전지 음극으로 활용할 수 있는 방법을 소개한다. 에테르 계열 전해질을 사용할 경우 소듐과 전해액이 함께

그라파이트에 삽입/탈리 되면서 에너지를 저장할 수 있게 된다. 이 경우, 2000 싸이클 이상 매우 우수한 수명특성과 율특성을 발현하게 된다.

본 논문의 3장에서는 다공성 그래핀의 표면에 작용기를 달아 리튬 및 소듐 이차전지 양극으로 활용 가능성에 대해 다루고 있다. 그래핀 표면의 작용기는 리튬 및 소듐을 전기화학적으로 저장할 수 있다. 일반적으로 그래핀은 낮은 전압으로 인하여 이차전지 음극으로 사용되지만, 작용기를 달아 줄 경우 작동 전압이 크게 상승하여 양극으로 활용 할 수 있게 된다. 이 경우, 리튬 및 소듐이 그래핀 표면에서 반응을 하고 구조내부로 확산 할 필요가 없기 때문에 율특성이 매우 우수하게 나타난다. 또한, 충방전시 큰 부피 변화가 나타나지 않아 우수한 수명특성을 보인다.

제 4장에서는 양극과 음극이 모두 흑연계 전극소재로 구성되어 있는 리튬 이차전지에 대해 다루고 있다. 그래핀 표면의 작용기를 통하여 리튬을 저장하는 양극과 그래핀 표면에 리튬을 저장하는 음극을 조합하여 전이금속이 없는 리튬이차전지 풀셀을 구현하였다.

주요어: 탄소; 그래핀; 배터리; 에너지 저장; 에너지 변환
학 번: 2011-30186

Curriculum Vitae

Education

Seoul National University, Seoul, Republic of Korea

Ph.D., Department of Materials Science and Engineering, March. 2011 – February. 2015 (The Best Graduate Thesis Award)

Advisor : Prof. Kisuk Kang

KAIST, Daejeon, Republic of Korea

M.S., Graduate school of EEWS, September. 2009 – February. 2011

Advisor : Prof. Kisuk Kang

Hangyang University, Seoul, Republic of Korea

B.S., Department of Materials Science and Engineering, March. 2006 – August. 2009 (Summa Cum Laude)

Honors & Awards

- Energy Technology Division Graduate Student Award, The Electrochemical Society (2015)
- The Best Graduate Thesis Award (2014)
- Student Award of the Korea Section of the Electrochemical Society (2014)
- Best poster award, “Bio-inspired organic nanohybrids for sustainable high-power lithium ion batteries” Korea Battery Society (2014)
- 20^{th} Humantech Paper Award, Samsung Electronics (2014)

- Best poster award, grand prize “Biological redox cofactor nanohybrid for sustainable high-power lithium rechargeable batteries” Nano Korea (2014)
- Paper Presentation Award, “A high-energy cathode for a Na-ion battery with long cycle life” Korean Battery Society (2013)
- Paper Presentation Award, “Metal substitution effects on the crystal structures and Electrochemical properties of spinel-structured M_3O_4 anodes in lithium rechargeable batteries” The Korean Electrochemical Society (2012)
- Global Ph. D. Fellowship (2011) funded by Korean government (NRF-2011-0002392)
- Paper Presentation Award, “Neutron and X-ray diffraction analysis of pyrophosphate-based $Li_{2-x}MP_2O_7$ (M=Fe, Co) for lithium rechargeable battery cathode materials” Korean Battery Society (2011)

Publications (First author)

1. Sodium Storage Behavior in Natural Graphite using Ether-based Electrolyte Systems.

Haegyeom Kim, Jihyun Hong, Young-Uk Park, Jinsso Kim, Insang Hwang, Kisuk Kang*

Advanced Functional Materials DOI:10.1002/adfm.201402984.

2. Advanced Hybrid Supercapacitor based on a mesoporous niobium pentoxide/carbon as high-performance anode.

Eunho Lim†, Haegyeom Kim†, Changshin Jo†, Kyojin Ku, Seongseop Kim, Hyung Ik Lee, In-Sik Nam, Songhun Yoon*, Kisuk Kang*, and Jinwoo Lee*

ACS Nano, Vol. 8, 8968 (2014) †Equal contribution

3. Aqueous Rechargeable Li and Na Ion Batteries.

Haegyeom Kim†, Jihyun Hong†, Kyu-Young Park†, Hyungsub Kim†, Sung-Wook Kim, and Kisuk Kang*

Chemical Reviews, Vol. 114, 11788 (2014) †Equal contribution

4. The Reaction Mechanism and Capacity Degradation Model in Lithium Insertion Organic Cathodes, $Li_2C_6O_6$, Using Combined Experimental and First Principles Studies.

Haegyeom Kim, Dong-Hwa Seo, Gabin Yoon, William A. Goddard III, Yun-Sung Lee*, Won-Sub Yoon*, and Kisuk Kang*

The Journal of Physical Chemistry Letters, Vol. 5, 3086 (2014)

5. Novel Transition-metal-free- Cathode for High Energy and Power

Sodium Rechargeable Batteries.

Haegyeom Kim, Young-Uk Park, Kyu-Young Park, Hee-Dae Lim,

Jihyun Hong, and Kisuk Kang*

Nano Energy, Vol. 4, 97 (2014)

6. All-graphene-battery: bridging the gap between supercapacitors and lithium ion batteries.

Haegyeom Kim, Kyu-Young Park, Jihyun Hong, and Kisuk Kang*

Scientific Reports, Vol. 4, 5278 (2014)

7. High-performance hybrid supercapacitor based on graphene-wrapped $Li_4Ti_5O_{12}$ and activated carbon.

Haegyeom Kim, Kyu-Young Park, Min-Young Cho, Mok-Hwa Kim,

Jihyun Hong, Sung-Kyun Jung, Kwang Chul Roh, and Kisuk Kang*

ChemElectroChem, Vol. 1, 125 (2014)

8. Graphene for advanced Li/S and Li/air batteries.

Haegyeom Kim†, Hee-Dae Lim†, Jinsoo Kim, and Kisuk Kang*

Journal of Materials Chemistry A, Vol. 2, 33 (2014) †Equal contribution

9. Novel high-energy hybrid supercapacitor based on anatase TiO_2-reduced graphene oxide and activated carbon.

Haegyeom Kim, Min-Young Cho, Mok-Hwa Kim, Kyu-Young Park, Hyeokjo Gwon, Yunsung Lee, Kwang Chul Roh, and Kisuk Kang*

Advanced Energy Materials, Vol. 3, 1500 (2013)

10. Scalable Functionalized Graphene Nano-Platelets as Tunable Cathodes for High-performance Lithium Rechargeable Batteries.

Haegyeom Kim, Hee-Dae Lim, Sung-Wook Kim, Jihyun Hong, Dong-Hwa Seo, Dae-chul Kim, Seokwoo Jeon, Sungjin Park, and Kisuk Kang*

Scientific Reports, Vol. 3, 1506 (2013)

11. Multicomponent effects on the crystal structures and electrochemical properties of spinel-structured M_3O_4 (M=Fe, Mn, Co) anodes in lithium rechargeable batteries.

Haegyeom Kim, Dong-Hwa Seo, Hyungsub Kim, Inchul Park, Jihyun Hong, Kyu-Young Park, and Kisuk Kang*

Chemistry of Materials, Vol. 24, 720-725 (2012)

12. Nano-graphite platelet loaded with $LiFePO_4$ nanoparticles used as the cathode in a high Performance Li-ion battery.

Haegyeom Kim, Hyungsub Kim, Sung-Wook Kim, Kyu-Young Park, Jinsoo Kim, Seokwoo Jeon, and Kisuk Kang*

Carbon, Vol. 50, 1966-1971 (2012)

13. Electrochemical and ex-situ analysis on manganese oxide/graphene hybrid anode for lithium rechargeable batteries.

Haegyeom Kim, Sung-Wook Kim, Jihyun Hong, Young-Uk Park and Kisuk Kang*

Journal of Materials Research, Vol. 26, 2665-2671 (2011)

14. Graphene-Based Hybrid Electrode Material for High-Power Lithium-Ion Batteries

Haegyeom Kim, Sung-Wook Kim, Jihyun Hong, Hee-Dae Lim, Hyung Sub Kim, Jung-Keun Yoo and Kisuk Kang*

Journal of The Electrochemical Society, Vol. 158, A930-A935 (2011)

15. Highly Reversible Co_3O_4/Graphene Hybrid Anode for Lithium Rechargeable Batteries

Haegyeom Kim, Dong-Hwa Seo, Sung-Wook Kim, Jongsoon Kim, and Kisuk Kang*

Carbon, Vol. 49, 326-332 (2011)

16. SnO_2/graphene composite with high lithium storage capability for lithium rechargeable batteries.

Haegyeom Kim, Sung-Wook Kim, Young-Uk Park, Hyeokjo Gwon, Dong-Hwa Seo, Yuhee Kim and Kisuk Kang*

Nano research, Vol.3, 813-821 (2010)

17. 리튬 이차 전지용 그래핀 기반 전극물질 개발

김해겸, 권혁조, 홍지현, 강기석*

재료마당, Vol. 25, 27-33 (2012)

Publications (Contributing author)

1. Organic Nanohybrids for Fast and Sustainable Energy Storage.

Minha Lee, Jihyun Hong, Haegyeom Kim, Hee-Dae Lim, Sung Baek Cho, Kisuk Kang*, and Chan Beum Park*.

Advanced Materials, Vol. 16, 2558-2565 (2014)

2. Recent Progress on Flexible Lithium Rechargeable Batteries.

Hyeokjo Gwon, Jihyun Hong, Haegyeom Kim, Dong-Hwa Seo, Seokwoo Jeon and Kisuk Kang*

Energy and Environmental Science Vol 7, 538 (2014)

3. Size-selective synthesis of mesoporous LiFePO4/C microspheres based on nucleation and growth rate control of primary particles.

Min-Young Cho, Haegyeom Kim, Hyungsub Kim, Young Su Lim, Kwang-Bum Kim, Jae-Won Lee, Kisuk Kang,* and Kwang Chul Roh. *

Journal of Materials Chemistry A. Vol. 2, 5992-5927 (2014)

4. Effects of sulfur doping on graphene-based nanosheets for use as anode materials in lithium-ion batteries.

Young Soo Yun, Vet-Duc Le, Haegyeom Kim, Sung-Jun Chang, Seung Jae Baek, Jungjin Park, Byung Hoon Kim, Young-Hyun Kim, Kisuk Kang, and Hyoung-Joon Jin*

Journal of Power Sources, Vol. 262, 79-85 (2014)

5. Mechanism of Co_3O_4/graphene catalytic activity in Li-O_2 batteries using carbonate based electrolytes.

Hee-Dae Lim, Hyeokjo Gwon, Haegyeom Kim, Sung-Wook Kim, Taeho Yoon, Jang Wook Choi, Seung M. Oh, and Kisuk Kang*

Electrochimica Acta, Vol. 90, 63-70 (2013)

6. Factors that affect the phase behavior of multi-component olivine ($LiFe_xMn_yCo_{1-x-y}PO_4$; $0 < x, y < 1$) in lithium rechargeable batteries: One-phase reaction vs. two-phase reaction.

Kyu-Young Park, Jihyun Hong, Jongsoon Kim, Young-Uk Park, Haegyeom Kim, Dong-Hwa Seo, Sung-Wook Kim, Jang-Wook Choi and Kisuk Kang*

Journal of The Electrochemical Society, Vol. 160, A444-A448 (2013)

7. Defect-free solvothermally assisted synthesis of microspherical mesoporous $LiFePO_4$/C.

Min-Young Cho, Kwang-Bum Kim, Jae-Won Lee, Haegyeom Kim, Hyungsub Kim, Kisuk Kang* and Kwang Chul Roh*

RSC Advances, Vol. 3, 3421-3427 (2013)

8. Critical role of oxygen evolved from layered Li-excess metal oxides in lithium rechargeable batteries.

Jihyun Hong, Hee-Dae Lim, Minah Lee, Sung-Wook Kim, Haegyeom Kim, Song-Taek Oh, Geun-Chang Chung and Kisuk Kang*

Chemistry of Materials, Vol. 24, 2692-2697 (2012)

9. The predicted crystal structure of $Li_4C_6O_6$, an organic cathode material for Li-ion battery, from first-principles multi-level computational methods.

Dong-Hwa Seo, Hyungjun Kim, Haegyeom Kim, William A. Goddard III, and Kisuk Kang*

Energy and Environmental Science, Vol. 4, 4938 (2011)

10. Neutron and X-ray diffraction study of pyrophosphate-based $Li_{2-x}MP_2O_7$ (M = Fe, Co) for lithium rechargeable battery electrodes

Hyungsub Kim, Seongsu Lee, Young-Uk Park, Haegyeom Kim, Jongsoon Kim, Seokwoo Jeon and Kisuk Kang*

Chemistry of Materials, Vol. 23, 3930 (2011)

11. Superior rechargeability and efficiency of Li-O_2 batteries: Hierarchical air-electrode architecture combined with a soluble catalyst.

Hee-Dae Lim, Hyelynn Song, Jinsoo Kim, Hyeokjo Gwon, Youngjoon Bae, Kyu-Young Park, Jihyun Hong, Haegyeom Kim, Taewoo Kim, Yong Hyup Kim, Xavier Lepro, Raquel Ovalle-Robles, Ray H. Baughman, and Kisuk Kang*

Angewandte Chemie, Vol. 53, 3926-3931 (2014)

12. Understanding the degradation mechanisms of LiNi0.5Co0.2Mn0.3O2 cathode material in lithium ion battery.

Sung-Kyun Jung, Hyeokjo Gwon, Jihyun Hong, Kyu-Young Park, Dong-Hwa Seo, Haegyeom Kim, Jangsuk Hyun, and Kisuk Kang*

Advanced Energy Materials, Vol 4, 1300787(2014)

13. A new high-energy cathode for a Na-ion battery with ultrahigh stability.

Young-Uk Park, Dong-Hwa Seo, Hyung-Soon Kwon, Byoungkook Kim, Jongsoon Kim, Haegyeom Kim, Inkyung Kim, Han-Ill Yoo, and Kisuk Kang

Journal of the American Chemical Society, Vol 135,13870 (2013)

14. Understanding the electrochemical mechanism of the new iron-based mixed-phosphate $Na_4Fe_3(PO_4)_2(P_2O_7)$ in a Na rechargeable battery

Hyungsub Kim, Inchul Park, Seongsu Lee, Hyunchul Kim, Kyu-Young Park, Young-Uk Park, Haegyeom Kim, Jongsoon Kim, Hee-Dae Lim, Won-Sub Yoon, and Kisuk Kang

Chemistry of Materials, Vol 25, 3614 (2013)

15. The potential for long-term operation of a lithium-oxygen battery using a non-carbonate-based electrolyte.

Hee-Dae Lim, Kyu-Young Park, Hyeokjo Gwon, Jihyun Hong, Haegyeom Kim and Kisuk Kang*

Chemical Communications, Vol. 48, 8374-8376 (2012)

16. Invited paper: Preparation and Electrochemical Characterization of Doped Spinel $LiMn_{1.88}Ge_{0.1}Li_{0.02}O_4$ Cathode Material.

Sung-Wook Kim, Vadam Ganesh Kumar, Dong-Hwa Seo, Young-Uk Park, Jinsoo Kim, Haegyeom Kim, Jongsoon Kim, Jihyun Hong, and Kisuk Kang*

Electronic Materials Letters, Vol. 7, 105-108 (2011)

17. Highly Laminated Electrospun ZnO Nanofibrous Film in the Transparent Conducting Oxide for Photovoltaic Device.

Jinsoo Kim, Sanghoon Yoon, Jung-Keun Yoo, Jongsoon Kim, Haegyeom Kim, and Kisuk Kang*

Journal of Electrochemical Science and Technology, Vol. 3, 68-71 (2012)